Design and Fabrication of Suspended Si_3N_4 Photonic Crystal Devices For Use With Cold Atoms

PhD Thesis

Jonas Bundgaard Mathiassen

September 30., 2024

Supervised by

Professor Eugene S. Polzik, Assistant Professor Jean-Baptiste Béguin

University of Copenhagen

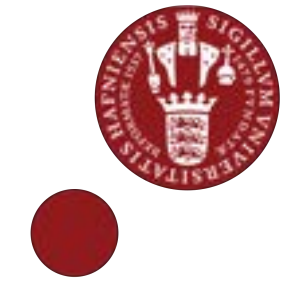

UNIVERSITY OF COPENHAGEN

Name of Institute:	Niels Bohr Institute
Name of Department:	Quantop
Author:	Jonas Bundgaard Mathiassen
Email:	jonas.mathiassen@nbi.ku.dk

Title	Design and Fabrication of Suspended Si_3N_4 Photonic Crystal Devices For Use With Cold Atoms
Supervisor:	Professor Eugene S. Polzik, Assistant Professor Jean-Baptiste Béguin
Handed in:	September 30.,2024
Date of defence:	November 25., 2024

Name _____

Signature _____

Date _____

Abstract

Photonic crystal devices are fabricated on a platform of suspended stochiometric silicon nitride (Si_3N_4) for integration with ultracold, optically trapped neutral atoms. Suspended, tethered waveguides and two-dimensional photonic crystals are designed, modeled, fabricated, and characterized. This work represents a step towards the realization of a hybrid quantum system that combines ultracold atoms with photonic crystal devices for quantum information processing and quantum simulation applications. This thesis describes the progress made in fabricating and characterizing these devices and discusses the challenges and opportunities for future research.

Sammenfatning

Fotoniske krystal-anordninger fremstilles på en platform af fritsvævende stochiometrisk siliciumnitrid (Si_3N_4) med henblik på integration med ultrakolde, optisk fangede elektrisk neutrale atomer. Fritsvævende, forankrede bølgeledere og todimensionale fotoniske krystaller designes, modelleres, fremstilles og karakteriseres. Dette arbejde udgør et skridt mod realiseringen af et hybridt kvantesystem, der kombinerer ultrakolde atomer med fotoniske krystal-anordninger til kvanteinformations- og kvantesimulationsapplikationer. Denne afhandling beskriver fremskridtene i fremstillingen og karakteriseringen af disse anordning, og diskuterer de udfordringer og muligheder, der ligger i fremtidig forskning.

Acknowledgements

So many people have been a positive influence on my life during my time in QUANTOP that I will inevitably forget to mention someone. First and foremost, I would like to thank my supervisor, Eugene Polzik, for offering me the opportunity to do a PhD in your group and for offering your support throughout the project. I also want to thank Jean-Baptiste Béguin for letting me join the light atom quantum simulator project. The width and depth of your knowledge never cease to amaze me, and as a fellow father of two, I have a tangible appreciation for your ability to balance your commitments. Jörg Müller got me interested in experimental laser physics in the first place, and our conversations about physics, music, and life, in general, are among the things I will miss the most now that I don't work in QUANTOP anymore.

In no particular order, I want to thank the following people: Anders Simonsen, who introduced me to the world of fabrication and had to put up with my smalltalk; Jacob Hansen, who helped create a friendly environment in the lab and kept me up to date on what was happening on the internet; Ivan Galinskiy, with whom I shared a very messy office and who was always willing to help me out with technical questions and memes; Christoffer Østfeldt, who was never afraid of having and sharing your opinion on things big and small; Chao Meng, who always manages to stay positive in the face of adversity; Ass. Prof. Emil Zeuthen, for your insights on music and life; Eric Langman, who helped me out in the cleanroom on multiple occasions; Rodrigo Thomas, who is the coolest dude in quantum optics; Georg Enzian, who was a kindred spirit in hard times; Andrea Grimaldi, who taught me about the shortcomings of Danish cuisine; Michał Parniak, who demonstrated how much you can achieve if you just work very hard, stay focused, and memorize all of The Silmarillion; Christian Bærentsen, who taught me that you don't have to agree on everything to be good colleagues; Sergey Fedorov, who was always very kind to me.

Finally, I want to thank my wife, Anine, for your support and patience throughout this project. The highlight of any day is coming home to you and the kids. I love you.

Scientific Output

Cold Atoms and Photonics for Quantum Simulation

Poster Presentation

Jonas Mathiassen, Anders Simonsen, Jacob Thornfeldt Hansen, Jörg Helge Müller, Eugene Simon Polzik and Jean-Baptiste Sylvain Béguin

Presented: International Conference for Integrated Quantum Photonics 2022.

Not related to the work presented in this thesis:

Phononically shielded photonic-crystal mirror membranes for cavity quantum optomechanics

Journal Article

Georg Enzian, Zihua Wang, Anders Simonsen, Jonas Mathiassen, Toke Vibel, Yeghishe Tsaturyan, Alexander Tagantsev, Albert Schliesser, Eugene S. Polzik

Published in: Optics Express Vol. 31, Issue 8, pp. 13040-13052 (2023)

Summary and contributions are described in Appendix C.

Contents

Chapter 1

Light Atom Quantum Simulator

The work presented in this thesis is a part of the Light-Atom Quantum Simulator (LAQS) experiment, which constitutes the experimental branch of the interdisciplinary Quantum for Life Centre[1], funded by the Novo Nordisk Foundation.

This chapter provides the background and motivation for the Light Atom Quantum Simulator (LAQS) project, followed by an introduction to the platform we are developing and key figures of merit (FOM). Finally, we outline the scope and structure of the thesis.

1.1 Motivation

Analog Quantum Simulators

Quantum simulation has experienced rapid growth in recent years, driven by the potential of controllable quantum systems to simulate complex phenomena where existing methods on classical computers are inefficient. Quantum simulators are designed to mimic the behavior of quantum systems that are difficult to study directly and could enable the design of high-temperature superconductors[2] and other quantum materials [3]. There are two approaches for building such a quantum simulator: a digital and an analog. In a digital quantum simulator, the problem is discretized and solved on a set of programmable quantum gates. In contrast, in an analog quantum simulator, the problem is mapped onto a physical system that can be controlled and manipulated in the lab[4]. A universal quantum computer can be a digital quantum simulator for arbitrary systems[5]. Still, the requirement for many qubits and low error rates makes this challenging.

Analog computation offers an alternative approach to quantum simulation, where the quantum system itself is used to simulate another quantum system. This approach can simulate the dynamics of a quantum system without the need for error correction,

as many physically relevant many-body models are stable to errors in analog quantum simulators[6]. Various platforms are currently being explored as quantum simulators, including trapped ions, superconducting qubits, ultracold atoms, and photonic systems, which are often disparate in their quantum degrees of freedom and range of operation frequency.

This thesis focuses on a hybrid system combining the two latter platforms, ultracold atoms, and photonic systems, to create a light-atom quantum simulator. We will briefly introduce the two platforms and then discuss how a hybrid system could leverage the strengths of both platforms to create a powerful quantum simulator.

Strong Light-Matter Interaction, cavity QED

A key objective in quantum electrodynamics (QED) is facilitating efficient light-matter interactions, described by the interaction Hamiltonian

$$H_{\text{int}} = -\boldsymbol{\mu} \cdot \mathbf{E}, \tag{1.1.1}$$

where $\boldsymbol{\mu}$ is the dipole moment of the emitter and $\mathbf{E}$ is the electric field of the light. The interaction strength is determined by the emitter's dipole moment and the electric field's strength at the dipole.

Although increasing the electric field strength enhances the interaction, in QED experiments, the efficiency of this interaction is often of greater interest. A useful measure is the probability P that a two-level atom will absorb a photon from a weak resonant laser beam, $P = \sigma_{\text{sc}}/A_{\text{eff}}$, where σ_{sc} is the scattering cross-section of the atom and A_{eff} is the effective mode area of the light.[1] It can be shown that for an ideal two-level system, the scattering cross section is bounded in the unitary limit by $\sigma_{\text{sc}} \leq 3\lambda^2/2\pi$ [7] where λ is the wavelength of the transition. In free space, the mode area can be decreased by tightly focusing the light, but this is limited by diffraction, and as a consequence, so is P[8].

One of the most successful ways of increasing the interaction is cavity QED, where the interaction strength is increased by placing the atom between two mirrors to recirculate the light, thereby increasing the interaction by the number of roundtrips. The interaction efficacy is quantified by the cooperativity parameter $C = \sigma_{\text{sc}} N/A_{\text{eff}}$, where N is the number of round trips the light makes in the cavity. The cooperativity can no longer be interpreted as a probability as C can be greater than one. The more typical expression for the cooperativity is

$$C = \frac{g^2}{\kappa\Gamma}, \tag{1.1.2}$$

where g is the rate at which a photon interacts with a two-level system inside the cavity, κ is the decay rate of the resonator, and Γ is the decay rate of the emitter. The

[1] This is the first-order expansion of the scattering probability $P = 1 - e^{-\sigma_{\text{sc}}/A_{\text{eff}}}$

cooperativity emerges as the relevant FOM when optimizing a desired process in the presence of losses, for example, when trying to achieve maximum fidelity in photon-mediated spin interactions in a system with finite interaction strength and losses. In a cavity of quality factor $Q = \omega/\kappa$ where ω is the resonance frequency, the cooperativity can be shown to be $C \propto Q\lambda^3/V_{\text{eff}}$, where V_{eff} is the effective mode volume of the cavity. In a short, high Q optical resonator, cooporativities of $C \approx 10 - 100$ have been demonstrated [9][10].

Interestingly, even when there is no strong coupling, the cavity affects the spontaneous decay of an excited atom. In 1946, Purcell[11] showed that when coupled to a resonator of volume V and quality factor Q, the spontaneous emission rate of an emitter is modified by a factor

$$F_p = \frac{\Gamma}{\Gamma_0} = \frac{3Q\lambda^3}{4\pi^2 V}, \tag{1.1.3}$$

known as the Purcell enhancement. This enhancement of spontaneous decay rate is caused by an increase in the local density of states (LDOS), leading us to engineer the LDOS beyond free-space cavities.

Waveguide QED

With advancements in microfabrication techniques over the past decades, nanophotonics has emerged as a powerful tool for manipulating light at the nanoscale. By confining light within dielectric materials, mode volumes can be reduced to $V_{\text{eff}}(\lambda/n)^3$, with recent experiments demonstrating $V_{\text{eff}} \sim 3\times10^{-4}\lambda^3$ [12]. Beyond the confinement of light, the dispersion can be engineered by periodically modifying dielectric structures at length scales comparable to optical wavelengths to form photonic crystals[13]. In these crystals, it is possible to open frequency bands, called bandgaps, where only evanescent waves can propagate. At the edges of such a bandgap, the dispersion creates slow-light regions where the group index $n_g = c(\frac{\partial\omega}{\partial k})^{-1}$ diverges, and the LDOS is significantly modified [14]. This modification of the LDOS, together with the small mode volumes, makes this a potent platform for creating strong interaction between emitters and light, and indeed systems using solid-state emitters such as quantum dots [15] and color centers [16] are already well-established platforms. Using atoms as the emitters in such a system presents several exciting possibilities, which we shall discuss in the following section.

The presence of a Photonic Crystal (PhC) modifies the rate of spontaneous emission by the F_p, but only a part of the emission is coupled into the guided modes of the waveguide, so in the context of emitters coupled to waveguide modes, the relevant figure of merit is the β-factor

$$\beta = \frac{\Gamma_{\text{wg}}}{\Gamma} \tag{1.1.4}$$

which is related to the cooperativity

$$C = \frac{\beta}{1-\beta} = \frac{\Gamma_{\mathrm{wg}}}{\Gamma'}, \tag{1.1.5}$$

where Γ' is decay into radiative modes. For quantum dots coupled to PhCs, β-factors close to unity have been demonstrated [17][18]. It can also be shown that in a waveguide coupled to N atoms, the transmission coefficient for resonant light is β^N[19].

Integration of Atoms and Photonic Waveguides

A hybrid system with ultracold atoms coupled to PhC waveguides arises as a promising platform for many-body quantum QED: Cold atoms are naturally identical emitters, and when coupled to the evanescent fields of modes in PhC waveguides, their interaction can be mediated through the guided modes of the structures. Moreover, with atoms trapped in dipole traps either formed by guided modes in the structure or arrays of optical tweezers, scaling to a large number of atoms is, in principle, possible.

When describing the dynamics of atoms coupled to PhC waveguides, it is convenient to do so in terms of the dyadic Green's function $\mathbf{G}$[20][21]. This is a tensor quantity describing the electromagnetic field along the axis α at a point $\vec{r}$ due to a source at $\vec{r}'$ polarized along the β-direction, oscillating at angular frequency ω for $\alpha, \beta \in \{x, y, z\}$. The Green's function is the solution to the inhomogeneous wave equation [14]

$$\left[(\nabla \times \nabla \times) - \epsilon(\mathbf{r}, \omega)\frac{\omega^2}{c^2}\right] \mathbf{G}_{\alpha\beta}(\mathbf{r}, \mathbf{r}', \omega) = \delta(\mathbf{r} - \mathbf{r}') \otimes \mathbf{I}, \tag{1.1.6}$$

where $\epsilon(\mathbf{r}, \omega)$ is the unitless dielectric function encoding information about the PhC, and $\mathbf{I}$ is the unit dyad.

The deterministic dynamics of N two-level atoms with density matrix ρ

$$\dot{\rho} = -i(H_{\mathrm{dd}}\rho - \rho H_{\mathrm{dd}}^{\dagger}), \tag{1.1.7}$$

can be described in terms of the Hamiltonian [22]

$$H_{\mathrm{dd}} = -\mu_0 \omega_{eg}^2 \sum_{i,j} \boldsymbol{\mu}^* \cdot \mathbf{G}(\mathbf{r}_i, \mathbf{r}_j, \omega_{eg}) \cdot \boldsymbol{\mu} \sigma_{eg}^i \sigma_{ge}^j, \tag{1.1.8}$$

with $\boldsymbol{\mu} = \langle e|\boldsymbol{\mu}|g\rangle$ being the dipole matrix element of the atom , σ_{eg}^i is the atomic raising operator at site i, and ω_{eg} is the transition frequency. The Green's function is evaluated at the transition frequency, and the sum is over all pairs of atoms in the system. The full dynamics also include a Lindbladian term describing decay away from the PhC, which is omitted in this description for simplicity [22].

This Hamiltonian incorporates both the spin-exchange rate J_{ij} and the decay rate Γ_{ij}[19],

$$J^{ij} = \left(\frac{\mu_0 \omega_{\text{eg}}^2}{\hbar}\right) \boldsymbol{\mu}^* \cdot \text{Re}\, \mathbf{G}(\mathbf{r}_i, \mathbf{r}_j, \omega_{\text{eg}}) \cdot \boldsymbol{\mu}, \tag{1.1.9}$$

$$\Gamma^{ij} = \left(2\frac{\mu_0 \omega_{\text{eg}}^2}{\hbar}\right) \boldsymbol{\mu}^* \cdot \text{Im}\, \mathbf{G}(\mathbf{r}_i, \mathbf{r}_j, \omega_{\text{eg}}) \cdot \boldsymbol{\mu}. \tag{1.1.10}$$

The appeal of phrasing the problem in terms of the Green's function is that it allows for a direct connection between the properties of the PhC and the dynamics of the atoms, as the Green's function can be calculated numerically from the PhC geometry. Two regimes emerge when considering the interaction between atoms and PhC waveguides: the dispersive and the dissipative regime fig. 1.1.

In the dispersive regime, the atomic transition is inside the bandgap, and the atoms interact dispersively via the evanescent field inside the bandgap, and the dissipative interaction is suppressed, leading to an effective spin Hamiltonian

$$H_{\text{spin}} = \sum_{\beta=x,y,z} \sum_{i,j} J_{ij}^{\beta} \sigma_i^{\beta} \sigma_j^{\beta}, \tag{1.1.11}$$

where the J_{ij}^{β} are the spin-spin couplings between the atoms at site i and j. The spatial dependence on this coupling depends on the specific PhC geometry and the specific atomic transition, but in a 1D PhC waveguide, the coupling $J_{ij}(x) \propto e^{|x_i - x_j|/L}$[23], where L is the decay length of the evanescent field, which can be tuned by the curvature of the band at the band edge α, and the detuning of the atomic transition with respect to the band edge frequency $\Delta = \omega_{\text{be}} - \omega_{eg}$.

In the dissipative regime, there is still a dispersive interaction, but the atoms also interact dissipatively via the guided modes of the photonic crystal, and the excitations eventually decay away. In this case, the dynamics can be described by a master equation similar to the abovementioned. In this case, the photonic waveguide mediates long-range interaction, which can result in collective effects such as superradiance [24].

Significant advances have been made in this field within the last two decades. In 2013, a single atom in a dipole trap was coupled to a nanoscale cavity [25]. A corrugated 1D alligator waveguide (AWG) coupled to optically cooled Cs atoms has been used to demonstrate atom-light interaction [26] and band edge physics [27].

Many experimental challenges still need to be addressed, including the delivery of atoms to the surface. A promising approach is using counter-propagating side-illumination beams to form a standing wave. The atoms can be delivered via a conveyor belt by scanning the phase between the two to move the standing wave [28][29].

To summarize, hybrid systems with ultra-cold atoms coupled to photonic crystal waveguides are a promising platform for simulating a broad class of Hamiltonians. The parameters are tunable by the choice of PhC and the in-situ positioning of the atoms on the crystal.

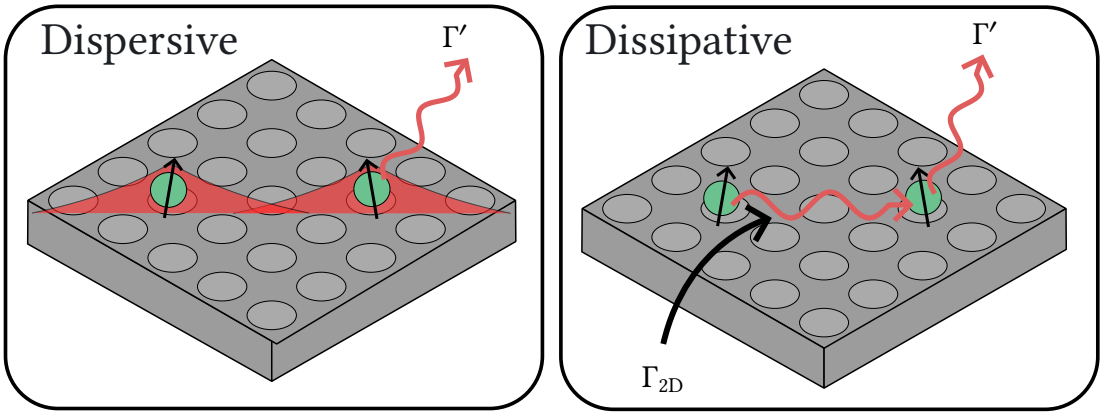

Figure 1.1: The dispersive and the dissipative regimes of the atom-photonic platform. On the left, the atomic transition is inside the bandgap, and the atoms interact dispersively via the evanescent field. On the right, the atomic transition is outside the bandgap, and the atoms interact dissipatively via the guided modes of the photonic crystal. In both cases, the atoms can decay into the radiating modes, which can be either suppressed or enhanced by the presence of the photonic crystal.

1.2 The Light Atom Quantum Simulator

In the LAQS project, we are working towards realizing a platform where the interaction between ultracold Cs atoms trapped in an array of dipole traps can be engineered using 2D photonic crystals. The prospect of moving to a 2D PhC is promising as it opens up new possibilities for engineering the interaction between the atoms. In a 2D PhC, the emission into unwanted modes can be suppressed beyond what is possible in a 1D system, as the crystal subtends a larger solid angle. In [28] they suggest a scheme where the strength and sign of the coupling can be controlled by the relative positions of the atoms, which combined with the ability to move the atoms using optical tweezers enables a powerful platform for analog quantum simulation.

We leverage extensive knowledge of trapping Cs atoms near dielectric structures from the QUANTOP research group[30]. This knowledge is complemented by assistant professor Jean-Baptiste Béguin's expertise, which he developed during his time in the pioneering research group of the late H.J. Kimble. The apparatus is shown in fig. 1.2, where atoms are cooled in a dual-chamber configuration before being captured in an array of optical tweezers.

To run a quantum simulation on this system, the atoms would be cooled and loaded into an array of optical traps. They would be prepared in an initial state using either global or site-wise addressing. The atoms are transported to the surface of the PhC, where they are held in dipole traps formed by a combination of guided modes in the structure, while interactions between atoms are mediated by their coupling to the evanescent field to the guided modes of the structure. The states of the atoms evolve

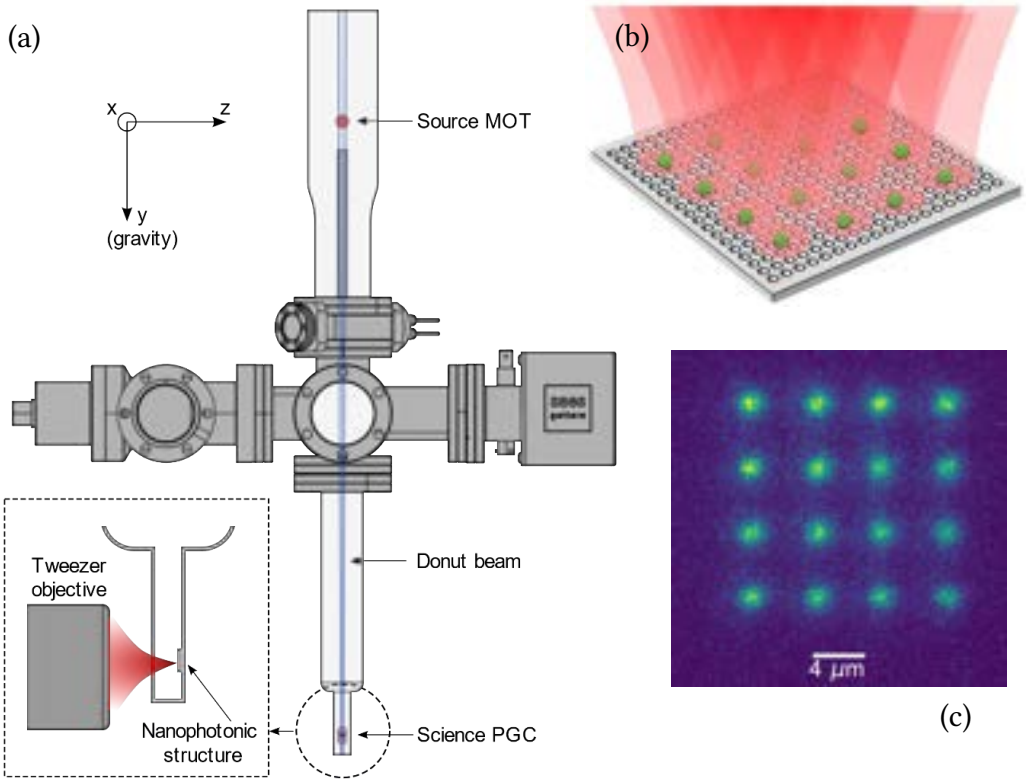

Figure 1.2: (a) The LAQS apparatus. Atoms are cooled in a source magneto-optical trap (MOT) before being funneled to a second chamber, where they are further cooled using polarization gradient cooling (PGC) and captured in a tweezer array. The atoms are transported to the structure's surface by moving the tweezer objective. (b) Illustration of atoms held in a tweezer array at the surface of a photonic crystal. (c) Average of 400 experimental runs of atoms trapped in 16 individual optical tweezer traps. Figures courtesy of Jacob T. Hansen.

according to the Hamiltonian in eq. (1.1.8), and the final states of the atoms are read out using fluorescence imaging.

Many challenges lie ahead in realizing this platform, including the design and fabrication of the PhC, the integration of the PhC with the atomic experiment, and the optimization of the interaction between the atoms.

The work presented here aims to establish a toolbox for designing, fabricating, and testing nanophotonic devices for use in this experiment.

1.3 Thesis Outline

Like most branches of science, the design and fabrication of nanophotonics presents unique challenges and pitfalls. As the first student in our research group to explore the world of photonics, electron beam lithography, and high aspect ratio dry etching, I have experienced many interesting and insightful moments along the way. The device that meets all requirements for full integration with the LAQS experiment is still to be fabricated, but significant progress has been made, and this thesis documents the work done so far in this direction.

In chapter 2, the nominal device is presented, followed by theoretical and numerical modeling of various aspects of the device, including the modeling of the dispersive characteristics of a photonic crystal, stress relaxation, and incoupling optimization.

In chapter 3, the details of the fabrication procedure are outlined. The fabrication flow is explained, with parameters for the various process steps, descriptions of the challenges encountered, and strategies to circumvent them.

The characterization of the devices is presented in chapter 4. Here, the focus is split between the characterization of the fabricated devices and discussing the merits and limitations of various characterization tools.

Finally, in chapter 5, the results are summarized, and the outlook for the project is discussed.

Chapter 2

Device Design and Modeling

This chapter presents the project's modeling and simulation efforts. We start with an overview of what a device compatible with atoms trapped in a tweezer array. The following section presents the plain waveguide with support structure and the idea of using a cavity formed by two 1D mirrors on the waveguide to determine waveguide propagation loss. Finally, a discussion of the design of the photonic crystal slabs is given, with a focus on the tolerances of the design parameters.

2.1 Device Overview

An overview of the desired device is shown in fig. 2.1. The central part of the device consists of a PhC designed to modify the interaction of the atoms by aligning an atomic transition frequency relative to the band edge frequency. Since the interaction is mediated by coupling to the evanescent field of the device, only air-clad devices are considered. Moreover, since the interaction window should also accommodate the presence of highly focused optical tweezer beams, the interaction section should be suspended over a transparent window. The requirement for the device to be suspended is part of the reason that stochiometric Si_3N_4 is the material of choice, as the intrinsic high tensile stress of the material keeps the device flat after release. Work has been done on a platform where the Si_3N_4 devices are sitting on a platform of SiO_2 and Si_3N_4 [29][31], which forms a transparent window, but this makes the formation of a 2D bandgap challenging as we shall discuss shortly. We opt instead for a fully suspended design similar to the one used in the group of the late H.J. Kimble [26][24][32].

The section indicated by a **B** in fig. 2.1 is the mode-matching section, where the spatial mode is transformed from the 1D waveguide to the 2D PhC mode. This section is necessary to ensure that the light is efficiently coupled to the PhC and that the light is efficiently coupled back to the waveguide. The approach used in [33] is to adiabatically widen the waveguide at the interface with the 2D crystal. At the boundary layer to the

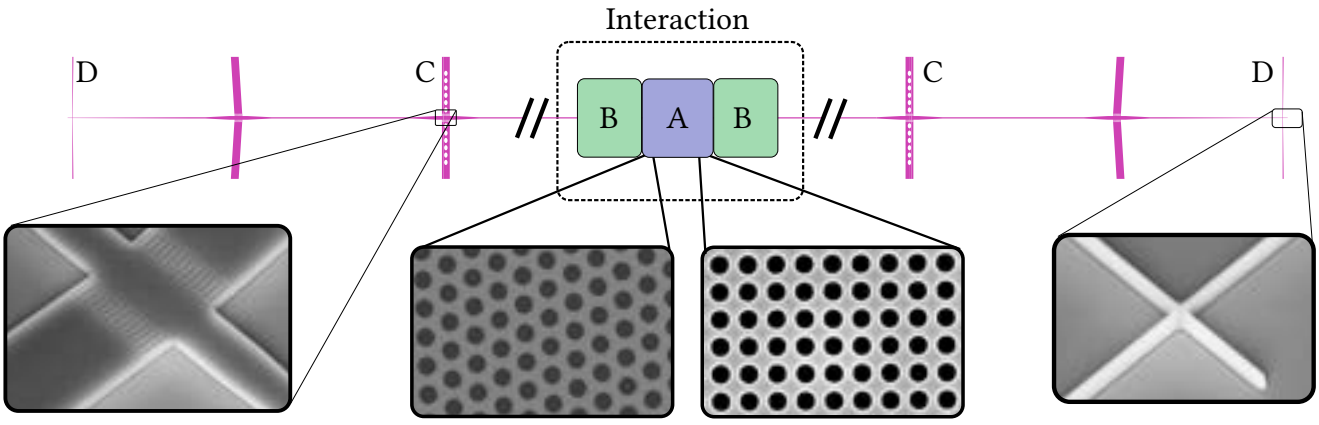

Figure 2.1: Overview of the desired waveguide design with inset SEM micrographs. The device is suspended over a V-groove in the Si substrate, with the interaction section being suspended over a fully etched window through the substrate. The aspect ratio of an actual device does not match what is shown here, as indicated by the slashes. **A** is the PhC, which can have either a hexagonal or square symmetry depending on the application. **B** is a mode-matching section where the 1D mode of the waveguide is transferred to a 2D-like mode in the PhC. **C** are tethers that keep the waveguide suspended and act as a channel for thermal dissipation while minimizing scattering loss. **D** is the inversely tapered waveguide coupler that allows efficient coupling between the waveguide and an optical fiber.

PhC, a layer of anti-reflection holes is added, followed by a section of self-collimating crystal structure[34] to prevent the light from diverging. For a detailed description of this approach, we refer to reference [35], as the optimization and implementation of this structure are not treated in this thesis. In the mode-matching section, the PhC could also be coupled to multiple 1D waveguides at different boundaries of the PhC to access different symmetry directions to either inject trapping light or to resolve the potential directional transmission of the atoms that we will discuss in section 2.4.2.

The light from the mode-matching section is coupled to a photonic waveguide connected to the outside world through a coupler marked by **D** in fig. 2.1. The nominal waveguide and the coupler should be designed and fabricated to minimize losses from scattering and unwanted reflections.

Additionally, atomic experiments require ultra-high vacuums, which places several constraints on the device's design, which we will discuss in more detail in the following section.

2.2 Suspended Waveguides

These waveguides have several requirements we must address in the design and fabrication process:

Single mode The waveguide must be single-mode to ensure the light is guided to the 2D structure with minimal losses.

Waveguide Suspension The waveguides are suspended in air, allowing the atoms to interact with the guided modes via the evanescent field. The PhC membrane must be suspended over a window in the substrate to accommodate the optical tweezer array.

Thermal Dissipation The waveguide must be able to dissipate the heat generated by light absorbed in the structure.

Mechanical Stability The high tensile stress of Si_3N_4 requires careful consideration of stress concentration, static deformations, and thermally driven mechanical modes.

Coupling The waveguide must efficiently couple light from either a free-space mode or an optical fiber into the waveguide.

In the following sections, we will address these criteria.

2.2.1 Single mode: Dispersion and Symmetry of the 1D Waveguide

The dispersion of the waveguide is shown in fig. 2.2b, where each vertical line corresponds to a solution to the partial differential equation [13]

$$\nabla \times \left(\frac{1}{\varepsilon(\mathbf{r})} \nabla \times \mathbf{H}(\mathbf{r}) \right) = \left(\frac{\omega}{c} \right)^2 \mathbf{H}(\mathbf{r}), \tag{2.2.1}$$

where $\varepsilon(\mathbf{r})$ is the dielectric function, $\mathbf{H}(\mathbf{r})$ is the magnetic field, ω is the angular frequency of the light, and c is the speed of light. The differential equation is most elegantly phrased in terms of the magnetic field, and the electric field can be obtained from the magnetic field as

$$\mathbf{E}(\mathbf{r}) = \frac{i}{\omega \varepsilon_0 \varepsilon(\mathbf{r})} \nabla \times \mathbf{H}(\mathbf{r}). \tag{2.2.2}$$

For the plain waveguide, the permittivity has continuous translational symmetry along the x axis, $\varepsilon(x + \delta x) = \varepsilon(x)$, for any x. The solution will be of the form $\mathbf{E}(\mathbf{r}) = E_{n,k_x}(y, z)e^{-ik_x x}$. The dispersion links the angular frequency of the solutions to their propagation constants

$$\omega = \omega_n(k_x), \tag{2.2.3}$$

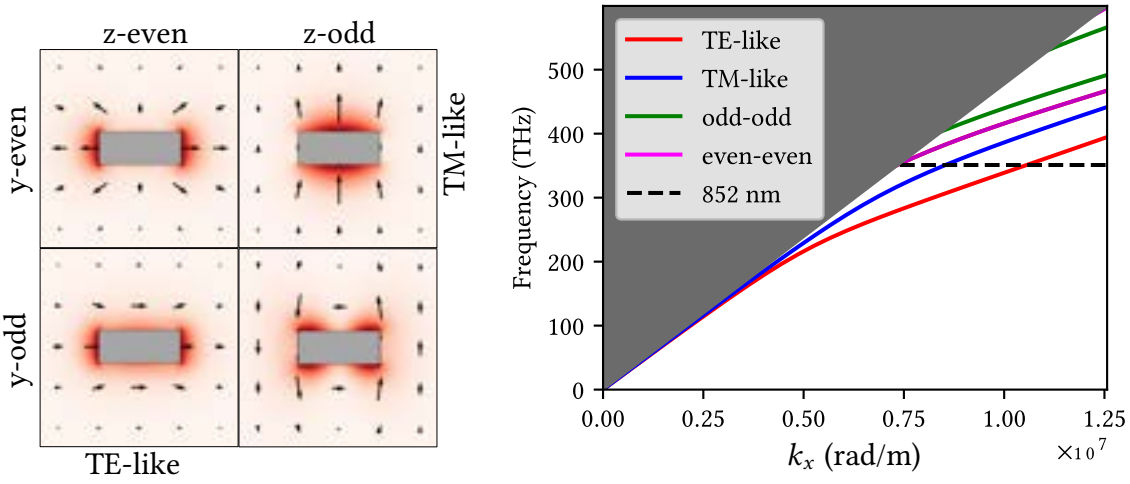

Figure 2.2: Symmetries and dispersion of a 1D photonic waveguide with a width of 500 nm and height of 200 nm and $n = 1.99$. On the left, the four types of modes are shown. The arrows indicate field direction, and the colors indicate the intensity $\propto |\mathbf{E}(\mathbf{r})|^2$. It supports a single TE-like and TM-like mode at 852 nm. (b) The dispersion of the four modes is shown in (a). The second TE-like mode is degenerate with the y-even z-even mode, and we see that for frequencies below 351 THz (or wavelengths above 852 nm), only two modes are guided, the TE- and the TM-like.

where n is the mode index for the bands. The grey area corresponds to the light line where $k_x > \omega/c$, implying that k_y or k_z has a non-zero, real component, making the mode radiative and not guided.

From this dispersion relation, we can calculate the group velocity of the mode as

$$v_g = \frac{d\omega}{dk_x}, \tag{2.2.4}$$

and the corresponding group index

$$n_g = \frac{c}{v_g}. \tag{2.2.5}$$

The waveguide's dispersion and modes are calculated using MPB[36], a free, open-source package that solves Maxwell's equations in the frequency domain for periodic structures.

The waveguide is a rectangular slab of stoichiometric Si_3N_4 with a width of 500 nm and a thickness of 200 nm surrounded by air. At these sizes, the waveguide supports a TE-like and a TM-like mode at 852 nm, as shown in fig. 2.2, which are of interest as they can be excited efficiently by available free-space laser beams or linearly polarized modes of optical fibers.

It is desirable to have the waveguide as broad as possible to minimize scattering from the sidewalls, but having the waveguide be single mode prevents scattering into higher order modes. These dimensions are chosen such that the second-order TE-like mode, degenerate with the fundamental z-even y-even mode, is just above the light line.

2.2.2 Tether Design

Optical Losses

Tethering is necessary to suspend the waveguide, but at each tethering point, the continuous x symmetry is broken, which causes scattering and reflection. This loss will be mode-dependent, and generally, changes to the geometry in the plane of the structure have a more substantial effect on the TE than the TM mode. Intuitively, we can understand this from looking at fig. 2.2 where we see that for the TE (TM) mode, most of the light is propagating on the sides (top/bottom) of the waveguide and thus sees the perturbation more or less.

The scattering from the tethers can be reduced by adiabatically widening the waveguide at the tethering section, which confines more of the light in the core and away from the tethers. In this platform, the waveguide is released from the substrate using KOH etching, which will be described in further detail in section 3.6. In a KOH etch, areas that are too large and unperforated will not be released from the substrate, which limits how wide we can make the tethering section and the tether. We adopt the same approach as used in [37][33][38], which uses an array of tethers to form an effective lower-refractive index material at the boundary of the tethering section, which helps to minimize scattering loss. An SEM micrograph of the tethering section is shown fig. 2.1C.

We find that we can reliably underetch a tethering section of width 1.5 µm, and with this width, we simulate the scattering for combinations of the pitch and width of the thethers. This simulation is done with finite difference time domain (FDTD) simulation, where the transmission through a section of width 1.5 µm is simulated for 15 tethers of varying pitch and width. The results of these simulations are shown in fig. 2.3. Smaller tethers generally produce lower losses, but fabricating tethers thinner than 100 nm is problematic. Choosing a tether pitch of a_{tether} =238 nm and a tether width of w_{tether} = 110 nm, the scattering from the tethers should be less than 1 % per tether array for the TE polarization, and even less for the TM polarization.

Waveguide Suspension

In the section of the chip with the PhC, the waveguide is suspended over a window in the substrate. The window is necessary to provide optical access to the waveguide

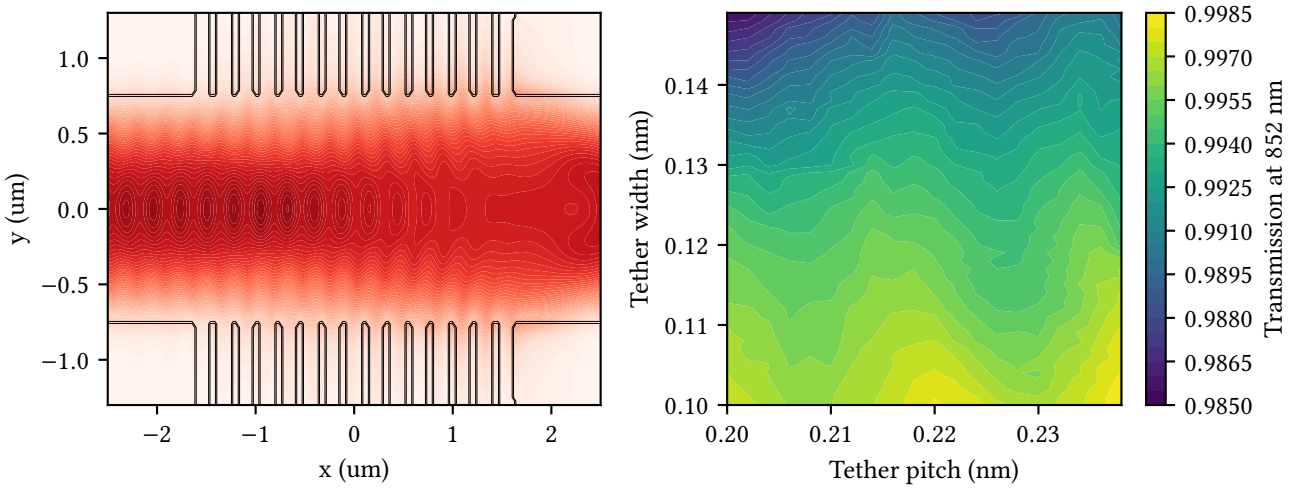

Figure 2.3: Transmission through a section with 15 tethers. On the left is the simulated transmission of a TE-like injection from the left at 852 nm. The tether pitch is a_{tether} = 238 nm and tether width w_{tether} = 110 nm. On the right are the transmission values for a scan of the width and pitch of the tethers.

from both the top and the bottom, which is required to trap the atoms at the structure's surface, as we shall discuss briefly in section 2.4.3. Another consideration is that the Si substrate will reflect and absorb the light from the tweezer array. Spurious reflections can perturb the trapped atoms and the absorption, which will heat the substrate, leading to thermal expansion. As the tweezer array is highly focused, these thermal effects could even change with the position of the tweezer, which could lead to unpredictable dynamics as the thermal expansion may affect optical parameters via various mechanisms such as stress-induced birefringence or changes to the waveguide geometry caused by the changed boundary conditions of the thermally expanding substrate.

Thermal Dissipation

In [28][38][27], the waveguides are tethered to a set of rails around the waveguide in the windowed section. By making the rails substantially wider than the waveguides, typically 5 µm to 10 µm, the heat from light absorbed in the waveguide is dissipated through the tethers and rails and into the substrate. While outside the scope of this thesis, we note that in a 2D system, multiple waveguides will be necessary to access the different symmetry directions in the PhC that we will discuss in section 2.4.3, and the tethering system will have to be adapted to accommodate this. Only preliminary work on suspending the waveguides over a window has been done here, but we shall discuss briefly a simple model for the problem of thermal dissipation.

Following the approach described in [33], the problem can be cast as an equiva-

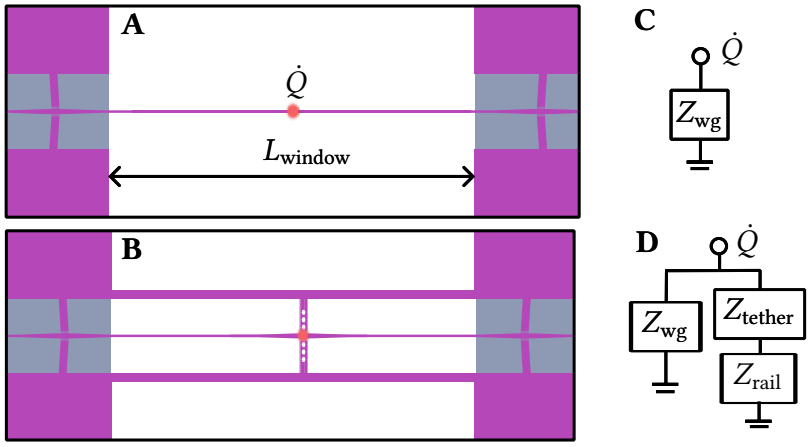

Figure 2.4: Thermal dissipation of a waveguide suspended over a window of length L_{window}. Purple indicates the Si_3N_4 , grey is the Si substrate, and white is the section where an optical window is opened in the substrate. Absorption of light is modeled as a point flux of thermal power $\dot{Q}$ at the center of the suspended section. **A** The waveguide is suspended over the window with no tethering. **B** The waveguide is tethered to two rails running alongside the waveguide. **C**(**D**) Equivalent thermal circuits for **A**(**B**).

lent thermal circuit as illustrated in fig. 2.4. The primary heating source will be the absorption of the guided light, which will be distributed throughout the structure. To simplify the problem, we assume that all the light is dissipated at a point in the center of the waveguide at a rate $\dot{Q}$ and assume that away from the window, the heat can be dissipated efficiently. The temperature change at the center of the waveguide is then given as

$$\Delta T = \dot{Q} Z, \tag{2.2.6}$$

where Z is the thermal impedance. For the waveguide suspended with no tethering and using the parameters shown in table 2.1, $Z = Z_{\text{wg}} = L_{\text{window}}/2A_{\text{wg}}\sigma_{\text{th}} = 333\,^{\circ}\text{C}\,\mu\text{W}^{-1}$, where the factor of $1/2$ accounts for thermal dissipation in both directions.

By tethering the waveguide to a set of rails, we see that the thermal impedance is now

$$Z = \left(\frac{1}{Z_{\text{wg}}} + \frac{1}{Z_{\text{tether}} + Z_{\text{rail}}} \right)^{-1} = 18\,^{\circ}\text{C}\,\mu\text{W}^{-1}, \tag{2.2.7}$$

with

$$Z_{\text{tether}} = \frac{1}{2} \left[\frac{L_{\text{tether}}}{w_{\text{tether}} d n_{\text{tether}} \sigma_{\text{th}}} + \frac{L_{\text{slab}}}{w_{\text{slab}} d \sigma_{\text{th}}} \right], \text{and} \tag{2.2.8}$$

$$Z_{\text{rail}} = \frac{1}{4} \frac{L_{\text{window}}}{w_{\text{rail}} d \sigma_{\text{th}}}. \tag{2.2.9}$$

evaluated for the parameters listed in table 2.1. The two contributions to Z_{tether} come from the tethering section close to the waveguide and the Si_3N_4 slab connecting it to

the rails, and the factor of 1/2 accounts again for dissipation in both directions. The 1/4 for the rails accounts for the two rails extending in both directions.

Waveguide parameters	symbol	Value
Waveguide width	w	500 nm
Waveguide thickness	d	200 nm
Suspended length	L_{window}	2 mm
Width of tether	w_{tether}	110 nm
Length of tether	L_{tether}	2 µm
Width of tether slab	w_{slab}	3.46 µm
Number of tethers	n_{tether}	15
Length of tether slab	L_{slab}	72 µm
Width of rail	w_{rail}	5 µm
Thermal conductivity Si_3N_4	σ_{th}	30 W m^{-1} °C [39]
Thermal resistance without rails	Z_{wg}	333 °C µW^{-1}
Thermal resistance with rails	Z	18 °C µW^{-1}

Table 2.1: Parameters for simulating thermal dissipation

The thermal impedance will approach that of the rails when adding more tether arrays, and the width of these rails can be adjusted to accommodate the required powers.

Mechanical Stress Relaxation

The waveguide is suspended over a V-groove in the substrate, and the waveguide is released from the substrate by etching away the silicon underneath the waveguide. The high tensile stress of the Si_3N_4 membrane is relaxed as the structure is released, which can cause a buildup of tension in certain regions if care is not taken to eliminate this. In particular, as the waveguide relaxes along its length, there is a deformation along the propagation direction, which can cause the tethers to snap. To minimize the stress along the direction of the waveguide, the left- and rightmost tether arrays are angled to provide an opposite force along the direction of the waveguide. This angle is determined numerically with a COMSOL simulation, where the total strain energy in the waveguide is minimized.

The waveguide design is imported into COMSOL as a 2D plane and extruded to a thickness of 200 nm. The ends of the tethers that connect to the other edges of the V-groove are constrained from moving, and the prestress of the Si_3N_4 layer, measured at 1.1 GPa is set as a material property for the waveguide. Symmetry reduces the computational domain size by 4, as indicated in fig. 2.5**A**. To account for the large aspect ratio

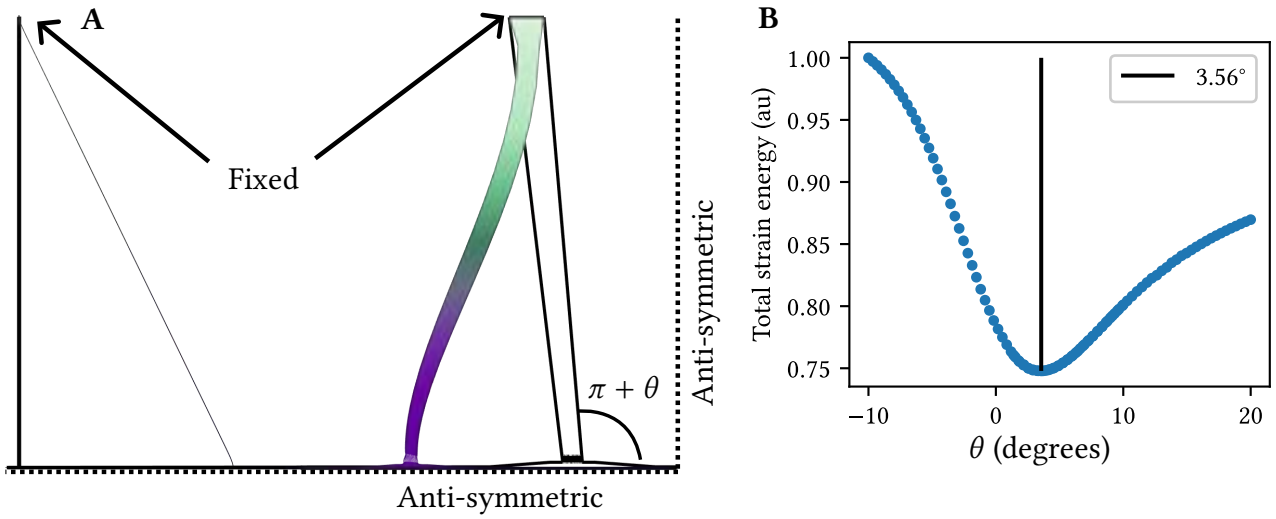

Figure 2.5: A The angle of the first node array helps redistribute the stress to minimize the stress on the single anchoring tether at the end of the waveguide. The wireframe shows the undeformed structure, and the colored structure is an exaggerated displacement profile after releasing the structure. **B** The stress relaxation with the waveguide release is simulated in COMSOL to find the optimal angle for the outermost tether arrays. The optimal angle is found by varying the tethering angle and solving for the total strain energy and is found to be 3.56°.

of the waveguide, the meshing is done by first meshing the 2D plane of the waveguide and then extruding this mesh using the sweep option in COMSOL. The system is solved for its stationary solution with the 'include geometric nonlinearity' option enabled to find the stress-redistribution of the released structure. The results of this simulation are shown in fig. 2.5**B** where we find that the total strain energy is minimized for an angle of 3.56°.

2.2.3 Waveguide Couplers

We pursue here two related approaches to coupling light from the waveguide to the outside, where the first utilizes an HP780 fiber positioned at the edge of the waveguide[37], and the second is a Y-coupler that is optimized for coupling light focused by a microscope objective into the waveguide[40].

Fiber Coupler

By designing the V-groove over which the waveguide is suspended such that a stripped HP780 fiber will have its core aligned with the tip of the waveguide, the field emitted from the tip of the fiber can be made to couple into the waveguide by having the tip of the waveguide aligned with the core of an optical fiber. The geometry of the V-

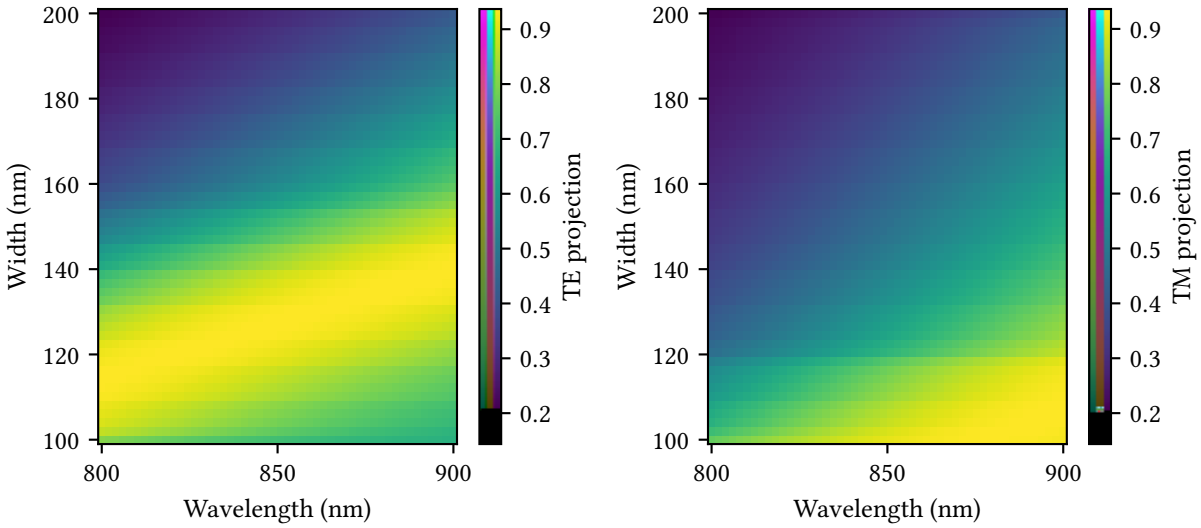

Figure 2.6: Mode overlap between a 780HP fiber and waveguide of varying widths as a function of wavelength, calculated for the TE and TM modes of the waveguide. We see that a waveguide width of around 128 nm achieves the maximum coupling of the TE mode around 850 nm.

groove will be discussed in section 3.6, and for now, we will discuss the design of the waveguide coupler. The waveguide coupler is shown in fig. 2.1D.

The mode-field diameter of the HP780 fiber is $(5 \pm 1)\,\mu$m at 850 nm, and as we see in fig. 2.2a, the TE and TM modes of the waveguide are confined close to the 500 nm waveguide. To increase the modal overlap, the waveguide is inversely tapered down, making the waveguide mode highly evanescent and increasing the transverse spread of the guided mode. The mode overlap is defined as [38]

$$\eta_{1\to 2} = \left| \Re\left\{ \frac{\mathcal{O}(\mathbf{E}_1, \mathbf{H}_2)\mathcal{O}(\mathbf{E}_2, \mathbf{H}_1)}{\mathcal{O}(\mathbf{E}_2, \mathbf{H}_2)} \right\} \frac{1}{\Re\{\mathcal{O}(\mathbf{E}_1, \mathbf{H}_1)\}} \right|, \quad \text{where} \quad \mathcal{O}(\mathbf{A}, \mathbf{B}) = \int dS \cdot (\mathbf{A} \times \mathbf{B}^*). \tag{2.2.10}$$

To maximize the overlap, we scan the waveguide's width at the tip of the coupler and calculate the overlap of the TE and TM modes of the waveguide with the fiber mode. The mode profiles for both the waveguide and the fiber are computed using the mode solver in Lumerical[1] with the parameters parameters listed in table 2.2. The results of this scan are shown in fig. 2.6, where we see that a waveguide width of around 1.3 µm maximizes the overlap for the TE mode, while narrower waveguides increase the TM projection. We chose a nominal width of 128 nm for the waveguide at the tip of the coupler.

[1]Lumerical Inc. **FDTD:** 3D Electromagnetic Simulator

Table 2.2: Parameters for Coupler simulations fiber

HP780 parameters [38]	Value
Core diameter	4.4 µm
Cladding refractive index (n_{clad})	1.4570
Core refractive index (n_{core})	1.4628
Si_3N_4 parameters	
n	1.99
Thickness	200 nm

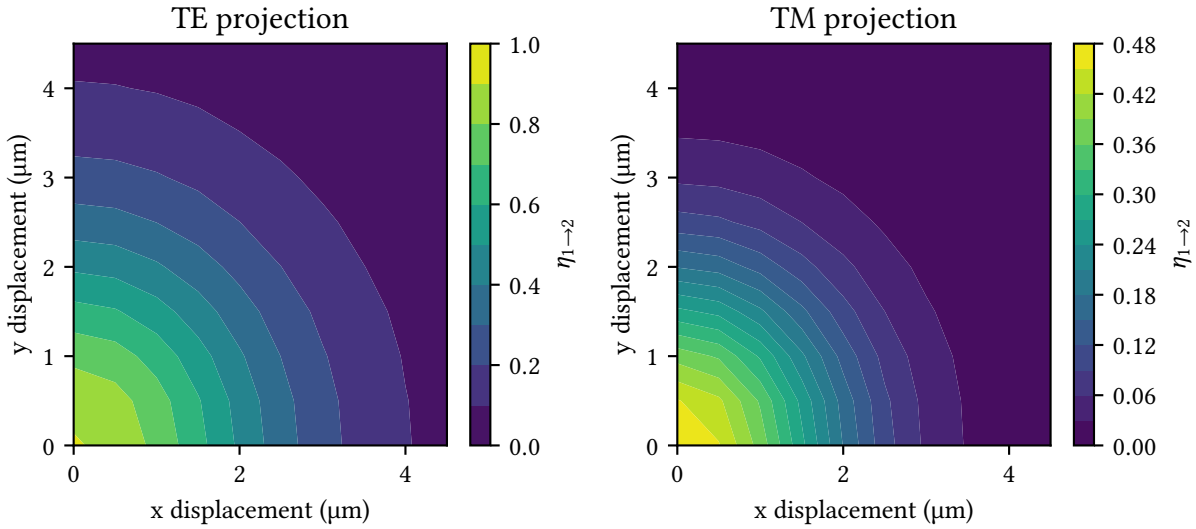

Figure 2.7: Mode projection from the fiber to the waveguide for the TE and TM mode at 850 nm as a function of the transverse displacement of the fiber from the waveguide. We observe a more rapid attenuation for the TM mode than for the TE mode.

To stabilize the end of the coupler, a single tether is added at a short distance from the tip of the waveguide. The tether will cause scattering losses and create reflections, but it is necessary for the waveguide to keep the coupler suspended. The scattering from the tether is minimized by making the tether as thin as possible, but we limit ourselves to a nominal tether width of 100 nm, as thinner tethers are more challenging to fabricate with a high yield. To estimate the scattering from this tether, we do an FDTD simulation as shown in fig. 2.8, where a Gaussian mode of w_0 =2.5 µm is focused onto the tip of the waveguide. The transmission is measured as the projection of the power propagating through a monitor at the right edge of the domain onto the fundamental modes of the tapered waveguide.

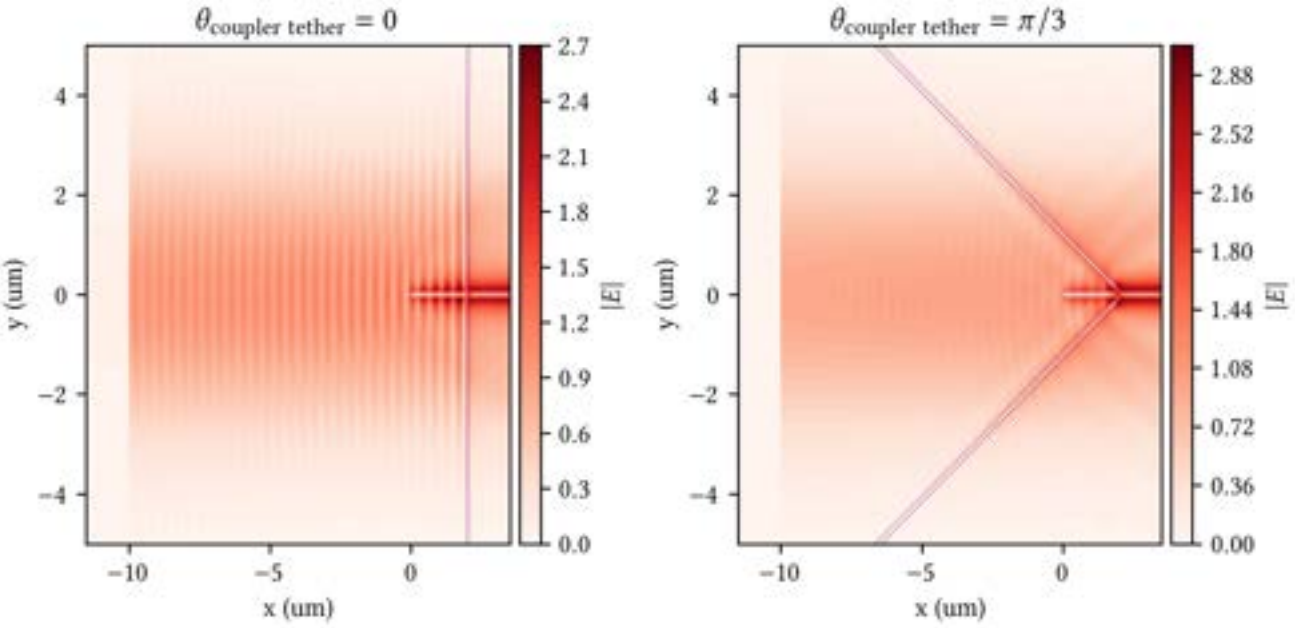

Figure 2.8: FDTD simulations of a Gaussian mode injected into a tapered waveguide coupler. In the left figure, the tethers are normal to the waveguide, where we see strong reflection fringes. On the right, the tethers are angled at $\pi/3$ with respect to normal, and we see a strong suppression of the reflection fringes.

The fibers must be glued to the chip after alignment using vacuum-compatible glue to integrate this system with the atomic experiment. This approach was used in the group of Kimble, and details on this procedure can be found in [33][38]. For optical measurements at ambient pressures, the fiber-coupled design is convenient as it makes coupling to the waveguide simple and robust, with the caveat that it is sensitive to the precision with which the center of the V-groove aligns with the waveguide. We will discuss this problem in section 3.4.

Free Space Coupling

Instead of using a cleaved fiber near the waveguide, the light can be injected from free space by focusing onto the waveguide with a microscope objective. This solution has the appeal that it avoids having to deal with fibers in the vacuum chamber, simplifying the chamber assembly and vacuum pumping. It also provides more control over the polarization state and the spatial mode of the injected light. This design also offers more freedom in the design of the device. The physical dimensions of the fiber dictate the dimensions of the V-groove, but with free space coupling, this is no longer a requirement. Narrowing the slot could improve device stability and reduce write times

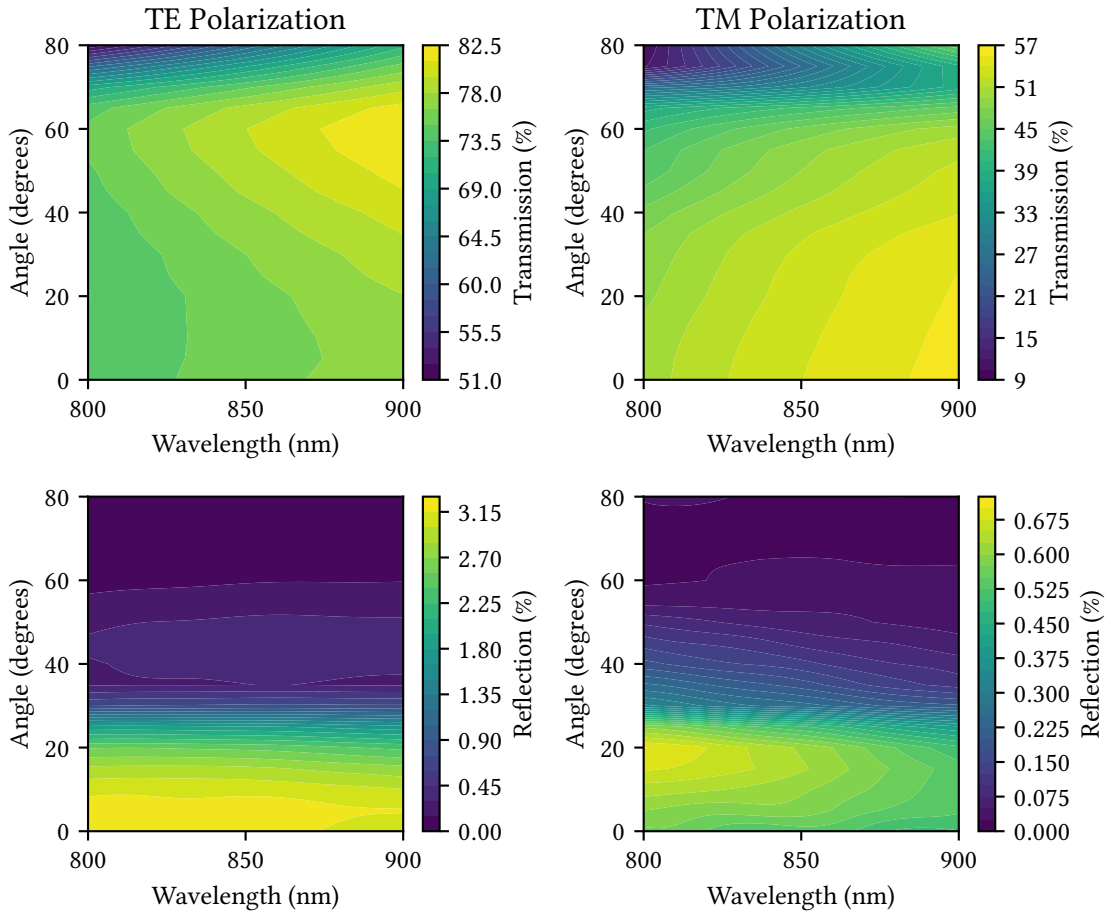

Figure 2.9: Scan of the angle of the tethers in the Y-coupler. The transmission and reflection are plotted for different angles of the tethers at different wavelengths.

in the e-beam writer. As the fiber does not occupy the half-space next to the end of the waveguide, there is also additional freedom in designing the anchoring tethers. In [32], they present a Y-shaped end coupler, where they find that by angling the tethers at $\pi/3$ from normal, back-reflection from the tethers can be reduced. We perform FDTD simulations to verify this result, where the angle of the tethers are scanned, and find that this design can suppress reflections at the cost of decreasing transmission by $\approx$10%. The results are shown in fig. 2.9.

As a note for future studies, the design of these tethers is a good candidate for topology optimization, where the shape of the tethers could be optimized to minimize back-reflection and optimize the transmission[41].

When coupling from free space, one should also consider aberrations from the highly focused light going through the side of the vacuum chamber window. On the

other hand, the freedom offered in shaping the mode of the incoming light outweighs this challenge. Using spatial light modulators (SLM), we can even access the waveguide's asymmetric modes, which might present interesting options.

2.2.4 Geometry Considerations for Multi-Port Devices

If we want access to multiple waveguides simultaneously in the future, this would have to be accomplished through a single microscope objective using, for example, an SLM or acoustic-optic deflectors. To keep all waveguides within the field of view of the objective, the waveguides must be close to one another, and the main limitation in how closely the waveguides can be placed is the distance of the coupler to the edge of the chip. If the waveguide is located too far away from the edge of the chip, the tightly focused beam will be clipped by the edge of the V-groove. To have bi-directional access to all symmetry axes of a hexagonal crystal, a total of 12 waveguides, ie, six on either side of the chip. With our current microscope objective, the field of view is 400x400 µm, so to fit six waveguides on either side of the chip, the waveguides must be spaced at most ≈66 µm apart. Allowing for a bit of space between each V-groove leaves a maximal width of ≈40 µm for each V-groove. Because of the geometry of the geometry of the V-groove, shown in fig. 2.10**B**, the distance from the center of the waveguide to the closest part of the V-groove is $2/\sqrt{3}w$ where w is the width of the waveguide. The waveguide should be <140 µm from the edge of the chip to avoid clipping the beam on the sides of the V-groove. If using the Y-coupler design, the tethers are anchored at a distance of $w/(2\cos(\theta_{\text{coupling tether}}))$ further toward the edge of the chip, making the requirement for precise cleaving of the chip even more important. In section 3.6, we present a method to reliably cleave the chip < 50 µm from the end of the waveguide.

2.3 Propagation Loss Measurements

The propagation loss in the waveguide is a central characterization parameter as it is a good indicator of the quality of the fabrication process and a key parameter for the performance of the devices. In part, this is because the optical power injected into the waveguides is limited by the ability of the device to dissipate the heat generated by the absorbed light. If too much light is used, it will permanently damage the device [42]. Additionally, when using the waveguides as a measurement port for the photonic crystal slabs, the linear loss in the waveguide will limit the signal-to-noise ratio of the measurements, and light scattered from the waveguide may interact deleteriously with atoms close to the surface.

For a linear waveguide, i.e., one without any bends or other features that would cause light to scatter out of the waveguide, the loss is primarily due to the material absorption and scattering at the interface between the waveguide and the cladding.

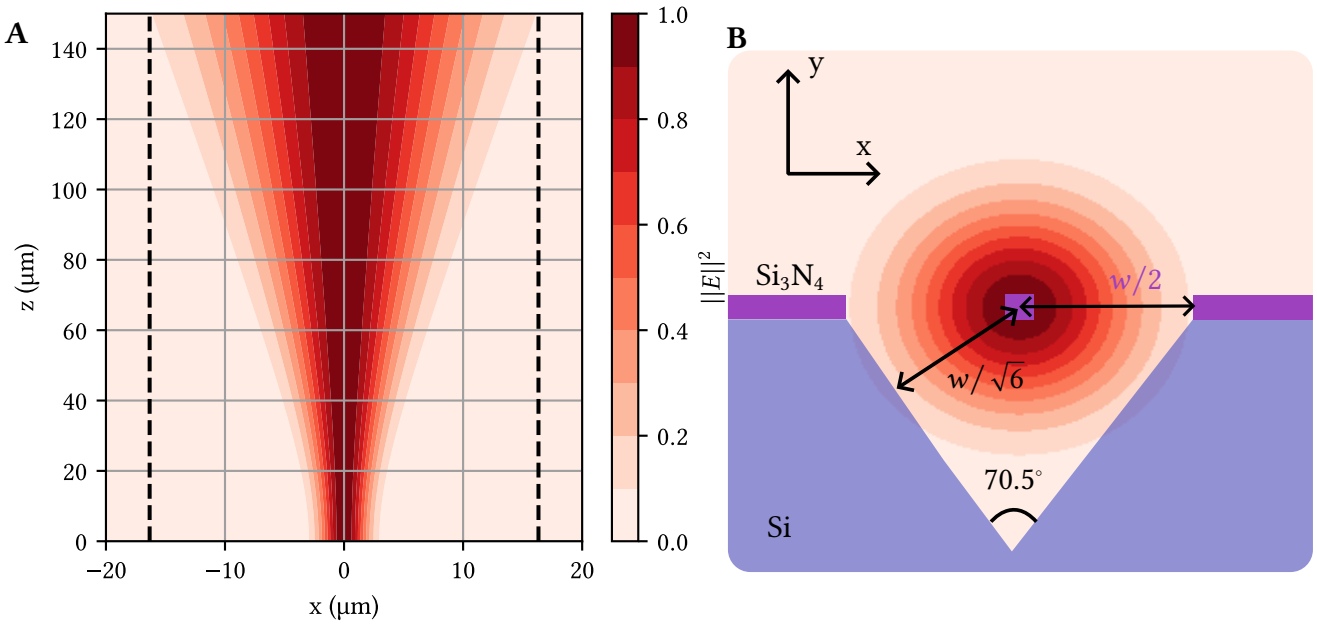

Figure 2.10: **A** The intensity contours of a Gaussian mode profile with $w_0 = 2.5\mu$m. The vertical lines indicate the distance from the center of the mode profile to the part of the V-groove closest to the waveguide, as shown in **B** for a groove of width w=40 µm. **B** Due to the geometry of the V-groove, the shortest distance from the waveguide (purple square at the center) to the substrate is $w/\sqrt{6}$, where w is the width of the opening in the Si_3N_4 .

The power in the waveguide is given by $P(z) = P_0 e^{-\alpha z}$, where α is the propagation loss and is often provided in dB cm^{-1}. Stochiometric Si_3N_4 has negligible absorption in the near-infrared (NIR)[43], and the propagation loss is dominated by scattering. For the TE mode, scattering is primarily due to roughness at the edges of the waveguide caused by the dry etch. For a slab waveguide, the scattering exponent can be shown to scale with the waveguide with w^{-4} [44]. Making the waveguides wider may decrease the scattering loss at the cost of introducing a second TE mode.

In the thesis of Su-Peng Yu [33] the propagation loss is reported at 0.05 % per 100 µm = 0.35 dB cm^{-1} for the TE polarization for an air clad Si_3N_4 waveguide at 903 nm. This propagation loss was achieved after careful optimization of their fabrication process, and as such, it may serve as a point of reference for our endeavors.

There are multiple approaches to measuring propagation loss, with the most common approach being the cutback method, where waveguides of varying lengths are fabricated, and the transmission through the waveguides is measured. The linear loss is then determined by fitting the transmission to an exponential decay as a function of waveguide length. This method, while simple and generally robust, has the problem that it is not possible to distinguish between the propagation loss and loss from mode mismatch at the couplers. In most cases, optimizing coupling is simply aligning

the input and output fibers. In our case, in contrast, the coupling into the waveguide is done by slotting a stripped optical fiber into a V-Groove, which has been designed such that the fiber core aligns with the waveguide. This method is more straightforward than free space coupling but provides much less control over the mode matching. If the V-Groove is not correctly aligned with the waveguide, for reasons that will be discussed in section 3.4 and section 3.6, the input coupling is reduced as shown in fig. 2.7. This displacement is fixed when the device is fabricated. If it is not identical between nominally identical devices, there is no way to separate propagation loss from coupling loss in a cutback measurement. Migrating to free space coupling would solve this problem, but we decided that sticking with fiber coupling for this project was the most time-efficient way to proceed.

To measure the propagation loss independent of the coupling loss for the fiber-coupled devices, we add Fabry-Perot resonators of varying lengths to untethered sections of the waveguide and infer the propagation loss from the Finesse of the resonances.

2.3.1 Distributed Bragg Reflector Cavities

To form the mirrors of the optical resonator, we opt for Distributed Bragg Reflector (DBR) mirrors. There are many ways to design DBR mirrors, and we chose to add holes to the waveguide to form the mirrors. Using holes had the appeal of being similar to our endeavors in creating a 2D photonic crystal, but as we shall discuss in section 3.5, the high aspect ratio of the holes in the waveguide limits how small we can make the holes. This, in turn, limits the mode-matching between the plain waveguide and the DBR section, causing scattering and thereby limiting the reflectivity.

To understand the limitations of the DBR mirrors, it is helpful to consider the simple case of light propagating in a waveguide with effective mode index n_1 and then encountering a region of alternating refractive index n_1 and n_2 with each layer having a thickness of $\lambda/4n$, $n \in \{n_1, n_2\}$. For a stack of N layers, the reflectivity of the DBR mirror is given by [45]:

$$R = \left[\frac{(n_2)^{2N} - (n_1)^{2N}}{(n_2)^{2N} + (n_1)^{2N}}\right]^2 . \tag{2.3.1}$$

This reflectivity is at the center of the stopband of the DBR f_0 and gives the stopband width

$$\frac{\Delta f_0}{f_0} = \frac{4}{\pi} \arcsin\left(\frac{n_2 - n_1}{n_2 + n_1}\right). \tag{2.3.2}$$

This model neglects the mode-matching between the waveguide and the DBR section and the scattering that occurs at the interface between the two sections, but it does provide some intuition for the design of the DBR mirrors. The difference in refractive

Parameter	Value	Description
N	15	Total number of holes
r_{max}	100 nm	Nominal radius of holes
r_{min}	66 nm	Minimal vertical radius of tapered holes
a	315 nm	Distance between holes
N_{taper}	5	Number of tapered holes
R	97 %	Simulated TE Reflectivity at 852 nm

Table 2.3: Nominal parameters for the DBR design.

index between the two layers should be large to obtain a wide stop band. The peak reflectivity also scales with the index contrast, but a low refractive index contrast can be compensated for by increasing the number of layers. In our case, the refractive index is modulated by the presence of holes in the waveguide, and the low (high) refractive index layers are the sections of the waveguide with (without) holes. The index contrast can be controlled by the size of the of holes, but is also influenced by the width and thickness of the waveguide, and we use FDTD simulations to get the reflectivity spectrum for the devices.

The transition from the nominal waveguide to a section with holes causes scattering into other modes. The scattering can be mitigated to some extent by adiabatically increasing the hole size, but the fabrication limits the minimal hole size. The holes are linearly tapered from r_{min} to r_{max} over n_{taper} holes.

The parameters used for the DBR design are shown in table 2.3, and the design is shown in fig. 2.11. The parameters were found from sweeps of the parameters and produced a (local) maximum in the reflectivity of the mirrors at 852 nm.

The simulated reflectivity of the DBR mirrors is 97 % at 852 nm and is primarily limited by scattering at the interface between the DBR and the plain waveguide. A larger number of holes reduces the transmission but leaves the reflectivity mostly unchanged, suggesting that scattering is limiting the reflectivity.

Other DBR designs, such as modulating the width of the waveguide, allow for a much smoother adiabatic mode transfer [46][33] and can, therefore, give much higher reflectivities. The appeal of using holes is its similarity to our 2D PhC designs, and we believed a reflectivity of 97 % to be sufficient for our purposes.

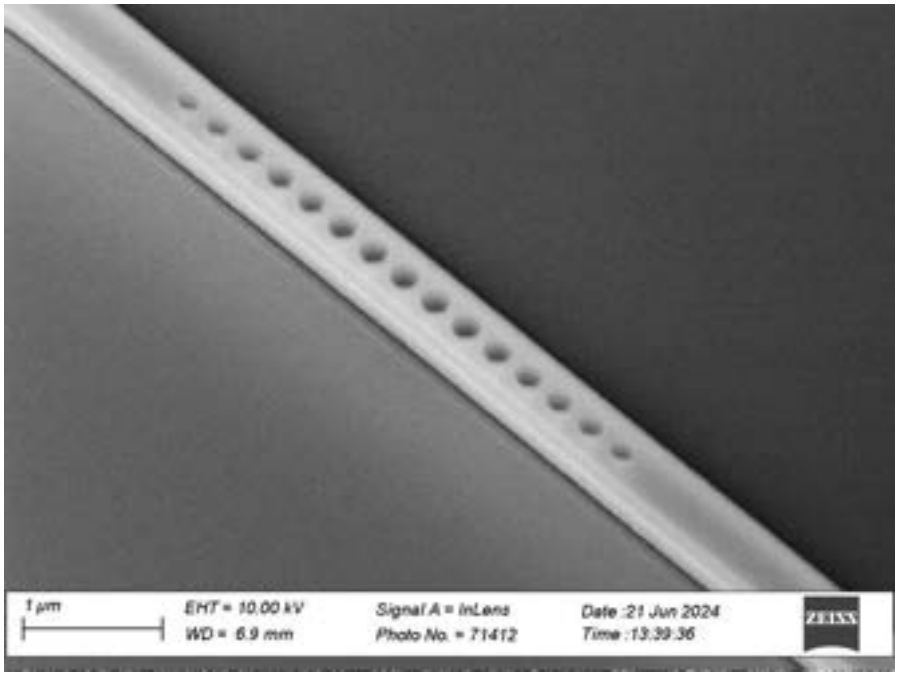

Figure 2.11: SEM Micrograph of DBR mirror. The holes are tapered to increase reflectivity.

2.3.2 Fabry-Perot Resonators

With a pair of DBR mirrors separated by L_{cavity}, we form a Fabry-Perot resonator. The Finesse of the resonator is given by [47]

$$\mathcal{F} = \frac{\pi}{2 \arcsin\left(\frac{1-\sqrt{\rho}}{2\sqrt[4]{\rho}}\right)}, \tag{2.3.3}$$

where ρ is the total power left in the cavity after one roundtrip. For a Fabry-Perot of length L resonator with two mirrors of nominally identical reflectivity R and an intrinsic propagation loss of α, $\rho = R^2 e^{-2\alpha L}$. With this simple model, we can then calculate the Finesse of the resonator as a function of cavity length for different propagation losses. The results are shown in fig. 2.12, from which we conclude that for realistic propagation losses, a measurement of cavities of varying lengths between 50 µm and 450 µm should be sufficient to determine the propagation loss of the waveguide. We will return to the actual measurement of these devices in section 4.2.1.

2.4 Photonic Crystal Slabs

The 2D PhC is the key component of the photonic device for the LAQS experiment, as it is in this section that we can engineer the interaction of the atoms via the dispersion in

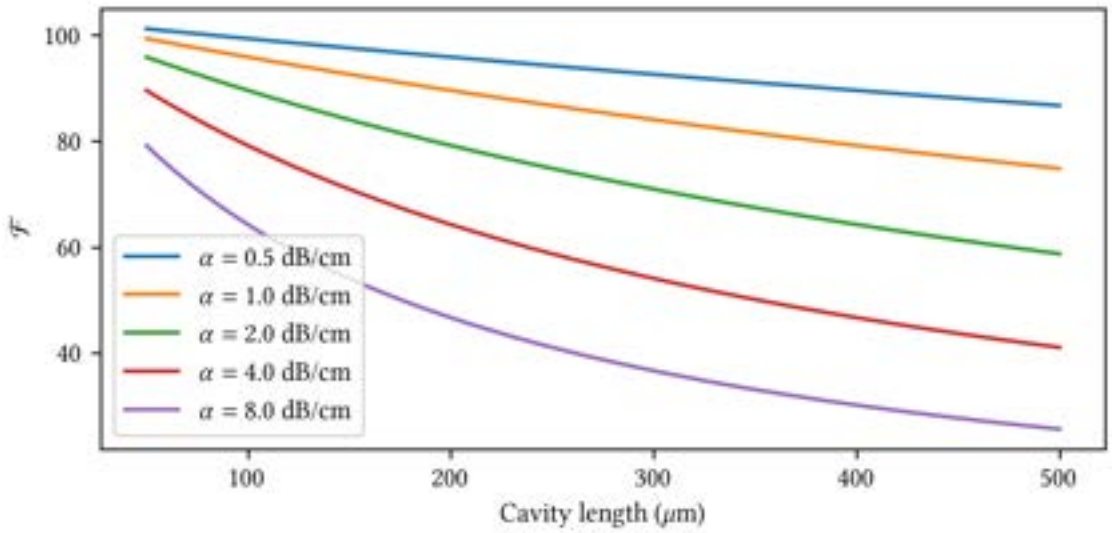

Figure 2.12: Finesse of the Fabry-Perot resonator as a function of cavity length for different propagation losses and mirror reflectivity R =97 %.

the plane of the crystal. As a platform to test our fabrication capabilities, we follow the designs presented by Yu et al. in [28], where they consider two different geometries of 2D PhCs. The first is a square lattice of holes perforated in the slab, and the second is a hexagonal lattice of hexagonal holes. For the hexagonal lattice, we also pursue a design with a round hole as this may prove somewhat more straightforward to fabricate at the cost of slightly altered dispersion properties.

We briefly review the theory of 2D PhCs, discuss their design for our platform, and finally present simulations of tolerances on the design parameters.

2.4.1 2D Periodic Structures

As in section 2.2.1, the dispersion is the relation between the light frequency and the propagation constant of the solutions to eq. (2.2.1). In the case of the 2D PhC, the dielectric function now has discrete symmetries instead of continuous ones such that $\varepsilon(\mathbf{r}) = \varepsilon(\mathbf{r}+\mathbf{A})$ where $\mathbf{A}$ is an arbitrary sum of the integer-multiples of the unit-vectors of the photonic crystal $\mathbf{a}_i$.

The solutions to eq. (2.2.1) are now Bloch modes, which are of the form

$$\mathbf{E}(\mathbf{r}) = \mathbf{E}_{n,\mathbf{k}}(\mathbf{r})e^{i\mathbf{k}\cdot\mathbf{r}}, \tag{2.4.1}$$

where $\mathbf{k}$ is the Bloch wavevector, and $\mathbf{E}_{n,\mathbf{k}}(\mathbf{r})$ with the same periodicity as $\varepsilon(\mathbf{r})$. Here it is implied that $\mathbf{k} \equiv \mathbf{k}_{\|}$ is only the part of the wavevector that is parallel to the plane of the PhC, and the dispersion is now $\omega = \omega_n(\mathbf{k})$.

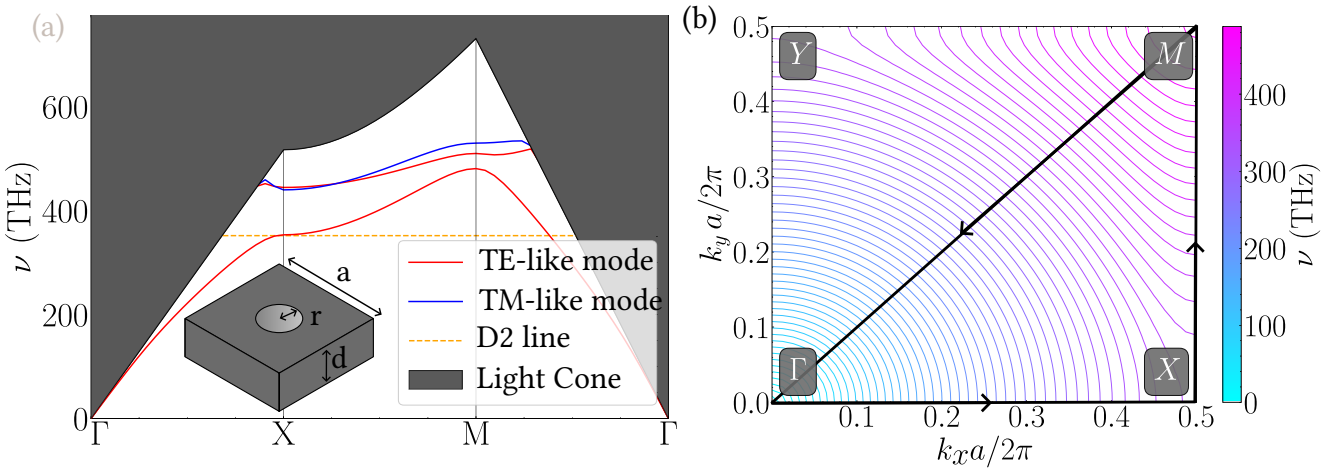

Figure 2.13: (b) The dispersion of PhC with $a = 290$ nm, $r = 103$ nm and $d = 200$ nm where we note the flat dispersion at the D2 line. The contour in k-space is indicated by the triangle in (b). The inset shows the unit cell of the square geometry. (b) The equifrequency contours for the TE-like dielectric mode in k-space, where we note that along the $k_{\Gamma X}$ direction, there is a region of flat EFCs around 390 THz, which causes self-collimation. Figures adapted from [49] with permission.

The periodicity of the lattice also implies periodicity in k-space, and thus only wavevectors within the first Brillouin zone are considered[48][13]. As the space spanned by the reciprocal lattice vectors is now two-dimensional, the bands are now instead 'sheets' in a ω,**k**-space. It is customary to present a 2D projection of the dispersion, where the frequency is plotted as a function of the wavevector along a high-symmetry path in the Brillouin zone. The path in k-space is shown as an inset in the corresponding band diagrams. We only consider modes under the light cone where $|\mathbf{k}| < \omega/c$.

For a PhC formed by holes in a slab, the first (second) energy band will have the majority of the energy confined to the dielectric (air) and is therefore named the dielectric (air) band. We limit ourselves to studying the TE and TM modes here, although the odd-odd and even-even modes could potentially be utilized by using an asymmetric Bragg grating [33].

All dispersion curves here are calculated using MPB, where the unit cell has the dimensions of the corresponding geometry in the x, y plane and a sufficiently large size in the z direction that the evanescent tail of the modes do not interact with the z boundary of the domain. Convergence is found for a domain height of $h = 5a$ and a resolution of 64 pixels per lattice constant a.

2.4.2 Square Geometry

In the square geometry, the lattice vectors are $\mathbf{a}_1 = \hat{x}$ and $\mathbf{a}_2 = \hat{y}$, and the unit cell is a square with side length $a = 290$nm and hole radius $r = 103$nm. For a 200 nm thick slab of Si_3N_4 , it is not possible to open a bandgap under the light line in the square geometry due to the modest index contrast of Si_3N_4 to air, so the dynamics that can be explored in this geometry are dissipative. With the chosen parameters, the D2 line of Cesium aligned with the slow light section at the X point to increase the light-mediated atom-atom interaction while also allowing light at the D1 wavelength (895 nm) to propagate in the crystal.

An interesting feature of this geometry is that of self-collimation[35][34], where light is confined along the diagonals of the square lattice. This can be understood as a consequence of the flat region of equifrequency-curves (EFCs) shown in fig. 2.13b. The confinement happens because the two-dimensional group velocity

$$\vec{v}_g = 2\pi\nabla_{\vec{k}}\nu(\vec{k}), \tag{2.4.2}$$

is always perpendicular to the EFCs, and thus, for frequencies where the EFCs are flat, a large number of the $\mathbf{k}$-vectors will propagate in the same direction. It is worth noting that the self-collimation for this set of parameters happens around 390 THz, which is far blue-detuned from the D2 line. By changing the pitch of the lattice to 330 nm, the self-collimation can be brought close to the D2 line, but at the cost of not having the slow-light section at the X point aligned with the D2 line. The self-collimation effect can be used to mode-match from the 1D waveguide mode to the 2D PhC mode, as mentioned previously, and it could potentially be a useful tool for the design of the atom trapping potential. Directional spontaneous decay in hexagonal geometries has also been recently studied [50].

This effect can be explored further using FDTD simulations, where a radiating dipole is placed in the vicinity of the photonic crystal and excited at different frequencies and dipole orientations to see the effect of the self-collimation, and the results are shown in fig. 2.14. The simulations used Lumerical FDTD, where a radiating dipole was placed near the PhC, and the emission was calculated for different frequencies and dipole orientations. This directionality of the emission in the 2D structures is of particular interest when considering the problem of coupling light from the 1D waveguide to the 2D photonic structure, as the self-collimation can be used to efficiently guide light from the 1D coupler to a specific region of the PhC by limiting the radial spread of $\mathbf{k}$ as the 1D mode encounters the PhC[35].

2.4.3 Hexagonal Geometry

In the hexagonal geometry, the lattice vectors are $\mathbf{a}_1 = \sqrt{3}/2\hat{x} + \hat{y}/2$, $\mathbf{a}_2 = \sqrt{3}/2\hat{x} - \hat{y}/2$. The dispersion curve for a hexagonal lattice is shown in fig. 2.15, where there is a

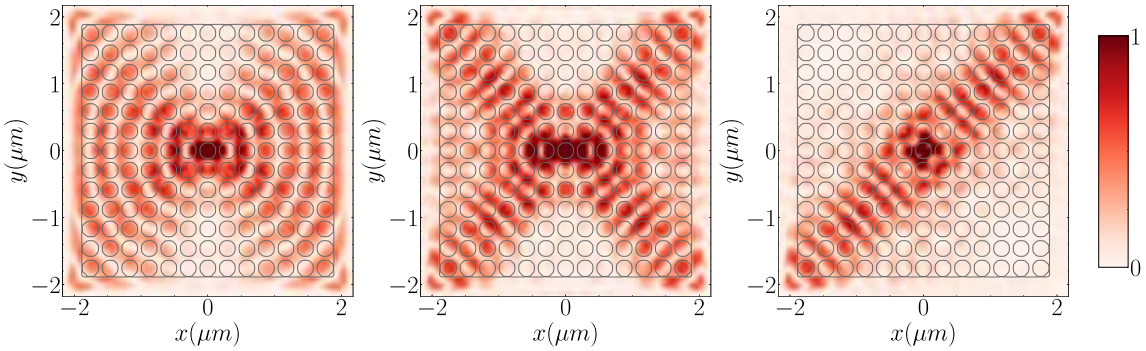

Figure 2.14: Emission of a radiating dipole in the PhC slab, where the color indicates the intensity of the field. On the left, the dipole is oriented with the y axis and radiates at 320 THz, far from the flat EFC region, and we see that self-collimation is not present. In the central panel, the dipole is still oriented along the y axis and now radiates at 390 THz, and directional radiation along the diagonals can be seen. In the third panel, the dipole is oriented along $\hat{y} - \hat{x}$ and emits light at 390 THz. The emission is focused along one diagonal. Figure courtesy of J. Martínez de Aguirre Jokisch [49].

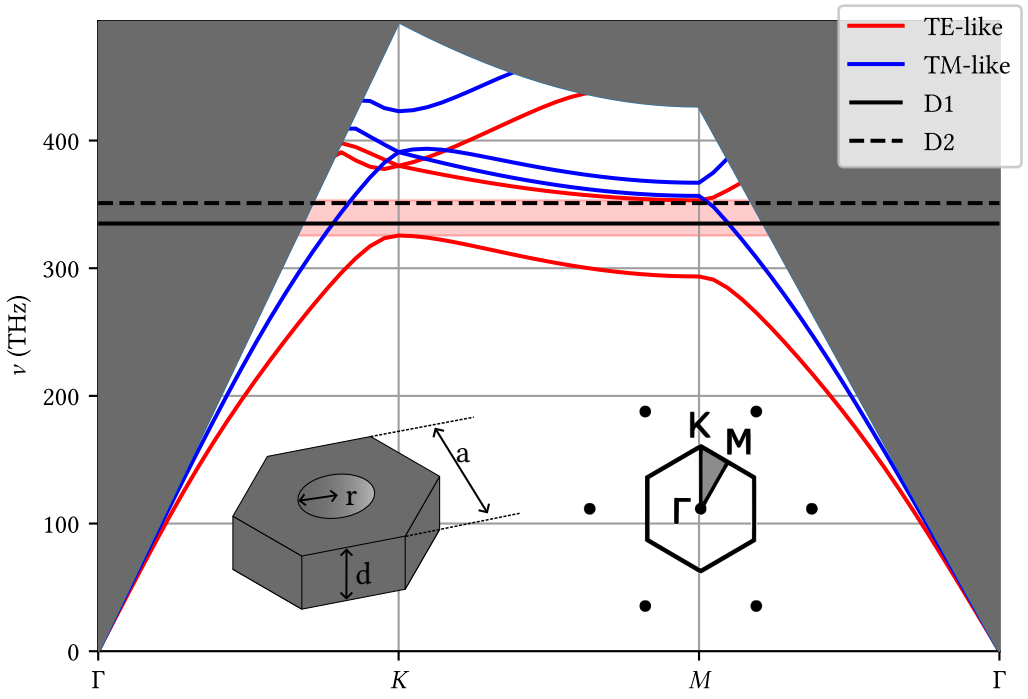

Figure 2.15: Band diagram for the hexagonal PhC with $a = 405$ nm, $r = 115$ nm and $d = 200$ nm. We see a partial bandgap under the light line for the TE modes. The inset shows the path traced along the high symmetry points in the Brillouin zone, as well as the geometry of the unit cell.

Parameter	Description
Γ_0	Free-space emission rate
$\Gamma = \Gamma_{2D} + \Gamma'$	Total emission rate in the presence of the PhC
Γ_{2D}	Emission rate into waveguide
Γ'	Radiative emission rate
J_{ij}	Coherent interaction rate
$F_p = \Gamma/\Gamma_0$	Purcell Factor
$C = \Gamma_{2D}/\Gamma'$	Cooperativity

Table 2.4: Overview of the figures of merit that can be estimated from the FDTD simulations.

partial bandgap under the light cone for the TE mode. The target parameters here are $a = 405$nm, $r = 115$nm, and $d = 200$nm, which are chosen to align the upper band-edge at the K point with the D2 line of Cs at 351 THz. The design presented in [28] has hexagonal holes instead, primarily to narrow the bandgap to move the D1 close to the band edge, but this is not an immediate priority here.

If the atomic transition is inside the bandgap, light emitted into the structure will be evanescent, and the emission of excited atoms into the structure is suppressed. To investigate the effect of the photonic crystal on the emission of atoms into the structure, we turn to FDTD simulations to calculate the emission of a radiating dipole in the vicinity of the PhC.

2.4.4 FDTD Simulations for Estimating Figures of Merit

Our master's student Beñat did these simulations, and a more detailed description of the simulations and theory can be found in his thesis [49]. Here, we provide a brief review of the principle of how these simulations can be used to estimate the Purcell enhancement, F_p, the β-factor, and the coherent interaction strength J_{ij} from eq. (1.1.11). An overview of the various FOM is shown in table 2.4.

The dyadic Green's function $\mathbf{G}(\vec{r}, \vec{r}', \omega)$, describes the electromagnetic field at position $\mathbf{r}$ created by point source at $\mathbf{r}'$ with dipole moment μ

$$\mathbf{E}(\mathbf{r}) = \frac{\omega^2}{\epsilon_0 \epsilon_r c^2} \mathbf{G}(\mathbf{r}, \mathbf{r_0}, \omega) \cdot \boldsymbol{\mu}. \tag{2.4.3}$$

It is a symmetric 3x3 matrix where each element can be obtained from the computed field of dipoles with different orientations at $\mathbf{r}_0$.

The LDOS is given by the imaginary part of the Green's function, and the spontaneous emission rate for a two-level system can be calculated as [14]

$$\Gamma = \frac{2\omega_0}{3\hbar\epsilon_0} |\boldsymbol{\mu}|^2 \rho_\mu(\mathbf{r}_0, \omega_0), \tag{2.4.4}$$

with

$$\rho_\mu(\mathbf{r}_0, \omega_0) = \frac{6\omega_0}{\pi c^2}\left[\mathbf{n}_\mu \cdot \mathrm{Im}\{\mathbf{G}(\mathbf{r}_0, \mathbf{r}_0; \omega_0)\} \cdot \mathbf{n}_\mu\right] \tag{2.4.5}$$

being the partial LDOS for a dipole oriented along $\mathbf{n}_\mu$ at $\mathbf{r}_0$. The Purcell factor is then defined as the ratio of the spontaneous emission rate in the presence of the photonic crystal to the spontaneous emission rate in free space and is given by

$$F_p = \frac{\Gamma}{\Gamma_0} = \frac{6c}{\omega}\hat{n}_{\boldsymbol{\mu}} \cdot \mathrm{Im}\left[\mathbf{G}(\mathbf{r_0}, \mathbf{r_0}; \omega)\right] \cdot \hat{n}_{\boldsymbol{\mu}}. \tag{2.4.6}$$

The Purcell factor is interesting because it lets us know how efficiently spontaneous decay into the photonic mode is. The simulation uses Lumerical, where a dipole is placed in the center of a hole in a finite-size photonic crystal, and the emission is calculated for different frequencies and dipole orientations.

To evaluate the cooperativity, the contributions to the total decay must be resolved into the two channels $\Gamma = \Gamma_{2D} + \Gamma'$. This is done by monitoring the power radiated through a box-'hat' sitting on top of the crystal and the total power radiated by the dipole. The ratio between the latter and the former gives the cooperativity. The simulations are shown in fig. 2.16, where it should be noted that these simulations are performed for a slightly different geometry, where the upper band edge is not aligned with the D2 line but around $\approx$ 380 THz, but this is just a matter of scaling the geometry to the correct frequency.

We see that radiation in the bandgap is suppressed both into the waveguide and the radiative modes. The maximal Purcell enhancement and cooperativity are found at the upper band edge, where $C \approx 10$, which is a promising result. The fact that both F_p and C are much higher at the upper band edge than the lower can be understood by considering the intensity profile of the modes at the band edges, which we shall return to shortly. Since the structure is rotationally symmetric, the X and Y dipole orientation is expected to give identical results, which we also find to be the case within the numerical error of the simulations. Convergence of the results was carefully considered and is documented in [49]. These effects were also found to be strongly dependent on the position of the atom relative to the PhC, and in particular to displacements along the z. The maximal suppression in the bandgap was reduced by $\approx$ 50%/100 nm.

We consider the real part of the Green's function to evaluate the coherent interaction strength J_{ij}. For Cs atoms in hyperfine states $|F\rangle$, $|F'\rangle$, the interaction strength is given by [51][28]

$$J_{ijqq'} = \frac{\mu_0 \omega_{qq'}^2}{\hbar}\left|\left\langle F \left\| \boldsymbol{\mu} \right\| F' \right\rangle\right|^2 \hat{e}_q \cdot \mathrm{Re}\left\{\mathbf{G}(r_i, r_j, \omega_{qq'})\right\} \cdot \hat{e}^*_{q'}, \tag{2.4.7}$$

where $\omega_{qq'}$ is the transition frequency between the states $|F\rangle$ and $|F'\rangle$, $\hat{e}_q$ is the polarization of the light, and $\mathbf{r}_i$ is the position of the $i^{[th]}$ atom. If we consider the

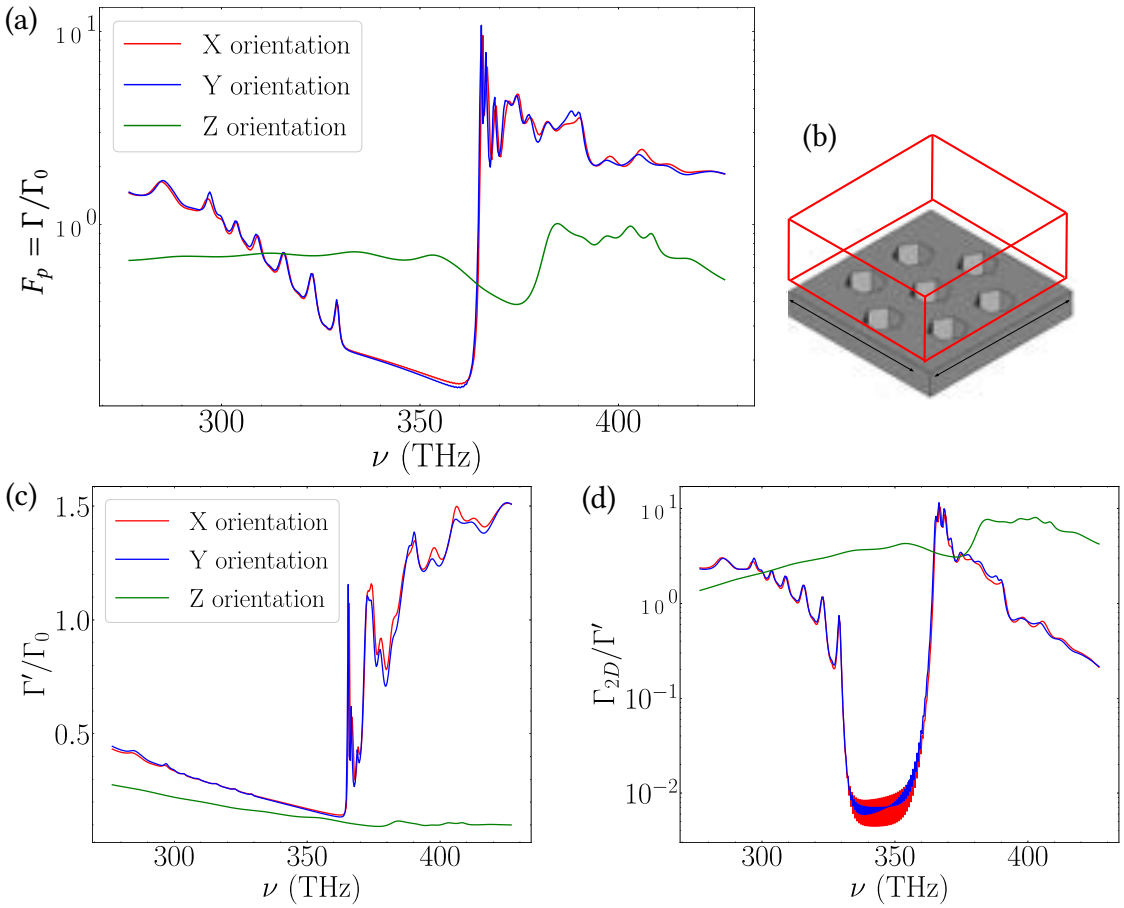

Figure 2.16: FDTD simulations of a radiating dipole in the hole of a photonic crystal. The three colors correspond to different orientations of the dipole. (a) The Purcell enhancement as a function of frequency. (b) Illustration of the box method for calculating the cooperativity. Calculating the power radiated through the sides of this box allows us to separate the radiation into Γ_{2D} and Γ'. (c) Suppression of radiative decay as a function of frequency. (d) The cooperativity as a function of frequency. The rapid fringing in the bandgap section is a numerical artifact of the finite simulation volume. Figure courtesy of B. Martínez de Aguirre Jokisch [49].

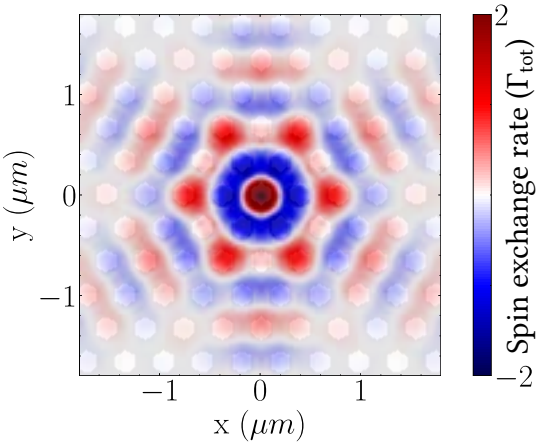

Figure 2.17: Spatial dependence of the coherent interaction strength J_{ij} for the $|F = 4, m_f = 4\rangle \Leftrightarrow |F = 5, m_f = 5\rangle$ transition. The color indicates the magnitude and sign of the interaction strength in units of Γ_{tot}. The value at the dipole position diverges and is omitted. Figure courtesy of B. Martínez de Aguirre Jokisch [49].

closed $|F = 4, m_f = 4\rangle \Leftrightarrow |F = 5, m_f = 5\rangle$ transition, the selection rules dictate that the light must be σ^+ polarized. In this case, the spatial dependence on J_{ij} is shown in fig. 2.17. The sign and magnitude of the interaction strength are spatially dependent. If the atoms can be positioned using, e.g., optical tweezers, the interaction between individual atoms can be controlled. By positioning the atoms in a super-lattice, a many-body system with the desired atom-atom interactions can be engineered through the position-dependent interaction strength[28].

In [52], they show that when the atomic transitions lie in the bandgap, the spatial dependence of $|J_{ij}| \propto K_0(|\mathbf{r}_{ij}\Delta/A)$ where K_0 is a modified Bessel function of the second kind, A is the curvature of the band, and Δ is the detuning from the band edge. $K_0(x)$ scales as $\log(1/x)$ for $x \ll 1$, so by varying the detuning from the band edge, the length scale over which the spin interaction is mediated can be controlled via Δ. While the band-edge frequency and curvature are not easily controlled in situ, it is possible to adopt a Λ scheme to relax the requirements of the band-edge frequency[23].

2.4.5 Mode Profiles

The mode profiles of the guided waveguide modes of the hexagonal structure at the high symmetry points are shown in fig. 2.18 and fig. 2.19 for the TE and TM fields, respectively. The reason that both C and F_p are much higher at the upper band edge than the lower is that the mode profile of the upper band edge has a strong maximum in the center of the hole, thereby coupling stronger to an emitter located there.

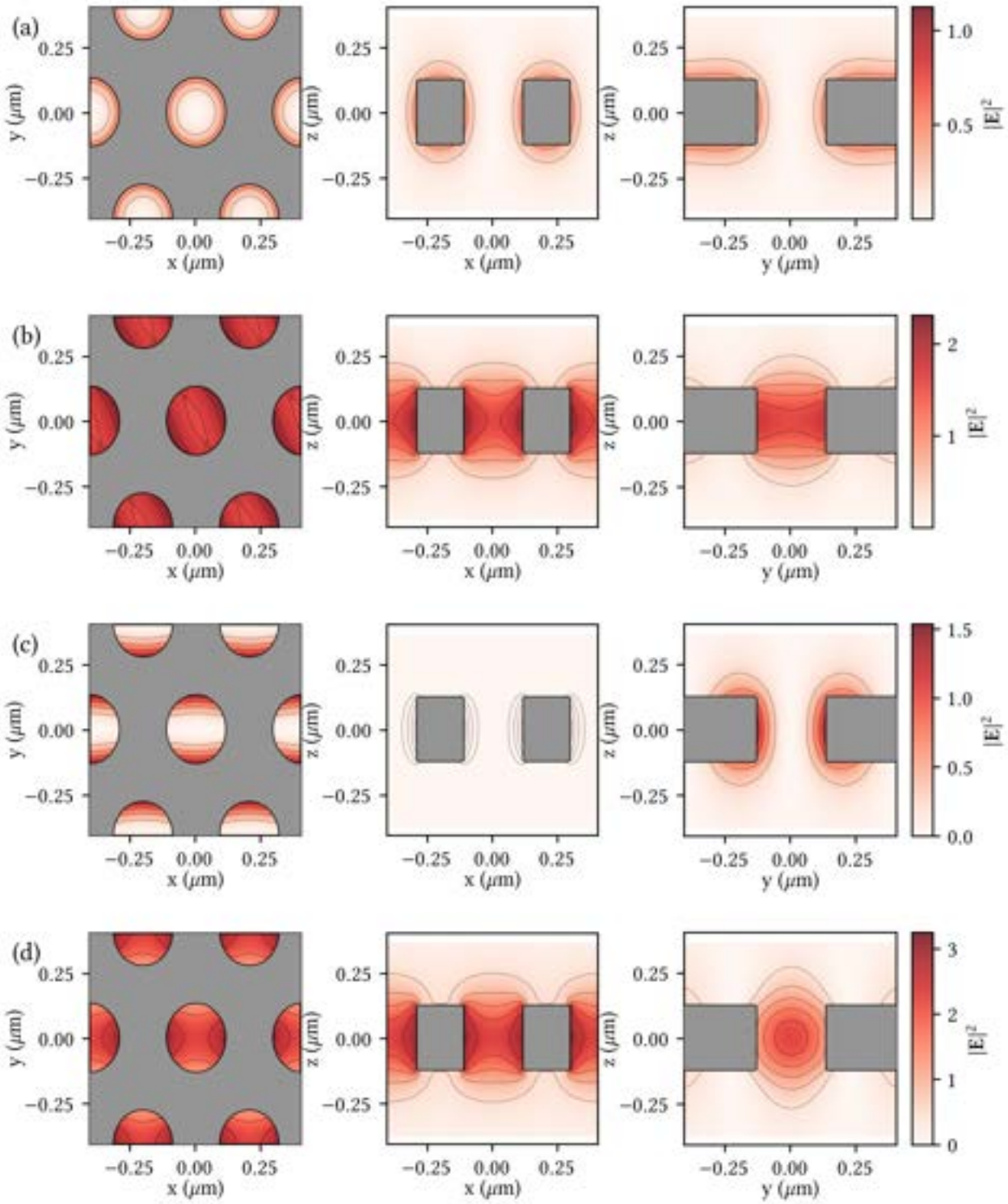

Figure 2.18: The mode profiles of the TE-like modes in the hexagonal PhC at high symmetry points. (a) The dielectric band at the $\mathbf{k} = K$ point. (b) The air-band at the $\mathbf{k} = K$ point. (c) The dielectric band at the $\mathbf{k} = M$ point. (d) The air band at the $\mathbf{k} = M$ point.

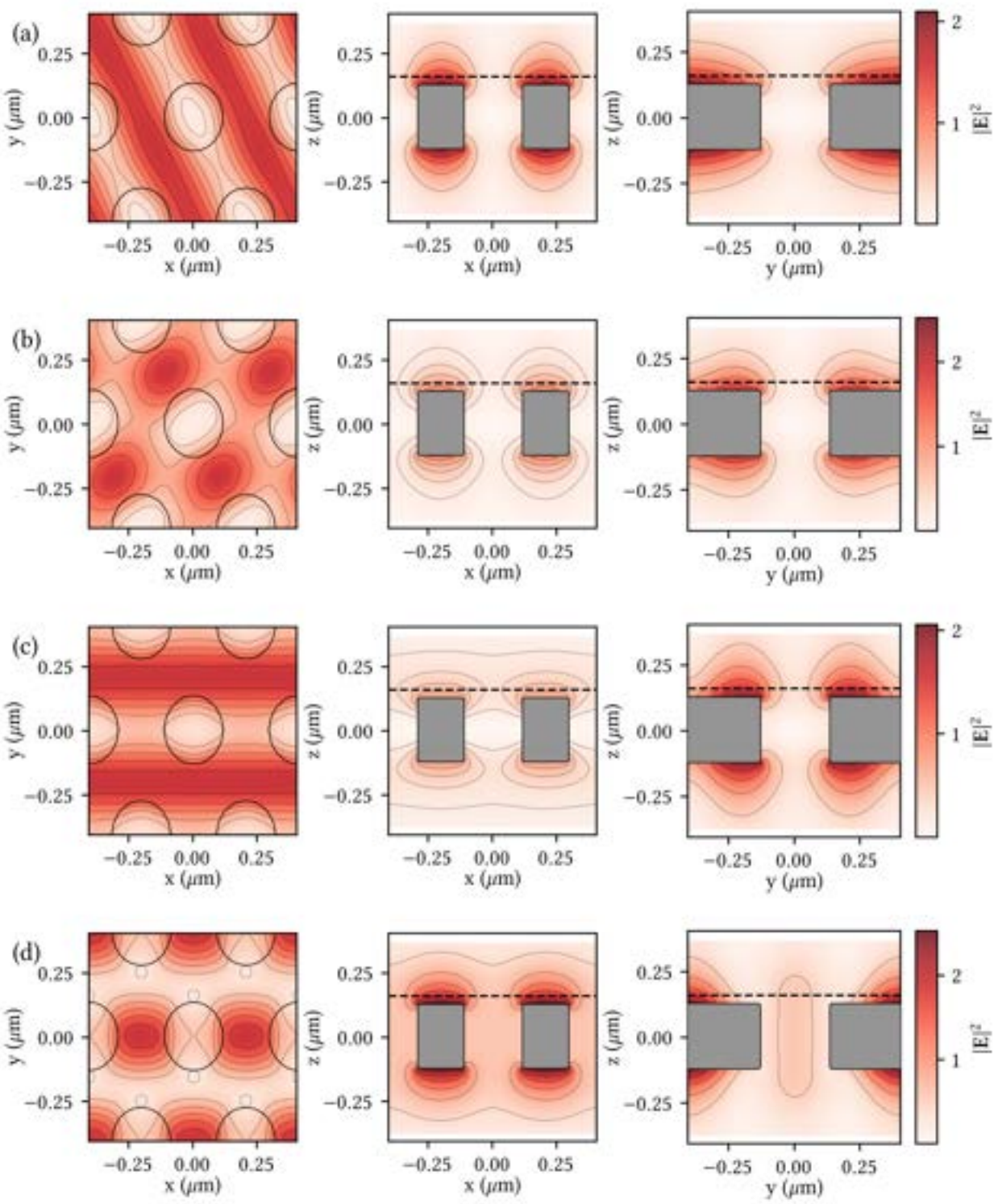

Figure 2.19: The mode profiles of the TM-like modes in the hexagonal PhC at high symmetry point. The plot of $\mathbf{E}(x, y)$ is in a plane just above the dielectric at a height z indicated by the dashed lines in the two other columns. This is done because there is little to no field at $z = 0$ for any of the modes. (a) The dielectric band at the $\mathbf{k} = K$ point. (b) The air-band at the $\mathbf{k} = K$ point. (c) The dielectric band at the $\mathbf{k} = M$ point. (d) The air band at the $\mathbf{k} = M$ point.

Trapping Considerations

Trapping the atoms at the surface of the waveguide is still one of the main challenges of the experiment. While it is outside the scope of this thesis, we will briefly discuss it in the context of the guided modes.

The trapping potential for a two-level atom in an optical tweezer is given by [53]

$$U_{\text{dip}}(\mathbf{r}) = \frac{3\pi c^2}{2\omega_0^3}\frac{\Gamma}{\Delta}I(\mathbf{r}), \tag{2.4.8}$$

where Δ is the detuning from the atomic transition, and $I(\mathbf{r})$ is the light intensity of the light at the atom position. For red-detuned light, $\Delta < 0$, the resulting force is attractive, and for blue-detuned light, $\Delta > 0$, it is repulsive.

In addition to the dipole force from the light, one must also consider the Casimir-Polder force, an attractive force that decays rapidly with the distance from the surface of the dielectric. The CP potential can be calculated from the polarizability of the atom, and the Green's tensor[54], and must be included when dealing with nanoscopic potentials.

We can make general observations by looking at the mode profiles in fig. 2.18 and fig. 2.19. A red detuned trap would require a maximum to be formed away from the surface of the crystal, preferably in the center of the hole. This is the case for the air-band TE mode at the M point. The cooperativity and Purcell enhancement decay rapidly with the detuning from the band edge, so it is desirable to have the upper band edge aligned with the D2 line. Consequently, a red-detuned trapping scheme using only the TE mode at the M point is not feasible.

To form a stable blue-trap from the guided modes, a 3D minimum of the intensity must be formed in the center of the hole. This is not the case for any TE modes, but the TM modes may prove helpful, as they can create a repulsive potential to counteract the attractive CP potential.

In nano-fiber experiments, stable potentials are formed by a combination of red- and blue-detuned guided modes[30]. For the 2D PhC, the most promising approach relies on a combination of guided modes, side-illumination, and CP forces [52] to form a trapping potential with a minimum at the center of the air holes in the PhC, see fig. 2.20.

A possible way forward is to form super-cells, where defects are periodically introduced to the nominal crystal structure to form strong concentrations of light in the air modes at the defect site[33, chapter 7]. The defects may be designed by casting it as an inverse problem where the dielectric structure is optimized for minimal trapping volume using gradient-based methods [55].

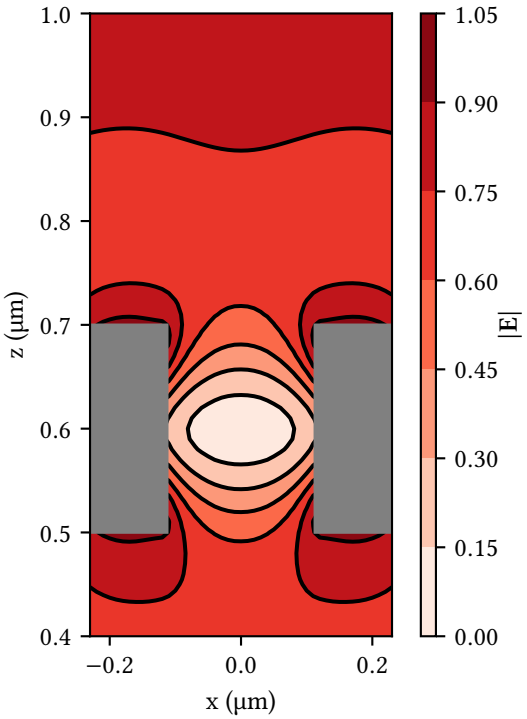

Figure 2.20: Trapping potential from side illumination. A plane wave is incident from the top and forms an intensity minimum at the center of the hole.

2.4.6 Tolerances

Fine control over the placement of the band edge is required for the schemes described above. Thermal fine-tuning of the band edge in suspended Si_3N_4 devices has been demonstrated [27], but there are still strict requirements for the fabrication. To determine how the band frequencies scale with the different design parameters, we vary the thickness, hole radius, and lattice constant of the PhC around the nominal design values. For the square lattice, the goal is to align the D2 line with the slow-light section at the X point, so we calculate how the dielectric band frequency at the X point changes with the design parameters.

The goal of the hexagonal design is to align the D2 line with the upper band edge, so we track how the air-band mode frequency changes at the M point.

The results are shown in table 2.5.

Of particular interest is how the band edge frequency can be tuned after the lithography step. There are two approaches to doing so: atomic layer deposition (ALD) and isotropic etching with buffered hydrofluoric acid (BHF). In ALD, a layer of Al_2O_3 can be isotropically deposited on the structure with sub-nanometer precision. From ellip-

Parameter (THz/nm)	$\Delta f/\Delta d$	$\Delta f/\Delta r$	$\Delta f/\Delta a$	ALD	BHF
Square X	-0.27	0.96	-1.38	-0.99	0.69
Hexagonal M	-0.21	1.19	-1.12	-0.97	0.98

Table 2.5: The tuning rates for the lower (upper) band frequencies at the X (M) for the square (hexagonal) design.

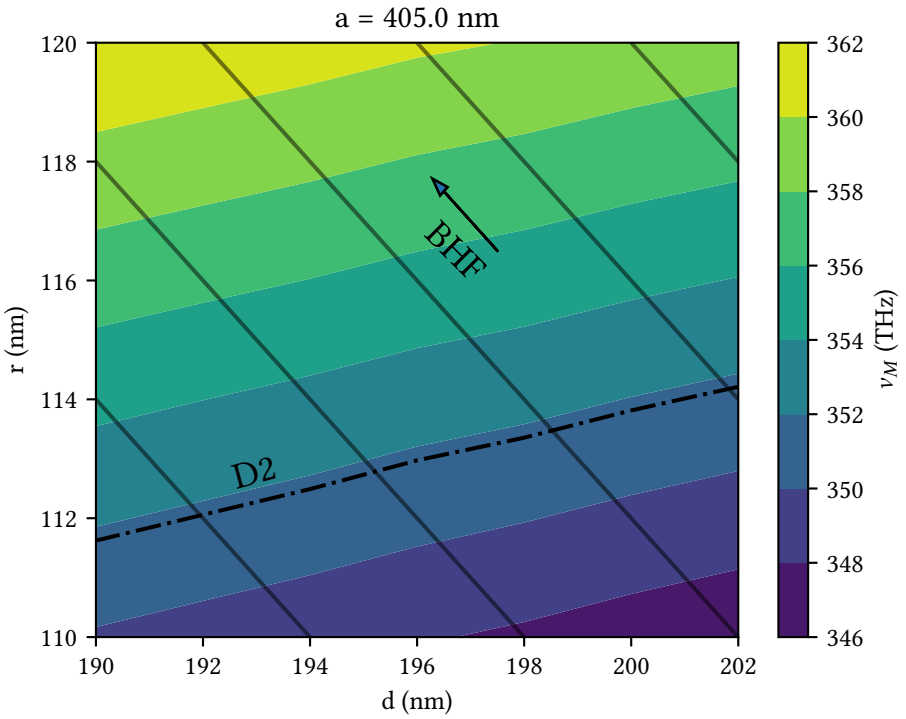

Figure 2.21: Simulated values of the upper band-edge frequency for hexagonal design for thickness variations d and r. The dash-dotted line indicates the D2 line, and the solid lines and the arrow indicate the contours along which the band-edge frequency can be changed using an isotropic etch.

someter measurements, we find that the Al_2O_3 layer has a refractive index of $n = 1.67$ at 852 nm. The simulations show that the band edge frequency increases when adding Al_2O_3.

In BHF, stoichiometric Si_3N_4 has very low etch rates of ≈ 1 nm/min, allowing us to increase the radius and decrease the thickness of the slab at the same rate. In fig. 2.21, we see that changing the radius and thickness by the same amount increases the band-edge frequency.

Chapter 3

Fabrication

This chapter presents the details of the fabrication endeavors. The time and effort dedicated to developing this fabrication process constitutes a large part of the thesis work, and we will try to provide a detailed explanation of the process to serve as a reference for future work. The starting point for our fabrication endeavors was inspired by the work in the group of Jeff Kimble, particularly the processes described in PhD theses by Andrew Mcclung [38], Su-Peng Yu [33]. The final process we ended up with is similar. However, there are a few notable differences, the most notable change being the shift to a Cr hardmask instead of the ZEP520a resist mask, and as a result of this, the dry-etch is also different. The reason for this change was challenges with the aspect ratio of the design, and we will elaborate on this in section 3.5. The primary cleanroom facilities used at DTU Nanolab are generally well-equipped for working with wafers rather than chips. This, combined with the fact that the existing fabrication expertise in our group was entirely on wafer-scale processing, led us to develop a process optimized for wafer-scale fabrication. A wafer-scale fabrication process has the added benefit of allowing us to fabricate multiple devices in parallel, but it ultimately led to a few dead ends.

To the work presented below into context, we showcase two structures that were fabricated as a part of this project.

3.0.1 Atom Delivery Playground Chip

The atomic experiment requested a device with holes of varying sizes to benchmark atom transport through progressively smaller apertures. The device is shown in fig. 3.1. A 2x2 mm window is opened at the center of the chip, where a 200 nm thick Si_3N_4 membrane is suspended over the window. The membrane has a 1x1 mm rounded square in the center to allow the atoms to move freely through the plane of the structure. At two corners of the chip are rows of holes with varying diameters. There are 10 holes per row, and 14 rows with diameters varying from 10 µm to 600 nm. We chose to add a

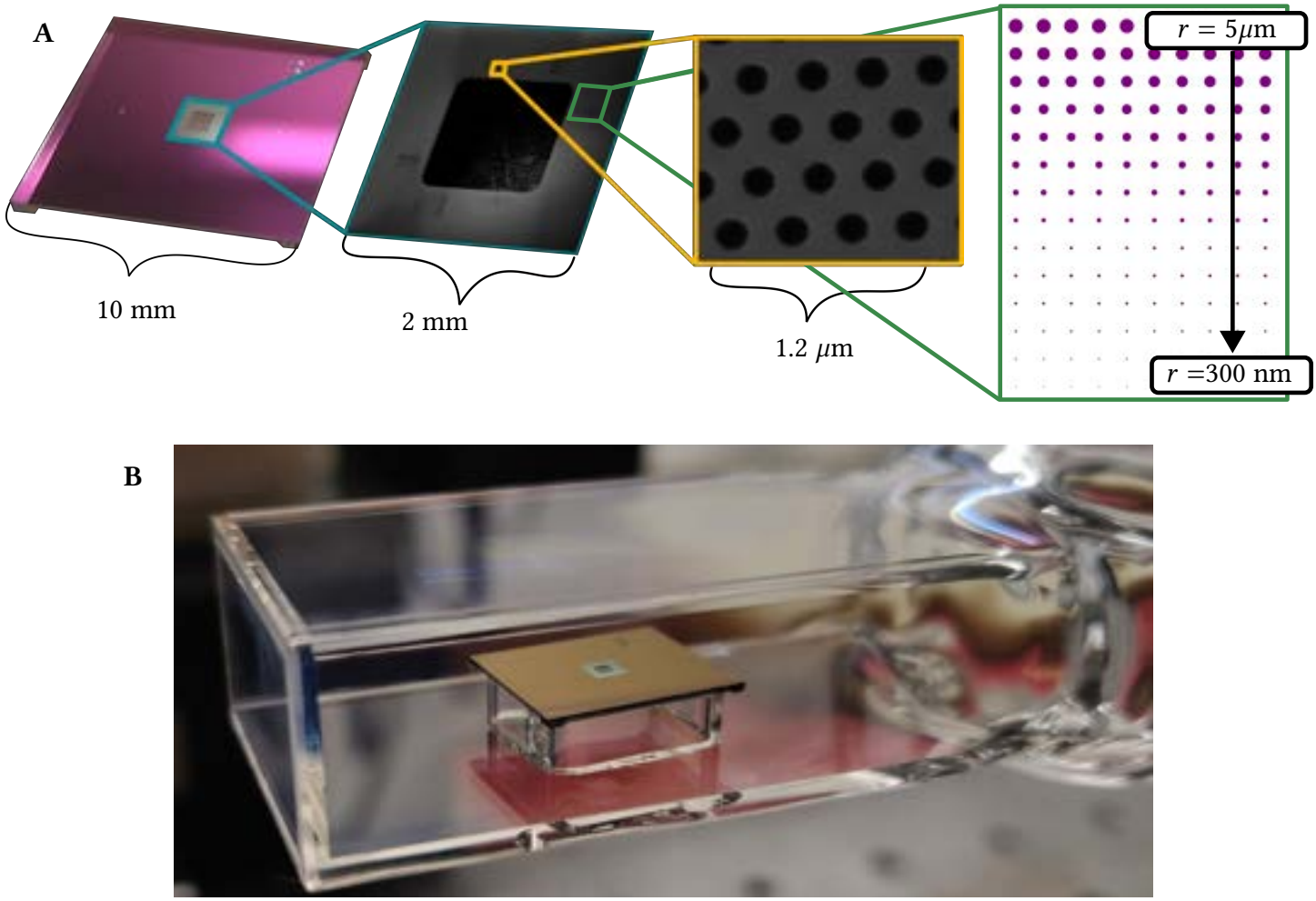

Figure 3.1: Atom delivery test chip. **A** From left to right: Photograph of chip. SEM Micrograph of the center of released membrane section of the chip. SEM Micrograph on the photonic crystals at the edge of the chip. Holes of varying sizes for atom delivery testing, diagram. **B** The chip is mounted in a glass cell on a glass pedestal using silicate bonding [32].

few photonic crystal sections at the edge of the structure. One of these chips has been mounted in a glass cell, and will soon be integrated with the atomic arrays fig. 3.1**B**

3.0.2 DBR Mirror Cavity Devices

The final waveguide devices that were fabricated as part of this project were waveguides with DBR mirror cavities of varying lengths, shown in fig. 3.2, designed to measure the propagation loss of the waveguide. The design of these cavities is described in section 2.3, and the transmission measurements are presented in section 4.2.1.

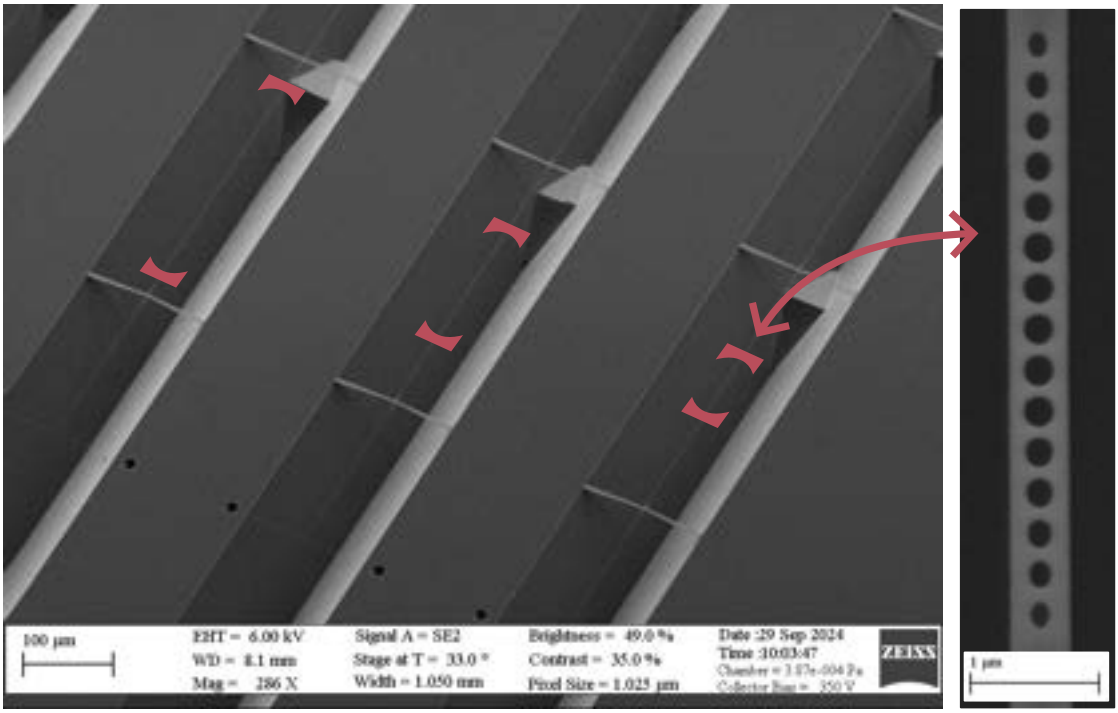

Figure 3.2: SEM micrograph of waveguides with DBR mirror cavities. The cavities are located on an untethered section of the waveguide, with the mirror positions varied between devices, as indicated by the red mirror symbols here. On the right is an SEM micrograph of a DBR mirror.

3.1 Process Overview

The fabrication process is shown in fig. 3.3. Stochiometric Si_3N_4 is deposited on a Si wafer using Low Pressure Chemical Vapor Deposition (LPCVD). Marks aligned to the wafer-flat are added with UV-Lithography, and one side is then coated with a layer of Cr using electron beam evaporation. The Cr layer is coated with CSAR 62 resist, which is patterned using electron beam lithography (EBL). The pattern is developed and the Cr layer is etched using a dry etch process with a Cl chemistry, followed by another dry etch process with a CF_4/O_2 chemistry to etch the Si_3N_4 layer. UV Lithography is done on both the front and the backside of the wafer to add cleaving grooves, and the wafer is cleaned in piranha before being placed in a solution of Potassium Hydroxide (KOH) to anisotropically etch the Si layer and release the device. Finally, the wafer is cleaned in piranha again before being cleaved into individual chips. The following sections will detail the individual process steps, the challenges faced in their development, and suggestions for future work.

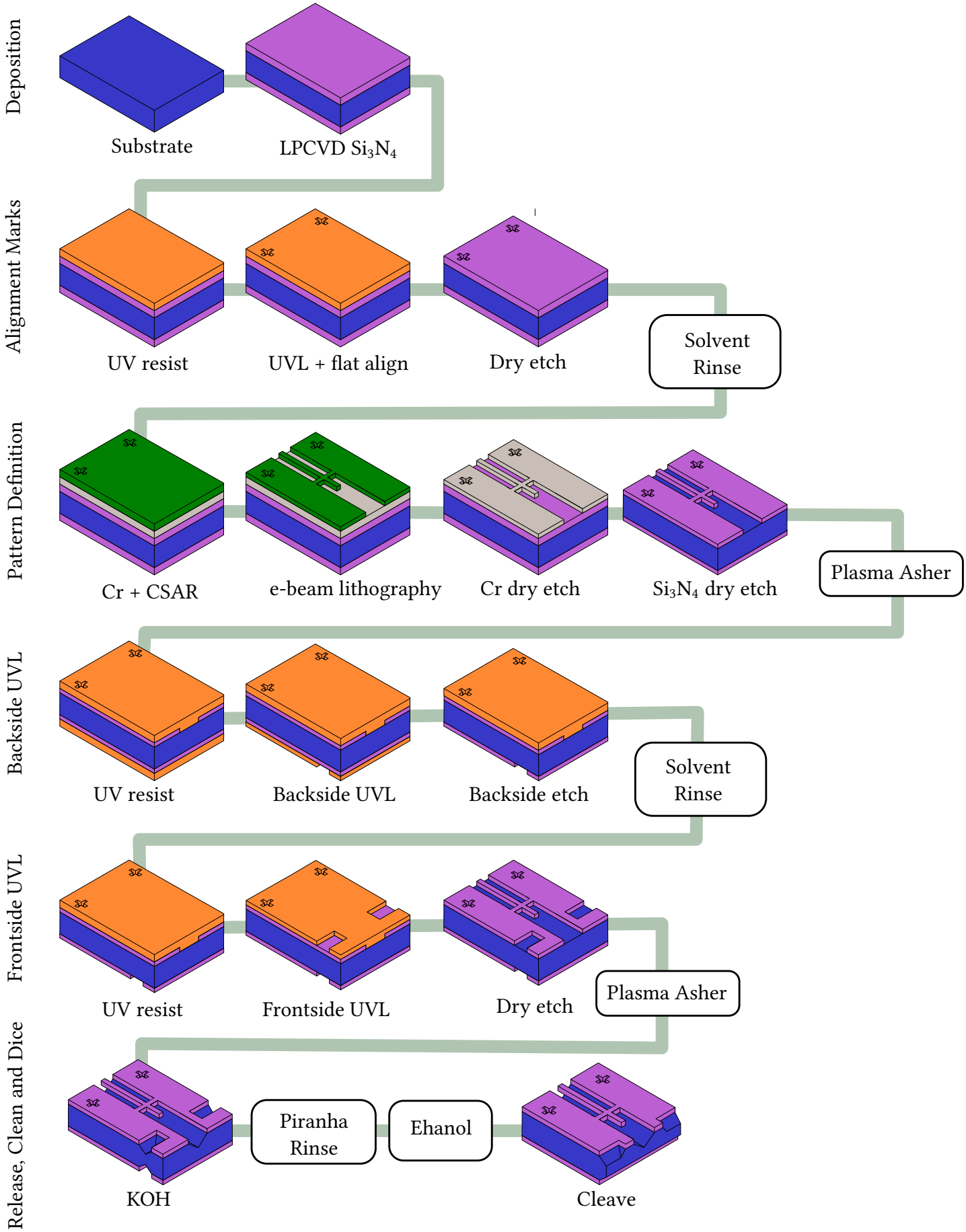

Figure 3.3: Overview of the fabrication flow.

3.2 Deposition

The first step in the fabrication process is the deposition of a layer of stoichiometric Si_3N_4 on a Si wafer. The Si wafers used are $(500 \pm 15)\,\mu m$ thick with a diameter of 100 mm. They are double side polished, and the are cut along the <100> direction. There was a choice between 500 µm and 300 µm, and we found that working with the slightly thicker substrates made handling the chips easier.

Stochiometric Si_3N_4 was chosen for this device for a couple of reasons. It has low optical losses of Si_3N_4 at NIR wavelengths [56], and it has a high enough refractive index $n = 2$ at 852 nm to open a partial bandgap in a slab PhC. The large transparency window[57] provides flexibility in exploring different atomic transitions and far-off-resonant trapping schemes without worrying about material absorption. The high tensile stress of the Si_3N_4 layer is also beneficial for suspended devices, as it keeps the membrane flat after release. The high stress also results in mechanical frequencies of the suspended devices that can be engineered to be much faster than the trapping frequencies in the dipole traps, which helps limit the parasitic heating of the atoms in the traps.

The deposition is done using a LPCVD furnace where the wafers are placed in a quartz tube and heated to a temperature of 800 °C at a pressure of 0.5 mbar. The gases used are SiH4 and NH3, and the deposition rates are typically around 3 nm/min. The maximum thickness allowed in the furnace is 200 nm, as the high tensile stress of the Si_3N_4 causes the wafer to crack for thicker films. There are methods for achieving thicker layers of Si_3N_4 [58], but we limit ourselves to a thickness of 200 nm. This not only simplifies the deposition step, but as we shall discuss later in this chapter, features with an aspect ratio (depth/height of a hole) are challenging to fabricate.

The Si_3N_4 layer is optically characterized after fabrication using an ellipsometer. For a batch of 12 wafers, typically 3 wafers are characterized, and if the results are similar this is taken as representative of the batch. The ellipsometry provides the thickness of the Si_3N_4 as well as the refractive index at multiple points across the wafer. Typically variations in Si_3N_4 thickness is around 5 nm across the wafer, and a refractive index of (1.99 ± 0.01) is measured at 852 nm.

The stress in the Si_3N_4 film is measured with a stylus profiler. A reference measurement of the wafer is taken after Si_3N_4 deposition, the Si_3N_4 is then removed from one side in a dry etch, and the wafer is measured again, and the stress-induced deformation is used to calculate the stress in the Si_3N_4 film. The stress is typically around 1 GPa to 1.5 GPa of tensile stress. Some initial measurements seem to suggest that annealing the Si_3N_4 film at 1150 °C for 4 h can reduce the stress in the film, at the cost of a slight increase in thickness. This is still under investigation, and the results are not yet conclusive.

3.3 Wafer Flat Alignment and UV Lithography

The anisotropic etch of Si in KOH is highly dependent on the crystal orientation of the Si wafer, this mechanism and the way that it is utilized for our design will be discussed in section 3.6, but it is important to note that the design must be aligned to the crystal orientation of the wafer. This is done by aligning the design to the wafer flat, which is a small flat edge on the wafer that is aligned to the crystal orientation. The wafer flat is cleaved along the <1,1,0> direction, and experience from the cleanroom is that the alignment between the wafer-flat and the <1,1,0> plane is accurate within a few mrad, and we content ourselves with aligning to the wafer flat in the maskless UV aligner (MLA). This could be verified using the approach described in [59], where the KOH anisotropy is used to identify the crystal planes.

3.4 Electron Beam Lithography, a Tale of Two Cities

Electron Beam Lithography (EBL) required the most substantial time investment during the fabrication process. This was partly due to the complexity of the tool and also because a decision was made to transition to a different EBL system mid-project.

The first system used is the JEOL9500 at DTU Nanolab which is a 100 kV system. This system is built for a production facility with a high throughput, and as such it is not the most user-friendly system. Exposures are controlled through jobdeck and schedule files that are compiled locally on the EBL computer, and the samples have to be loaded into the machine by the cleanroom staff. The system is very reliable, but due to high demand in the earlier half of this project exposures often had to be scheduled weeks in advance making it difficult to iterate on designs.

The decision was made to move our E-beam endeavors to the Elionix F-125, which is a 125 kV system located at KU. This system is targeted towards academic users, with a more user-friendly interface at the cost of lower throughput. The main disadvantage of this system is that it is not located at the same facility as the rest of the equipment used in this fabrication process. In fact, it is not even located in a clean room, which also caused some concerns regarding sample contamination.

Transporting samples between the two facilities, which are located 10 km apart, presents logistical challenges and potential risks for contamination.

A notable consequence of switching EBL systems was the difference in calibration settings between the two systems. This meant that the exposure parameters that had been optimized for the JEOL system were not directly transferable to the Elionix system. This was not a major problem, but it did mean that some time had to be spent on re-optimizing the dosing and the proximity effect correction for the new system.

After working with the Elionix F-125 for around a year, the booking system on the JEOL9500 was changed to favor academic users, and the system became much more

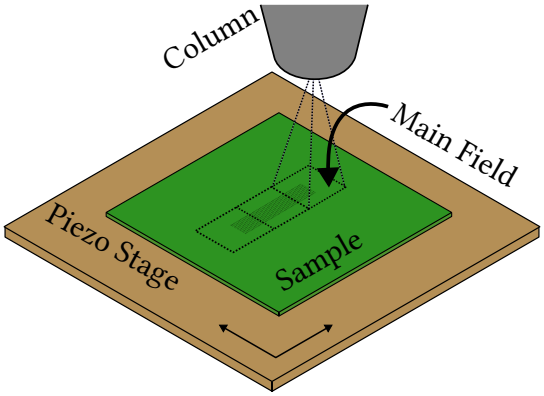

Figure 3.4: Schematic of the EBL exposure process. Inside the write field the beam is scanned using only the deflection coils. Patterns that are larger than the main field are exposed by moving the sample with the piezo stage.

readily available. At the same time, the Elionix system was experiencing technical difficulties and was unavailable for some time. This led to a switch back to the JEOL system for the final part of the project.

3.4.1 Dosing and Proximity Effect Correction

The basic operation of the EBL is illustrated in fig. 3.4. Inside what is called the write, the beam can be deflected using the deflection coils in the column. For the JEOL system the maximal write field is 1000 µm × 1000 µm, and in the Elionix it is 500 µm × 500 µm. Inside this write field, the beam position can be scanned on a discretized grid defined by the pitch p of the scanner, and the dose D per unit area is given by

$$D = \frac{I \cdot t_s}{p^2}, \tag{3.4.1}$$

where I is the current of the electron beam, t_s is the dwell time. It is typically listed in $\mu C/cm^2$.

The bandwidth of the scanner limits the minimal dwell time, and thus, for a given dose, smaller currents allow for smaller pitch and higher resolution but will, in turn, affect the total write time. For a pattern of total area A, the total write time is

$$T = \frac{DA}{I}, \tag{3.4.2}$$

and a compromise between resolution and write time must be made.

One of the first things to figure out is the dose to clear D_c, which is the dose required for a given resist to be completely removed in the development process. This depends on the resist type, the material stack and the electron beam acceleration voltage. To

determine this dose, a dose test is performed where a square pattern is exposed with varying doses, and the dose to clear is determined by the dose where the center of the square is completely developed fig. 3.5. The square should be large enough that the proximity error effects do not affect the center of the square, which leads us to a discussion of the effect of proximity error.

When the electron beam interacts with the resist and the substrate, secondary electrons are generated. These secondary electrons can then interact with the resist and cause it to be exposed even if the primary electron beam is not directly hitting the resist. This effect is called the proximity effect, and it can lead to a distortion of the pattern, as exemplified in fig. 3.5. Here all of the square receives nominally the same dose, but the proximity effect causes the center of the square to receive a larger dose than the edges.

If the nominal dose pattern is $D(x, y)$, the actual exposed pattern $E(x, y)$ will be the convolution of the PSF of the electron beam and substrate stack with the dose pattern. This can be expressed as

$$E(x, y) = (D * \mathrm{PSF})(x, y) = \int\int \mathrm{d}u\mathrm{d}v D(u, v)\mathrm{PSF}(x - u, y - v). \tag{3.4.3}$$

The effects of this proximity error on the developed pattern can be mitigated by applying a proximity effect correction (PEC) to the design. This is done by solving the inverse problem of finding the dose pattern $D'(x, y)$ that, for a given PSF, reproduces the nominal dosing pattern, i.e., the pattern that, when convolved with the PSF, gives the nominal dose pattern. This can be expressed as

$$E(x, y) = D(x, y) = (D' * \mathrm{PSF})(x, y). \tag{3.4.4}$$

The effect of the PEC is, more practically speaking, to decrease the dose in densely exposed areas and increase the dose in sparsely exposed areas. Commercial software for calculating and applying the PEC is available. We use Beamer on both the Elionix and the JEOL systems. This requires a model for the PSF of the electron beam and material stack, which can be simulated using software such as Tracer.

The dose to clear is a good starting point for the dose to use for the exposure, but given the complexities of PEC, it is always wise to conduct a dosetest for a specific pattern. If in doubt it is often advisable to go with a slightly higher dose than the dose to clear, as overdevelopment will typically only cause a slight increase in the feature size, while underdevelopment can lead to a complete loss of the feature.

3.4.2 Fracturing

After PEC, the dosing pattern is fractured into smaller polygons that the EBL system can handle. The Beamer software does this, allowing users to choose between different

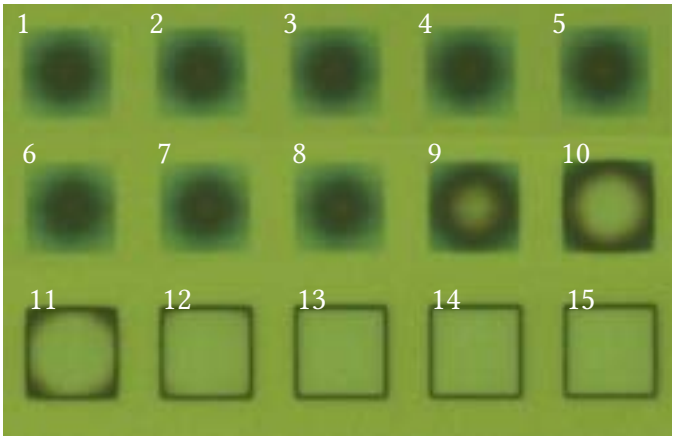

Figure 3.5: Optical micrograph of dose to clear test for the Elionix System. A 100 µm x 100 µm square is exposed with a dose varying from 100 µC/cm^2 to 275 µC/cm^2 in steps of 12 µC/cm^2. The dose to clear is taken to be the dose where the center of the square is completely developed. The dose to clear is estimated to be approximately 225 µC/cm^2 corresponding to image 11.

fracturing modes. The 'conventional' mode fractures the design into smaller polygons, while the 'curved' mode tries to follow the edges of the design. A sketch of the two modes can be seen in fig. 3.6. The choice of fracturing mode can have a significant impact on the distribution of shots, which in turn can affect the fidelity of the produced pattern. When the .gds files are written, it is important to check that the number of polygons is not too high, as this will cause the fracturing to produce a large number of small polygons that the EBL system cannot handle as seen in fig. 3.6a-b.

3.4.3 Double Pass Exposure and Traversal Pathing

When exposing waveguide sections that are too large to fit within the main field of the E-beam writer, stitching errors can occur at the boundaries. It has been shown that by dividing the dose between multiple overlapping write fields, the optical propagation losses can be reduced significantly [60].

We choose to adopt a double-pass exposure strategy, but in principle, the dose can be divided between a larger number of passes. We have not yet verified that the double-pass exposure affects the optical properties of our devices, so a systematic study of this should be conducted, but from SEM imaging, we have observed a decrease in stitching errors.

When exposing multiple chips on a wafer in a single exposure, it is important to consider the traversal path of the E-beam, as incorrect pathing can result in neighboring areas of the design being exposed at a large enough difference in time for thermal drift to cause misalignment. This becomes even more apparent when doing multiple passes. As seen in fig. 3.7, if the write path is not optimized, the two halves of the dose

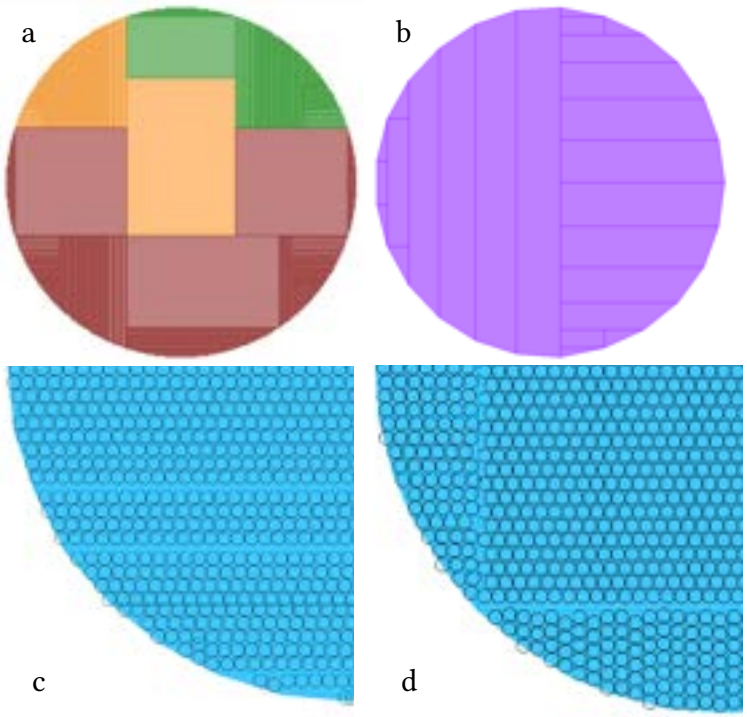

Figure 3.6: Fracturing of a design. The design is divided into smaller write fields, and the exposure is done field by field. **(a)** The design is made with too high resolution, which causes the fracturing to create a large number of small polygons that the EBL system cannot handle. **(b)** The design is made with a lower resolution, which causes the fracturing to create a smaller number of larger polygons that the EBL system can handle. **(c)** and **(d)** The fractured circle overlaid with e-beam shots. In **(c)** the 'conventional' fracturing mode is used, and in **(d)** the 'curved' is used where we see a more uniform distribution around the edges of the circle.

can be applied in non-consecutive write fields, which, combined with thermal drift, can cause the exposed features to be distorted. This can be controlled with options in the software used to fracture the design which in our case is Beamer[1]. It is also important to consider the size of the write fields. The default double-pass configuration of Beamer is to displace the field by half of the main field size in both x and y, and looking at fig. 3.7, it can be seen that the default write-field size of 1 mm × 1 mm results in some waveguides being split between two write fields. To prevent this, the width of the write field should match an integer number of waveguides, and the offset should only be along the direction of the waveguide. With this optimization, we saw great improvement in the quality of the exposed waveguides.

[1]From GenISys GmbH

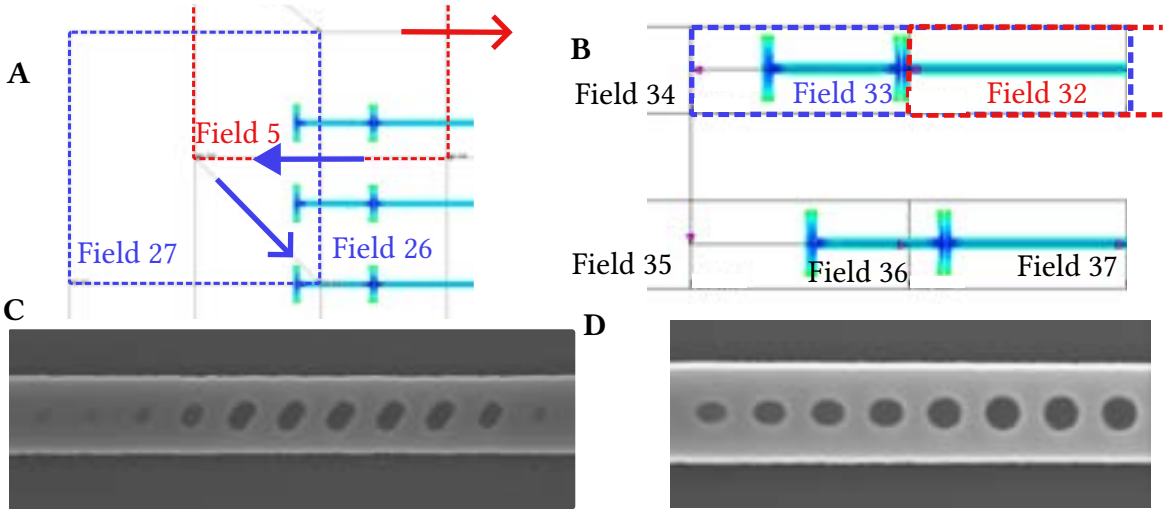

Figure 3.7: The effects of traversal pathing. **A** The write field size and double-pass offset have not been adapted to the waveguide width, and we see that the traversal path causes the two half-doses to be delivered at a delay of 22 write-fields. **B** The writefield has been decreased in width to match that of a waveguide, and the double-pass offset has been limited to the X direction. The two double-pass dose is now delivered in subsequent writefields. **C** (**D**) SEM micrograph of a device defined with the travelsal path of **A** (**B**).

3.4.4 Exposure with Multiple Currents

To decrease exposure times, we implemented a double-current exposure where only areas close to the waveguide are exposed with a small current I_{sleeve} = 2 nA, and areas around the waveguide such as the waveguide area is exposed using a current of I_{bulk} = 29 nA. The low current area is called the sleeve, and the high current area is called the bulk as shown in fig. 3.8. The size of the sleeve is set to 10 µm to prevent any proximity effects, but could perhaps be reduced to increase write-speeds even further. The overlap is set to 2 µm. When doing PEC for the two currents, we found that using 'optimal contrast' for the fine and 'optimal clearing' setting in PEC->advanced for the bulk gave the most consistent results.

To increase write speed even further, the bulk area is not exposed fully, but instead the larger area is exposed in tiles as illlustrated in fig. 3.8. When released in the KOH, the squares are underetched and float away. In the defining script, the number of tiles across the width of the waveguide and the linewidth of the exposed area is defined, and the size of the tiles is calculated to match these. We found that for the 150 µm wide V-groove, 6 tiles and 2 µm lines worked well.

One caveat is that this type of release is not ideal when released in a wetbench where other users reuse the KOH, as Si_3N_4 squares are sometimes left floating in the bath. Moving forward, this should perhaps be reconsidered. For free-space coupled

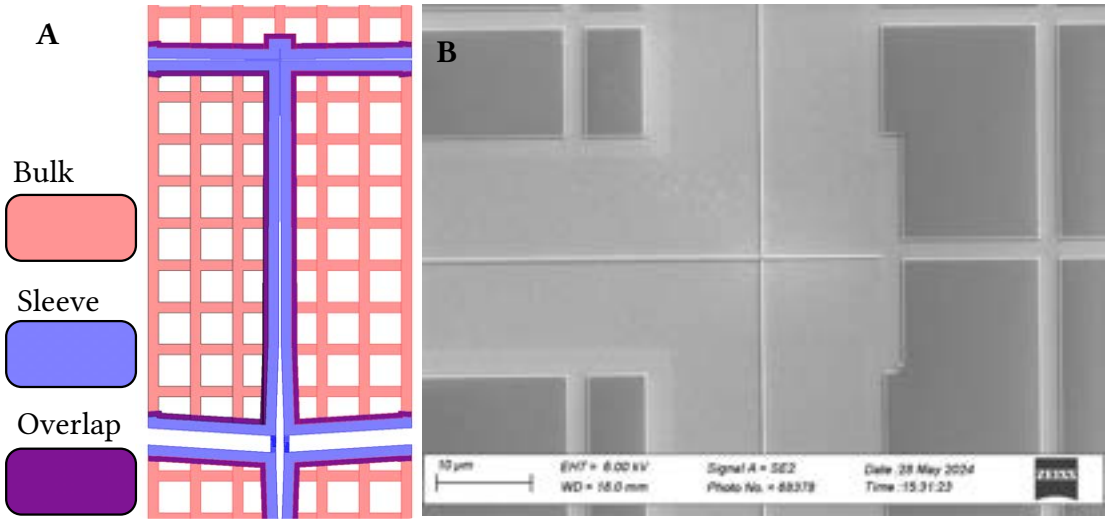

Figure 3.8: Double current exposure with tiling. **A** The bulk area is exposed at $i_{\text{bulk}} = 29\text{nA}$, and the sleeve is exposed at $i_{\text{sleeve}} = 2$ nA. The two have an overlapping area to ensure full exposure. **B** SEM micrograph showing the resulting structure.

devices, the V-grooves can be made much narrower which will make the need for tiling less urgent.

3.4.5 Thermal Stability

When exposing patterns with multiple currents, thermal expansion of the stage can lead to misalignment of the patterns exposed with different currents. This can be mitigated by using a thermally stable material for the casette such as Titanium, but for the latter part of this project the only casette available at the EBL was made of aluminum. This led to a significant amount of misalignment in the patterns, which can be seen in fig. 3.9. The thermal drift causes a shift between the pattern exposed at 2 nA and 29 nA that displaces the waveguide from the center of the V-Groove. This is a significant problem as the waveguide is designed to be centered in the V-Groove to ensure that the fiber is correctly aligned.

This issue primarily arises during extended exposure durations. Therefore, one potential mitigation strategy is to reduce the number of devices exposed in a single run. An alternative approach to mitigate this issue would be to realign to the alignment marks at each chip, rather than only at the start of the exposure. However, this would increase the total write time. A balanced approach could involve aligning after every fourth or sixth chip to optimize both accuracy and efficiency.

Due to time constraints, the temporary solution was to load the cassette well in advance of the exposure, preferably the night before, to allow it to thermally stabilize.

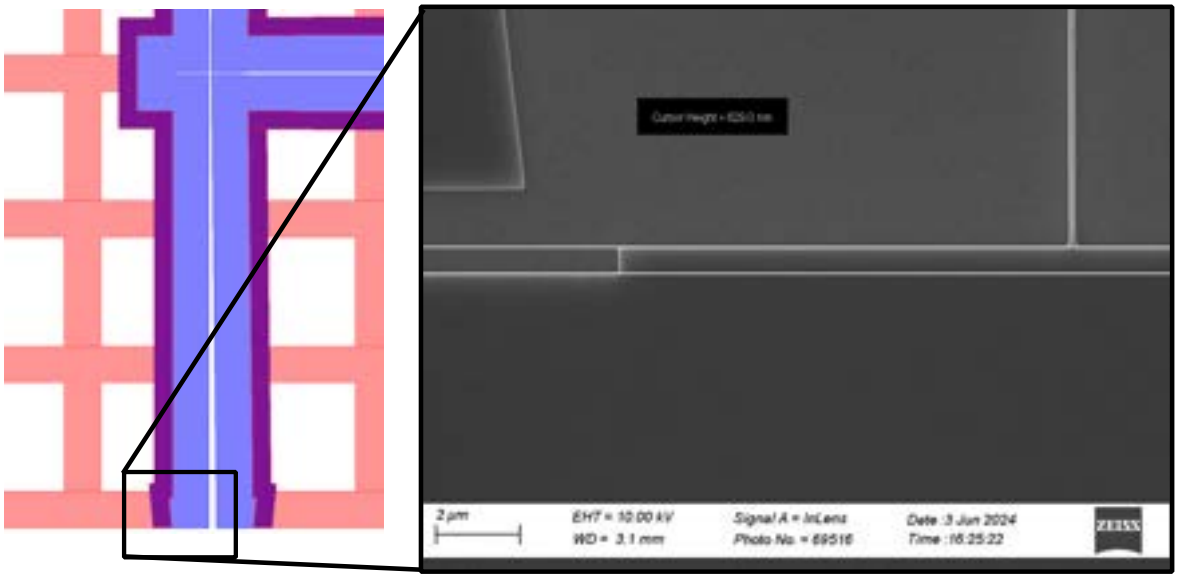

Figure 3.9: The effect of thermal drift when exposing with two currents. On the left is the nominal design. On the right we see that the sleeve is shifted upward from the bulk by ≈630 nm as indicated by the horizontal white lines. This is caused by a thermal expansion of the casette holding the wafer during the exposure, and the time delay between the bulk and sleeve exposure.

This reduced the misalignment between the V-groove and the waveguide from 1 µm to <100 nm, which has minimal impact on the coupling fig. 2.7.

3.5 Pattern Transfer

To transfer the pattern defined by lithography into the Si_3N_4 we use reactive ion etching (RIE) in an inductively coupled plasma (ICP). In these machines a plasma is formed via a high power RF field produced by a set of coils around the chamber. The ions are accelerated towards the sample via a DC bias field on the platen (the surface holding the sample). By balancing the isotropic chemical etching of the ions interacting with the surface, with the physical etching of the ions ballistically etching away the surface, the etched side walls in the pattern transfer can be made close to vertical.

Typically plasma etching of Si_3N_4 is done using a Flourine chemistry, with either CF_4, CHF_3, and SF_6. As there was no existing knowledge readily available on etching Si_3N_4 photonic waveguides in our research group or with our collaborators at the DTU cleanroom facilities, we consulted our colleague Eric Langman who had previously been working on optomechanical Si_3N_4 devices at UCSB, and he recommended a process utilizing an etching recipe using a CF_4/O_2 chemistry and a Chromium (Cr) hardmask.

Adapting any recipe to a new cleanroom is time-consuming, and we focused our attention on optimizing this etching recipe. One unfortunate circumstance is that the use of Cr hardmask necessitated the use of two tools in the DTU cleanroom which are in extremely high demand, the e-beam evaporator and an ICP for etching metals. Other etching recipes, such as the one presented in [33][38] that rely on a resist soft-mask could be worth investigating, but the hard mask offers some advantages over these.

In our design, an additional challenge is when etching some of our smaller features such as the $\approx$ 200 nm holes into a 200 nm Si_3N_4 film, we encounter aspect ratio dependant etching effects (ARD), where features with high aspect ratios (depth/width) experience reduced etch rates, and this often leads to small features having more sloped sidewalls. Hard masks offer larger selectivities allowing for longer etch times, which can mitigate the effect of ARD.

3.5.1 Choice of Electron Beam Resist

Practical considerations primarily drove the selection of CSAR resist; it was readily available in the cleanroom's industrial-grade spin-coater, whereas ZEP resist required separate procurement and manual spin-coating. A small quantity of ZEP resist was acquired and tested, but the results were sufficiently similar to the CSAR resist that we decided to stick with the more convenient option. The emphasis on convenience was not a matter of complacency but rather of achieving consistent results. Although manual spin-coating of ZEP resist can be performed with the same precision as automated spin-coating of CSAR, minimizing potential sources of human error is generally preferable.

One thing to note when using the spin coater for CSAR is that one should always assume that the resist-line in the tool is clogged. This is because the resist is quite viscous and can easily clog the line, and thus one should always verify this, and clean the tip of the dispenser with anisol if necessary. It is always possible to verify the presence of resist on the wafer by looking for fringes in the reflection at the flat of the wafer. If these are present, it has been coated.

3.5.2 Chromium Hard Mask and Dry Etch

The Cr hardmask is deposited using an electron beam evaporator[2]. The mask thickness is 30 nm deposited at a rate of 1 nm/s. It has been shown that for Al, higher deposition rates result in large grains and higher surface roughness [61], and we assume a similar behavior for Cr. The deposition rate is kept low, but a systematic study of this effect could be conducted.

[2]Temescal/Ferrotec at DTU Nanolab

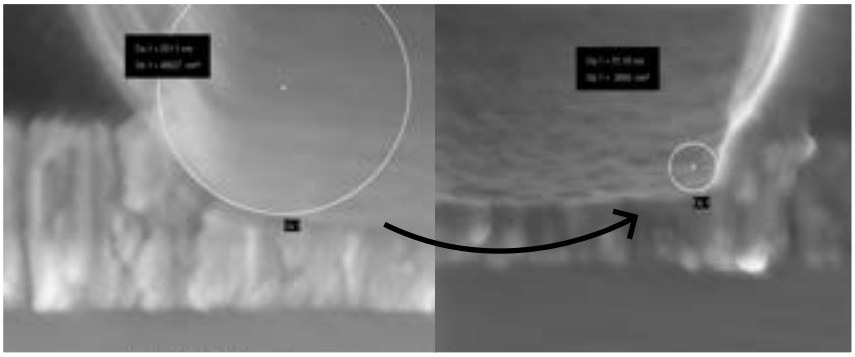

Figure 3.10: The radius of fillets formed at the edge of the Cr mask was reduced by lowering the pressure.

To transfer the pattern from resist to Cr, we adopted a Cl_2/O_2 dry etch recipe which has previously been shown to produce good results both in terms of sidewall roughness but also sidewall slope [62][63]. The etch was optimized by looking at the cross-section of etched gratings with varying pitches and filling factors, which were cleaved and imaged with SEM. In the images, we identified that the Cr hardmask formed fillets at the edge of the mask, fig. 3.10. This was found to be correlated with increased edge roughness in the subsequent Si_3N_4 etch, and we optimized the parameters to reduce the radius of these fillets. The optimization of this etch was based around a design-of-experiment parameter sweep of the parameters listed in table 3.1 using a Plackett-Burman type distribution. For more details on this analysis, see the publicly available technical note [64]. The parameter range was chosen to be in a reasonable range around the process described in [63].

The recipe was developed on an ICP Metal etch from SPTS, and all etching was done on 6" carrier wafers coated with 1 µm PECVD SiO_2, which has been observed to increase process stability [63]. We experimented with crystal bonding the devices to the carrier, but found it to have limited influence on the results.

The parameters used at the end of the project are shown in table 3.2.

Table 3.1: Design-of-Experiment Parameter Sweep for Cr Dry Etch

Parameter	Range
Coil power	300-500 W
RF power	15-25 W
Total gas flow	40-80 sccm
Oxygen percentage	15-25 %
Pressure	5-15 mTorr

Table 3.2: Parameters for Cr Dry Etch

Parameter	Value
Gas flow rate (Cl_2)	23 sccm
Gas flow rate (O_2)	7 sccm
RF power	15 W
Pressure	10 mTorr
Etch rate (Cr)	43 nm/min
Platen temperature	20 °C
Selectivity Cr:CSAR	0.42

Table 3.3: Parameters for Si_3N_4 Etch

Parameter	Value
Gas flow rate (He)	174 sccm
Gas flow rate (CF_4)	40 sccm
Gas flow rate (O_2)	4 sccm
Coil power	1300 W
Platen power	350 W
Pressure	4 mTorr
Etch rate (Si_3N_4)	420 nm/min
Platen temperature	5 °C
Selectivity Cr:CSAR	Not defined

3.5.3 Si_3N_4 Dry Etch

The Si_3N_4 etch parameters are shown in table 3.3. One interesting thing we found was that a layer of CrF_4 forms during the etch, and the hardmask actually grows thicker during the etch. This makes the selectivity ill-defined, but we found that a 20 nm Cr film can withstand approximately 50 s of etching. This layer of CrF_4 is very resilient, and the only reliable way of removing it that we have found is in an oxygen plasma. This recipe has not been optimized for optical performance, but as demonstrated in fig. 3.11, we see that we can achieve great sidewall verticality even for high aspect ratios. To assess the quality of the etching, we made designs with the parameters of our target designs for both 2D arrays of holes to mimic the PhC, 1D arrays of narrow ridges to mimic the tether arrays, and isolated ridges of varying widths to mimic the nominal waveguide and the coupling tethers. These were extended over a few mm and cleaved after etching for inspection in SEM.

3.6 Membrane Release with KOH

To release the Si_3N_4 membrane from the Si substrate, we use Potassium Hydroxide (KOH) as it etches Si anisotropically. The rate of etching along the <1,1,1> crystal plane in KOH is, depending on temperature and concentration, typically between 50-400 times lower than along the <100> plane, and 100-600 times lower than along the <110> plane. The effect of this, is that a rectangular opening in the Si_3N_4 will etch a pyramid into the Si, with the sidewall angle $\theta = \tan^{-1}\sqrt{2}) = 54.7^{\circ}$, with the sides of the crystal following the <1,1,0> planes. A side view of the etched profile is shown in fig. 3.12, where we see that the nonzero etch rate along <1,1,1> causes the Si to be

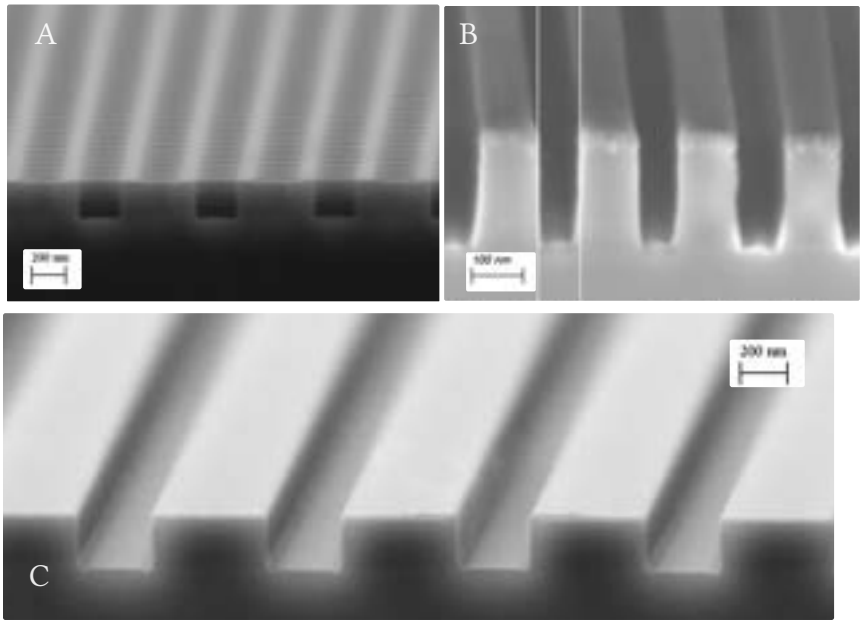

Figure 3.11: SEM Micrographs of structures used for testing the performance of our etching. The material stack is Si/Si_3N_4 /Cr. In A, we see that we can etch holes with a radius of $\approx$ 100 nanometers with minimal sidewall tilt. In B, we see that even very narrow trenches can be etched with reasonable verticality, and note that there is an appreciable amount of Cr left on top, which indicates that by overetching even further, the sidewall could be improved further. In C, we see excellent sidewall verticality for less densely spaced ridges.

etched underneath the Si_3N_4 by an amount δ given by

$$\delta = S_{111} T \sqrt{6}, \tag{3.6.1}$$

with T being the etch time. The etch rate of Si_3N_4 in KOH is generally found to be immeasurably small, meaning that it can safely be submerged in KOH without worrying about changing critical structures. For many purposes, the under-etch δ can be ignored. The relationship between the depth of the etched pyramid D and the width of the opening in the mask w is given by $D = w/\sqrt{2}$. As we shall discuss shortly, δ should be considered when alignment is critical.

As shown in fig. 3.12**C**, positive corners are underetched much faster and, the design tries to avoid these by using only negative corners. In fig. 3.12**D** a negative square has been defined at an angle to the <110> plane, and the under-etched pyramid has conformed to the crystal axis. These effects become critical when trying to open a window through a device that has V-grooves, as we shall discuss in the next section.

The KOH etching is done in a wet-bench where a 40% w.t. solution of KOH undergoes weekly quality control by the cleanroom staff. The etch rates along <100> are taken from the log-book for the machine, and the etch rate along <111> is estimated

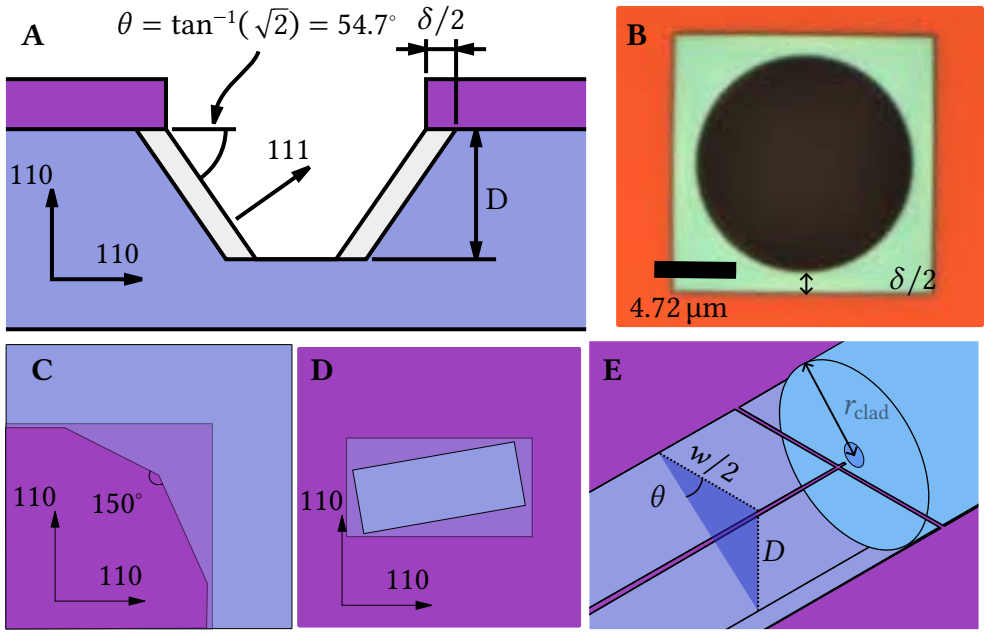

Figure 3.12: **A** The different etch rates along the <1,0,0> and <1,1,1> crystal planes causes anistropic etching at an angle θ. The figure is adapted from [65]. **B** Microscope image of a hole in Si_3N_4 etched into a Si substrate. The hole is etched into a square with the sides aligned with the <1,1,0> plane, and the under-etch δ can be estimated from the width of the square. **C** Positive corners are underetched more than negative corners. Blue indicates Si, translucent purple indicated the areas where the nitride mask has been under-etched. **D** If a square is misaligned with respect to the <110> plane, the under-etched pyramid will conform to the crystal axis. **D** Illustration of aligning an optical fiber with a waveguide suspended across the V-groove.

from the hole in fig. 3.12**B**. A circular hole in the Si_3N_4 etches into a square with the sides aligned with the <110> plane, and the etch rate S_{111} can then be estimated from the under-etch with eq. (3.6.1). The bath is preheated to 80 °C for about an hour before etching.

3.6.1 Capillary Forces and Ethanol Drying

Mechanical failure after release is a real concern, and while one might intuitively expect the crux to be the surface tension when pulling the sample out of a liquid, it was found that this was not the most perilous step. The most critical step was the drying of the sample. When the sample is taken out of the final rinse, water sticks to the surface, and surface tension causes the water to pool up around the waveguides in the V-grooves, and as the water evaporates, these puddles contract, pulling on the waveguide tethers, causing them to first bend and then snap. This can be observed in

real-time in a microscope, making for a rather heart-wrenching experience as this is one of the final steps in the fabrication process.

To mitigate this, the sample is moved directly from the final water rinse into a beaker with ethanol. The ethanol displaces the water, and as the surface tension of ethanol is less than a third of that of water[66], the capillary forces are greatly reduced. We found that simply taking the wafer out of the ethanol bath after a few minutes and letting it dry in air was sufficient to substantially increase the yield. This has only been tested for waveguides suspended over a V-groove and not waveguides suspended over a fully etched hole, and it is possible that this may be insufficient for the latter. We have successfully released membrane devices suspended over a window, so it is likely that this method is sufficient for suspended waveguide devices as well. Should this prove not to be the case, one can pursue an approach similar to that of Yu[33], where the device is moved from liquid to liquid in a specially made cup such that the device never breaks the surface of the liquid, and the final drying is done in a critical point dryer.

Table 3.4: Parameters for KOH Etching

Parameter	Value	Source
S_{111}	$(12.5 \pm 2.5)\,\mathrm{nm/min}$	Measured
S_{100}	$(1.30 \pm 0.05)\,\mu\mathrm{m/min}$	Measured
r_{clad}	$(62.5 \pm 0.5)\,\mu\mathrm{m}$	Datasheet
KOH Temperature	80 °C	Measured
KOH Concentration	40% w.t.	Measured

3.6.2 Fiber V-groove Dimensions

To align the core of a stripped HP780 fiber with the waveguide as shown in fig. 3.12**E**, we must define the width of the opening in the Si_3N_4 such that the etched V-groove has the correct depth. As we saw in section 2.2.3, the coupling to the waveguide is sensitive to the transverse displacement of the fiber, and as we shall see, the nonzero S_{111} etch rate should be taken into account when designing the V-groove.

The HP780 fiber has a cladding diameter of $2r_{\mathrm{clad}} = (125 \pm 1)\,\mu\mathrm{m}$, and with a bit of trigonometry we find that to center the core of the fiber on a waveguide of thickness d =200 nm the depth of the V-groove trench should be

$$D = r_{\mathrm{clad}}/\cos(\theta) - d/2 = 108.2 \pm 0.9\mu\mathrm{m}. \tag{3.6.2}$$

This gives an etch time $T = D/S_{100} = 83 \pm 3$ minutes using the parameters shown in table 3.4. In this time, the Si_3N_4 mask has been under-etched by $\delta = S_{111}T\sqrt{6} =$

$(3.6 \pm 0.7)\,\mu m$, which displaces the waveguide by $\Delta z = \delta/\sqrt{2} = (1.8 \pm 0.4)\,\mu m$. This displacement decreases the coupling into the TE mode by $\approx$ 30%, which is not negligible. To prevent this displacement, the width of the opening in the mask should be adjusted to include the effect of the underetch

$$w = \sqrt{2}D - \delta = (150 \pm 1)\,\mu m. \tag{3.6.3}$$

Precise alignment of the structure with the <110> crystal plane is also crucial. As indicated in fig. 3.12 **D**, a rectangular shape that is not aligned with the <110> crystal planes will underetch into a square along the crystal planes. Because the V-grooves extend over several mm, even a small misalignment from the crystal plane results in sufficient under-etching to displace the waveguide too far from the waveguide to couple light in. As stated above, we found that the wafer-flat alignment of the MLA was sufficient to prevent excessive underetching.

3.6.3 Etching a Through-Window

Etching all the way through a 500 µm wafer takes about 6.2 hours. The depth of the V-grooves is ≈110 µm which takes about 80 minutes to etch so to avoid excessive amounts of underetching of the waveguide, we place the wafer in a backside protector[3] isolating the front of the wafer from the KOH. After etching ≈350 nm of Si into the back of the wafer, it is taken out, rinsed, and placed in a regular wafer caddy and put back into the KOH bath to etch the remaining 150 µm of Si. When placed in the regular caddy it is advised to place the device wafer between two wafers with Si_3N_4 on both sides to limit liquid flow through the opened window. When the structure is fully released, the caddy is *carefully* taken out of the KOH bath, and placed into a preheated water rinse. After rinsing, the wafer is moved to a Piranha solution of 4:1 sulfuric acid to hydrogen peroxide, where it is cleaned for 10 minutes, after which it is rinsed a final time. The wafers are kept vertical throughout this procedure to minimize surface forces out of the plane of the wafer.

Full through windows were successfully etched for membrane devices such as the one shown in fig. 3.1, but work on suspending waveguides across the opening is still ongoing. Suspending waveguides across a window is challenging both because the structures are very thin and fragile, but also because it requires precise timing of the KOH etch to avoid excessive underetching at the corners where the V-groove opens onto the window. In fig. 3.13 a full window has been opened under a set of waveguides, tethered to rails as described in section 2.2.2, and we see severe underetching of the Si_3N_4 in the regions next to the rails. Minimizing this requires both precise alignment to the crystal planes of the substrate, and timing the KOH etching.

[3] Which here protects the front of the wafer, yes.

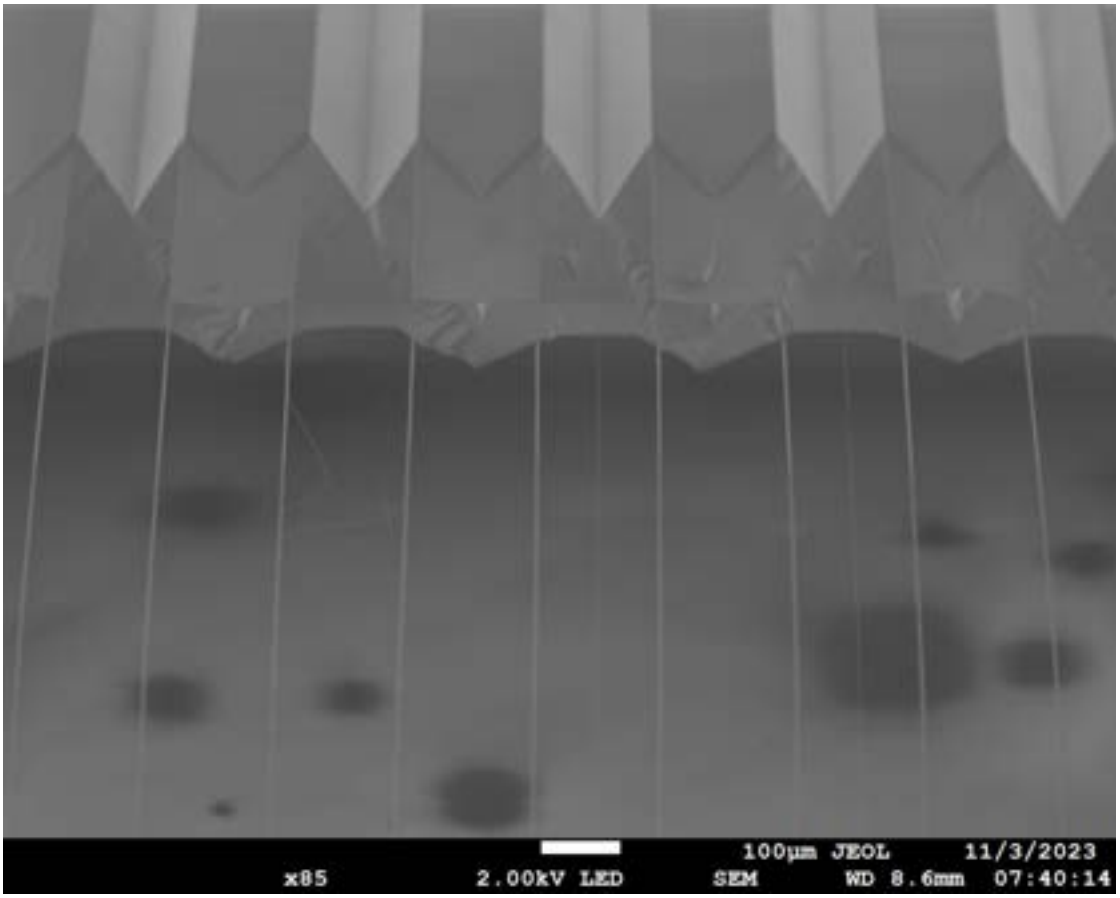

Figure 3.13: A window has been etched under a set of suspended waveguides. At the top of the image we see severe underetching of the Si_3N_4 structure.

3.6.4 Tethers

Initially, we used tethers that extended all the way to the edge of the V-groove, but we found that these were prone to bunching up, and we suspect that this might lead to the tethers being more prone to breaking, so we wanted to change the tether design to be more robust. From FDTD simulations, we found that beyond the first µm, the optical effects of the tether array were negligible, and we thus decided on a design where only the last 1 µm of the tether is perforated, and the rest is solid. To ensure that the tether is under-etched in the KOH, elliptical holes were added to the tethers. The final design is shown in fig. 3.14, and we found this tether design to be reliable throughout multiple fabrication runs.

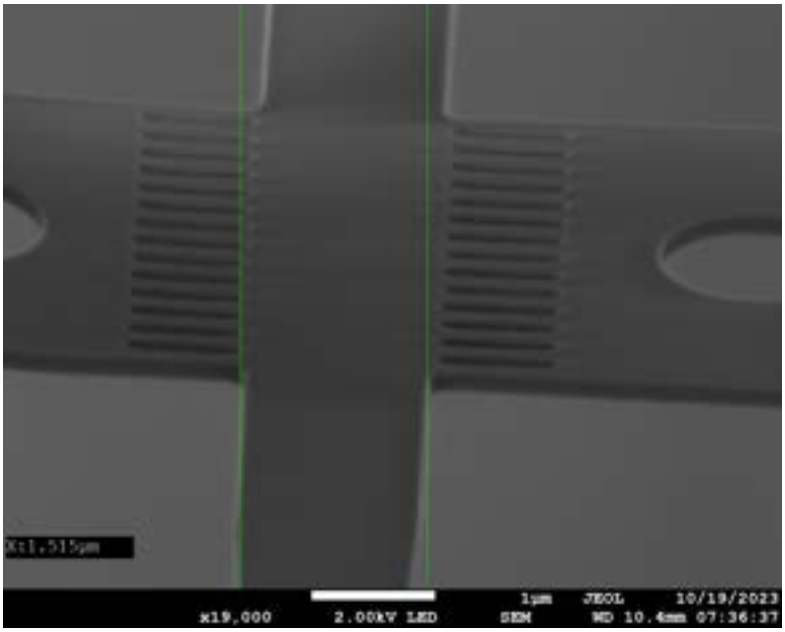

Figure 3.14: The final tether design. The tethers are solid for the first 1 μm and then perforated with elliptical holes.

3.6.5 Cleaves

The final step is to cleave the wafers into chips. By etching V-grooves into the front and the back of the wafer along the <110> directions, the wafer can be made to snap in the correct place. Avoiding debree when cleaving is a real concern, and the best approach that we have found is to hold the device vertically, and snapping it as illustrated in fig. 3.15**A**.

As discussed in section 2.2.3, being able to cleave the chips very close to the end of the waveguide can be a limiting factor in designing free-space coupled devices. Using V-grooves on the front side perpendicular to the V-grooves housing the waveguides is problematic, as it will underetch the corners as shown in fig. 3.12**C**, creating large 'flaps' of Si_3N_4 that may or may not break off during release and cleave. To avoid this, we etch V-grooves on the backside of the wafer, and add a cleave line on the front side that terminates just before the V-groove, as shown in fig. 3.16. The groove on the backside is 300 μm deep, and the groove on the front is 70 μm deep. With this method we found that we could reliably cleave the waveguide .

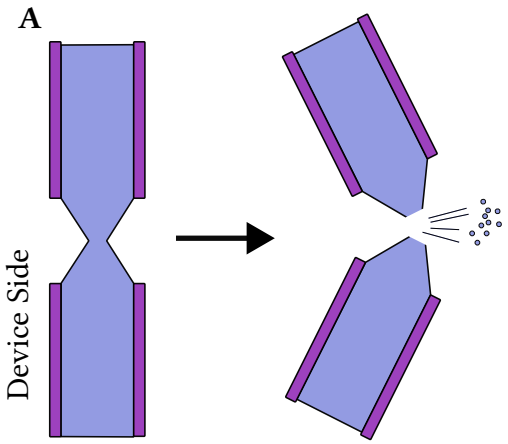

Figure 3.15: Illustration of the approach used to cleave the chips. The wafer has V-grooves etched on either side along the <110> crystal axis, and the wafer is snapped by hand while being held vertically to prevent the Si debris from landing on the device side.

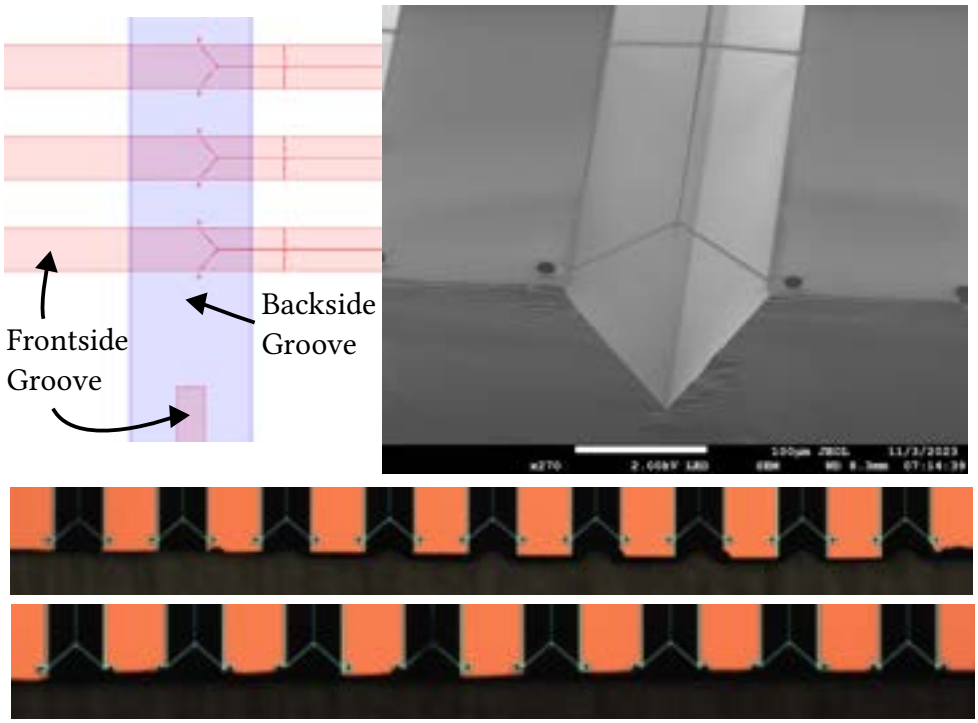

Figure 3.16: We cleave the wafers close to the edge of the waveguide by creating a V-groove on the backside of the wafer, the center of which has been aligned with the desired cleave line. Cleave lines are added to the front, but do not cross the V-grooves. To the right is a SEM micrograph showing a cleaved coupler. The waveguide here is a 'mock' device that has been exposed using UV lithography for testing the cleave method. On the bottom, two microscope images of a large number of waveguides cleaved very close to the edge of the chip, showing the robustness of this method.

Chapter 4

Characterization

This chapter reports on the status of our fabrication capabilities and provides an overview and description of the characterization techniques we applied or attempted to apply. Results from fabricated devices will illustrate the methods. Some techniques mentioned in this section did not reach a point where we used to characterize the devices, so they are included here to document the progress made in utilizing the tool.

4.1 Scanning Electron Microscopy

Scanning Electron Microscopy (SEM) focuses a beam of electrons onto a sample and measures the scattered electrons from the sample surface. The electron beam is focused and redirected with a series of magnetic lenses, i.e., coils, and the image is formed by correlating the intensity of the scattered electrons with the scan position of the beam. The highest achievable resolution depends on the material of the subject as well as the skill of the operator, as dialing in the parameters of the image can be difficult and time-consuming. Conductive samples are generally much easier to image, as there is no charge build-up on the sample's surface. Charge on the surface creates a repulsive force on the electron beam, distorting the image. Insulating samples can be imaged by coating them with a thin layer of conductive material, but this can be difficult to do without damaging the sample, and the conductive layer can sometimes obscure the features of interest. For a conductive sample, resolutions of 2 nm are possible, but the resolution is lower with dielectric materials.

Imaging samples at different stages throughout the fabrication process results in qualitatively different images, and the measured dimensions depend on both the material, which is imaged, and, as we shall discuss in the next section, the imaging parameters.

As the SEM is located inside the cleanroom, measurements can be done between process steps and non-destructively so as long as there is no E-Beam resist on the sam-

ple. The images are used primarily as a qualitative tool to inspect whether the previous process step was successful. Still, we also put effort into extracting quantitative data such as feature sizes, sidewall angles, and roughness from SEM images. This project used two different SEM systems, one located in the DTU cleanroom [1] and one at the KU facilities[2]. The performance of the two is similar, but as most of the time was spent with the DTU SEM, this is also the system where the most consistent quality SEM images were measured, and this is the one used for the quantitative feature extraction described in the following section.

Quantitative Feature Extraction

The work on the 2D PhC structures was primarily carried out at the beginning of this project when we had yet to design and fabricate waveguides. Transmission spectroscopy was, therefore, not an option for the fabricated 2D PhCs, so their characterization was done exclusively using SEM imaging. In particular, we wanted to quantify the distribution of radius, pitch, and roundness in an automated fashion. After imaging the PhC, the SEM images are imported into Python, and the contours are detected by first applying a Gaussian Blur to the image and then determining the threshold value using Otsu's Binarization [67]. From the binary image, the contours are detected using the algorithm [68], implemented in the OpenCV library [69]. The center of mass of the images is determined from the image moments, and the effective radius of all contours is calculated as

$$r = \sqrt{\frac{A}{\pi}}, \tag{4.1.1}$$

where A is the area of the contour. Many of the detected contours are not related to the photonic crystals, and the contours are filtered by their radius as well as their circularity as defined by the parameter

$$\eta = \frac{4\pi A}{s^2}, \tag{4.1.2}$$

where s is the arclength of the contour. For a perfect circle, $\eta = 1$, and for any other shape $0 \leq \eta \leq 1$. The contours are filtered by η to remove any non-circular shapes.

The pitch is calculated by the pairwise distance between the contours' center of mass (COM). For a hexagonal geometry, these pairwise distances will be grouped around

$$d_{mn} = a\sqrt{m^2 + mn + n^2}, \tag{4.1.3}$$

where a is the pitch and m, and n are integers representing the position of the contours on a hexagonal lattice. As the distance increases, these distances become increasingly

[1] Zeiss Supra 40VP
[2] JEOL 7800F prime

densely spaced, so we limit ourselves to the five smallest distances to avoid confusing clusters. The pitch is then determined by grouping the distances using K-means clustering, as implemented in the Scikit-learn library[70], and dividing the measured distance by the corresponding value of d_{mn}/a. This approach allows us to extract feature sizes from the SEM images automatically.

But this begs the question of how sensitive our feature extraction is to changes in the SEM parameters. To determine this, we used a sample of holes with a nominal radius of $r = 200\,\text{nm}$ and nominal pitch $a = 600\,\text{nm}$. The samples are fabricated following the process described in the previous chapter but terminated before releasing the Si_3N_4 from the Si. The material stack is thus Si_3N_4 on a background of Si.

The sample was imaged with the SEM at different magnifications and scan speeds using two secondary electron detectors, the SE2, and the Inlens detector. The SE2 detector is located on the side of the beam column. It is generally good at detecting topological features, while the Inlens detector is situated in the beam column and has better detection efficiency. An array image is taken for each setting, and the features are extracted as described above. The results are shown in fig. 4.1. From the figure, we see that for the SE2 detector, the measured radius strongly depends on the zoom level but is less sensitive to the scan speed. The Inlens detector is slightly less sensitive to the magnification level when using intermediate scan speeds but generally more sensitive to the scan speed. The increased measured radius for high magnification levels and slow scan speeds is explained by the thermal drift of the SEM stage, as the image acquisition time is long enough to be severely distorted. This effect also contributes to the decrease in η as the circles become elliptical.

This analysis assumes that the radii and pitches are normally distributed, which may not be the case, as there is likely to be a spatial dependence on the measured features. In fig. 4.2, we see that there is indeed a spatial distribution of radii in the images and that this distribution depends on the detector used. For the Inlens detector, there is a gradient in the detected radii, which coincides with the gradient in the image, and towards the top of the image, the gradient causes the contour detection to fail. This gradient is present in many images taken with the Inlens detector. Thus, if one intends to use the Inlens detector for feature extraction, it is important to be aware of this effect and mitigate it during imaging. For the SE2 detector, the radii are more randomly distributed, with a clear island of smaller radii towards the center of the image where the structure has been repeatedly imaged. This island is likely an artifact caused by charge build-up on the surface from repeated imaging of the same area.

To determine whether the increase in measured radius as a function of the magnification level for the SE2 detector seen in fig. 4.2 is caused by a non-uniform spatial distribution of the radii, the same analysis was done on specific subsets of the detected circles for different magnification levels, and the general trend of increasing radius with magnification level was found to be consistent across the image.

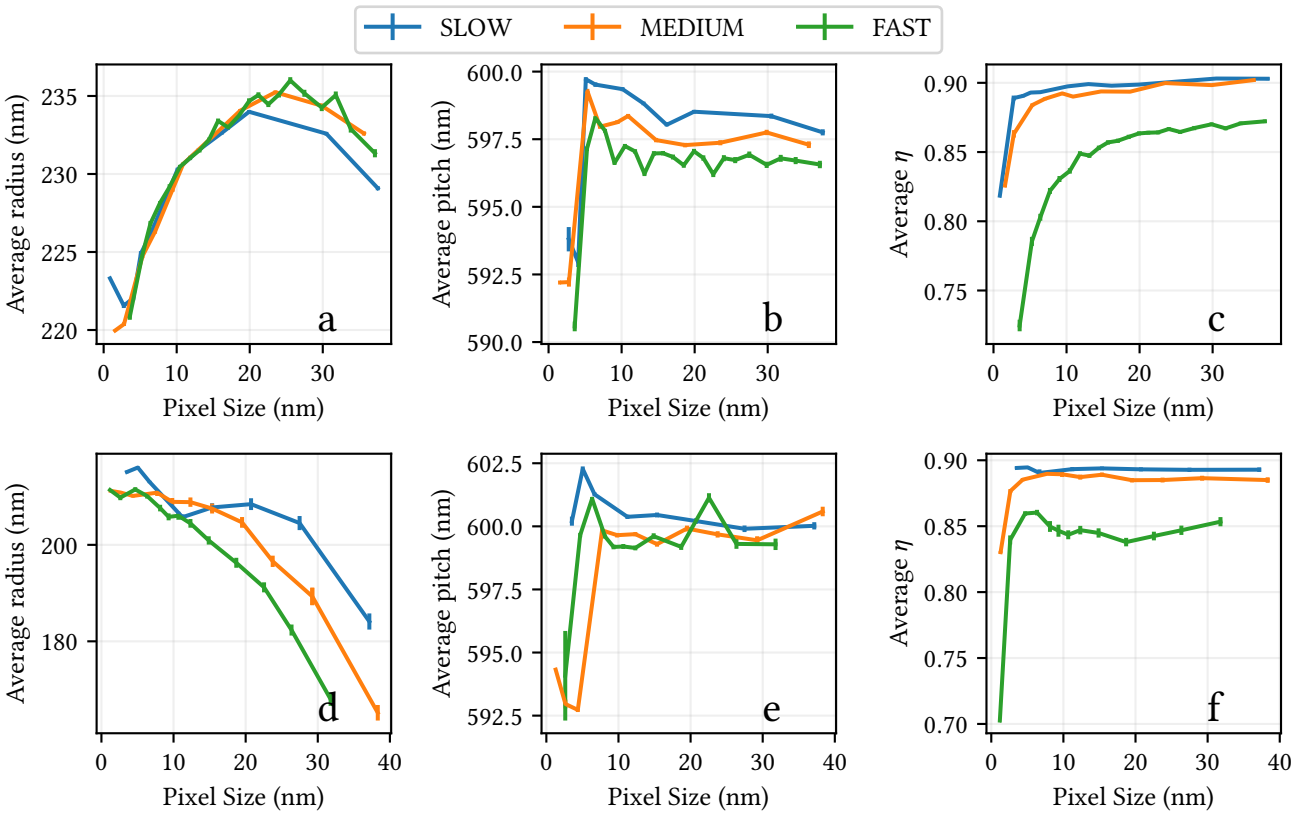

Figure 4.1: Averages of features extracted from SEM images of a photonic crystal for different scan speeds and levels of magnification. **a-c** is taken with the SE2 detector, and **d-f** is taken with the Inlens detector. The error bars represent the error of the mean.

It is compelling to interpret the maxima in the measured radius for the SE2 detector as the actual radius of the holes, as the distribution of the measured radii is more symmetric around the mean, and the deviations look more randomly distributed. This plateau happens around a pixel size of 20 nm, which means that for a circle of radius 200 nm, the circle would be represented by $\approx (2r/\text{pixel size})^2\pi/4 = 314$ pixels, which should be enough to describe the circle accurately. The sidewall tilt of our structures could explain that the two detectors measure radii that do not overlap, as the SE2 detector is more sensitive to edges at the surface of the structure. In contrast, the Inlens detector is more sensitive to the edges at the bottom of the holes. The sidewall tilt could cause the measured radius to be smaller for the Inlens detector than for the SE2 detector, as illustrated in fig. 4.3. The Si_3N_4 film here is 190 nm thick, and a measured difference in radius of 25 nm would thus correspond to a sidewall tilt of $\arctan(25/190) = 7.4^\circ$, which is not unreasonable.

The pitch is less sensitive to the SEM parameters. The measured value is confirmed

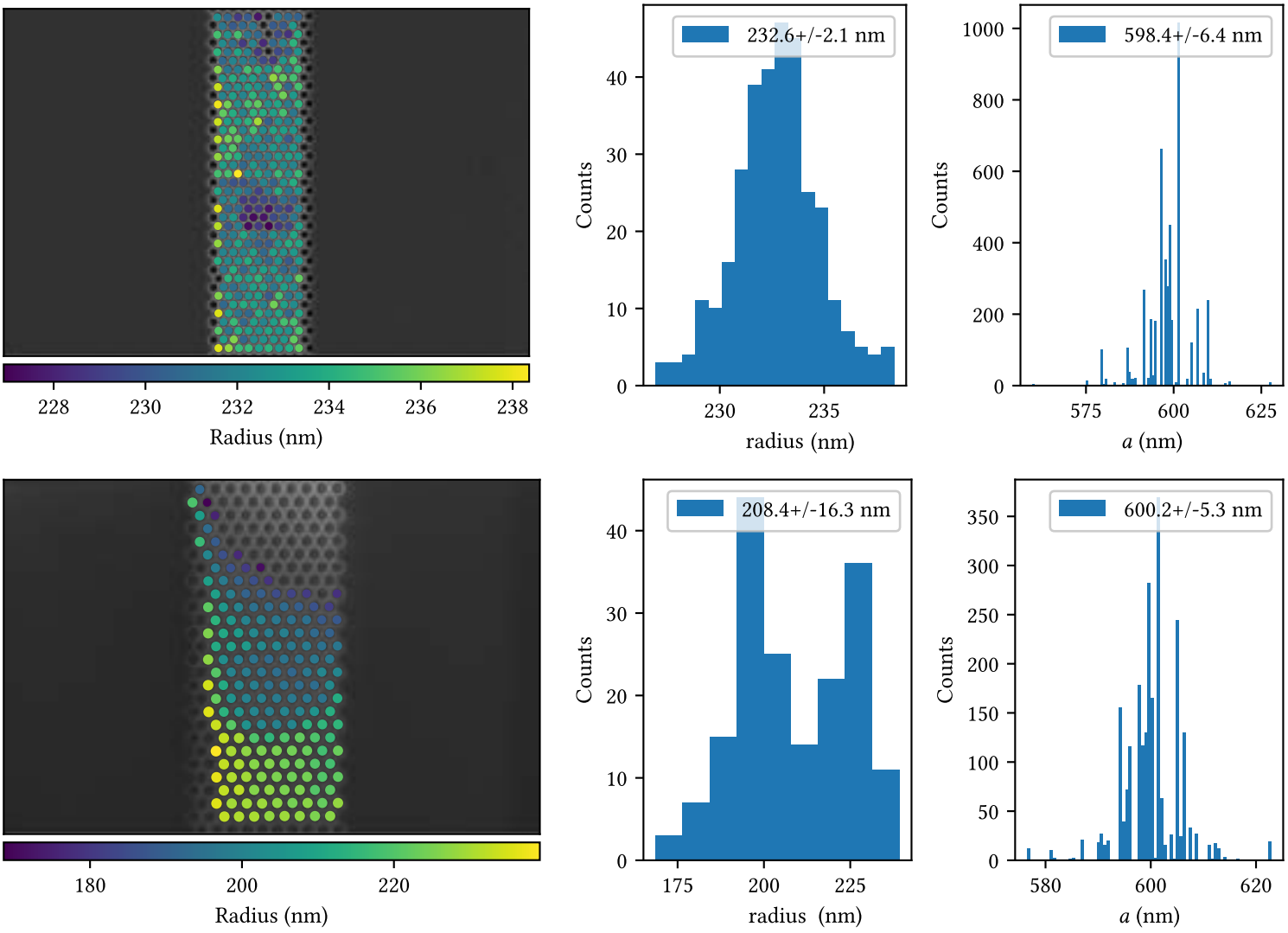

Figure 4.2: SEM Image analysis of the test device taken with the SE2 detector (top row) and the Inlens detector (bottom row) at the slowest scan speed. The leftmost shows the original image, with the color of the dots indicating the detected radius of the holes. The dot size is not representative of the measured radius. The two rightmost figures show the distribution of the detected radii and pitches, with the uncertainty shown in the legend being the standard deviation of the measured values, i.e., not the error on the mean. For the SE2 detector, we see that the distribution of the measured radii is somewhat symmetric around the mean and that the deviations look somewhat randomly distributed apart from a few islands. For the Inlens detector, there is a clear gradient in the detected radii, which coincides with the image's gradient and leads to a bimodal distribution of measured radii. This gradient causes the contour detection to fail towards the top of the image.

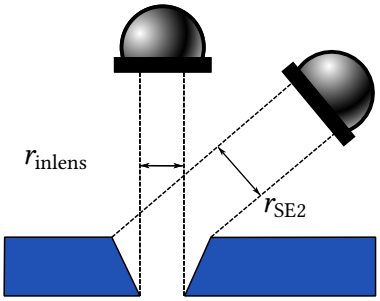

Figure 4.3: Schematic of the effect of sidewall tilt on the measured radius of a hole in a photonic crystal. The SE2 detector is more sensitive to the top edge of the hole, while the Inlens detector is more sensitive to the bottom edge. The sidewall tilt causes the measured radius to be smaller for the Inlens detector than for the SE2 detector.

by an AFM[3] measurement where the pitch is found to be (599.5 ± 0.1) nm. Still, it is interesting that the SE2 detector consistently measures a pitch 0.5 % smaller than the Inlens and AFM measurements.

The results of the SEM analysis show that the feature extraction is sensitive to the SEM parameters and that the Inlens detector is more sensitive to the scan speed than the SE2 detector. The Inlens detector is also more susceptible to imaging artifacts, which can influence the detected features. The difference in the radius measured by the two detectors suggests they may be imaging the holes' top and bottom, respectively.

Ultimately, these measurements have to be consolidated with optical measurements of the devices' in-plane optical properties. The SEM analysis provides a reasonably precise, if not very accurate, estimate of the feature sizes of the fabricated devices.

4.1.1 SEM Analysis of PhC

The chips described in section 3.0.1 had sections with PhC structures, and we use the procedure described above to extract the features of the released membrane from an image taken with the SE2 detector. These chips do not provide optical access to the in-plane modes of the structure, so this should be considered mostly a proof of concept. The target parameters for the device were $a = 405$ nm, and $r = 129$ nm, and from fig. 4.4 we find that the pitch matches well with the target, value, but the holes are smaller than the target design. We calculate the dispersion for these parameters and find that the Cs D2 line is in the air band of the structure and detuned by 2.4 THz from the band edge as shown in fig. 4.5.

To extend this analysis even further, the contour detection could be used to extract the detected geometry and export it to a format that can be imported into an FDTD

[3] Brüker AXS Dimension Icon-PT

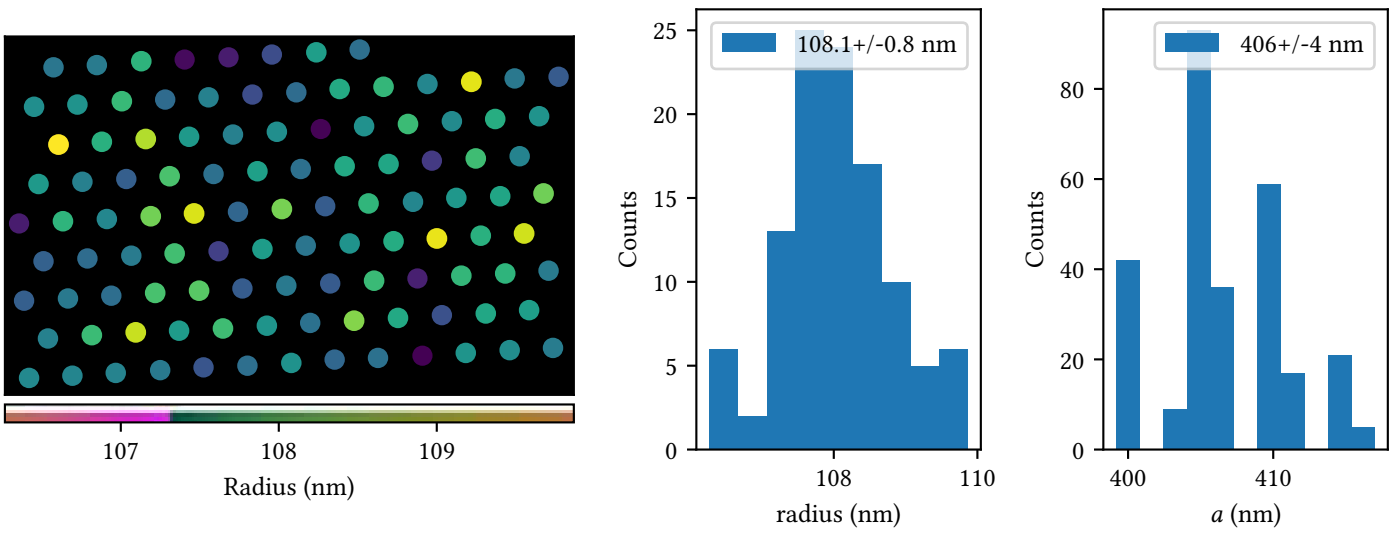

Figure 4.4: SEM image analysis of the PhC on the atom delivery practice chip.

solver. The simulations described in section 2.4.3 could then be performed with geometry that has been realized experimentally, to see what the effects of fabrication imperfections are on the FOMs.

Only preliminary work was done on this, namely, writing the code to extract the contours from SEM images and save them to .gds files that can be imported into, say, Lumerical.

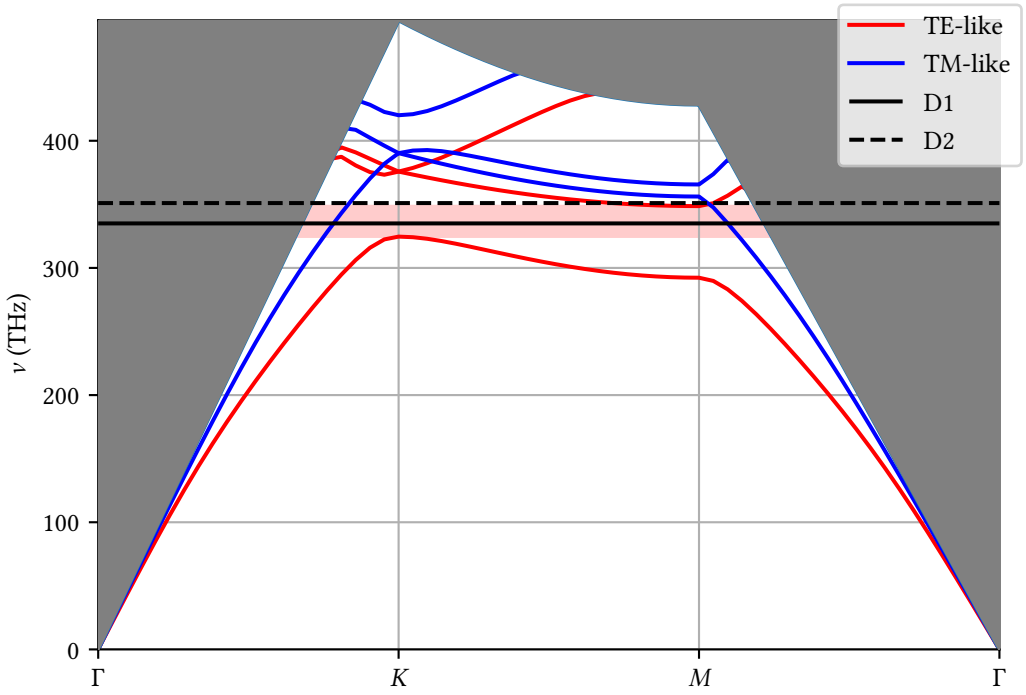

Figure 4.5: Band diagram for the parameters found using SEM analysis of the fabricated atom-transport chips. The deviation in radius from the target value has pushed the bandgap towards lower frequencies, and the D2 of Cs now couples to the propagating air mode.

4.2 Transmission Spectroscopy

To measure the in-plane optical properties of the fabricated devices, we use the setup shown in fig. 4.6. We do two types of spectroscopic measurements; one injects light from a superluminescent light-emitting diode (SLED)[4] and the transmission spectrum is measured on an optical spectrum analyzer (OSA)[5]. The other measurement uses a Ti:Saph laser[6] connected to a Wavemeter[7], where the transmission is recorded on an Avalanche Photo Detector (APD)[8].

To control the polarization of the incoming light, a set of achromatic $\lambda/4$ and $\lambda/2$ wave-plates are used together with a thin film polarizer. The light is coupled into a

[4]Initially, we used an InPhenix IPSDM0822-0813, but when one of the diodes burned out, we used an SLD850S-A20W driven by CLD1015, both from Thorlabs.

[5]Anritsu MS9740B

[6]Initial measurements were done using a Spectra-Physics Matisse CR laser generously borrowed by Sebastian Hofferberth. As this had to be returned, the later measurements were done using a M Squared Solstis laser borrowed from a different experiment in the lab.

[7]HighFinesse WS7

[8]Thorlabs APD120A

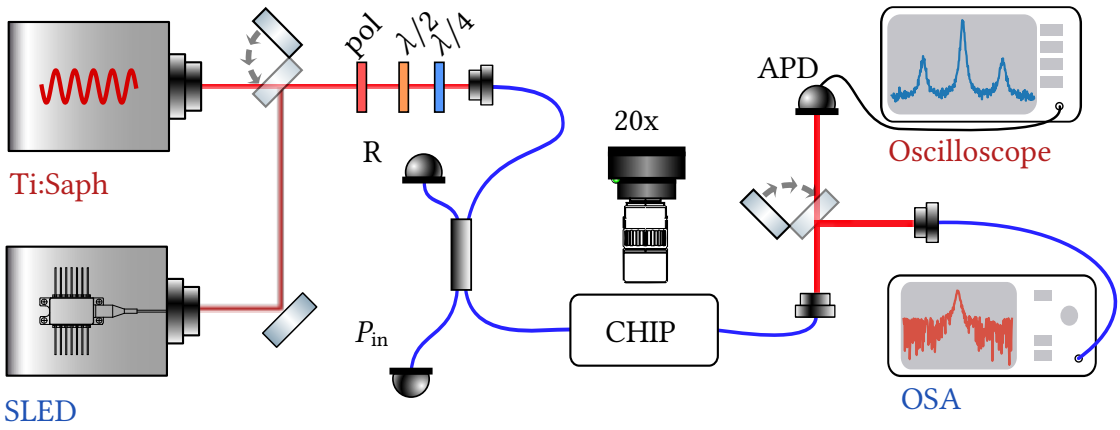

Figure 4.6: Schematic of the transmission setup. Light from either the Ti:Saph or the SLED passes through a thin film polarizer and two achromatic retardation plates before being coupled into a 50/50 fiber BS. The light is then coupled into the chip with an AR-coated fiber, and the light is collected with another AR-coated fiber. The light is then sent to an OSA or an APD, and the chip is imaged with a 20x microscope.

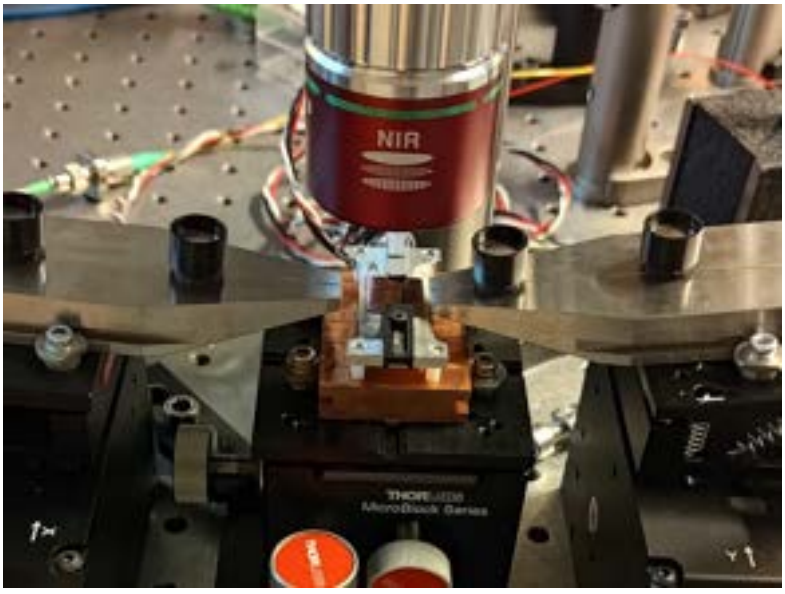

Figure 4.7: Chip-Fiber coupling setup. The chip is mounted on the central stage, and the fibers are mounted on the two 5-axis stages to either side. A microscope objective images from above.

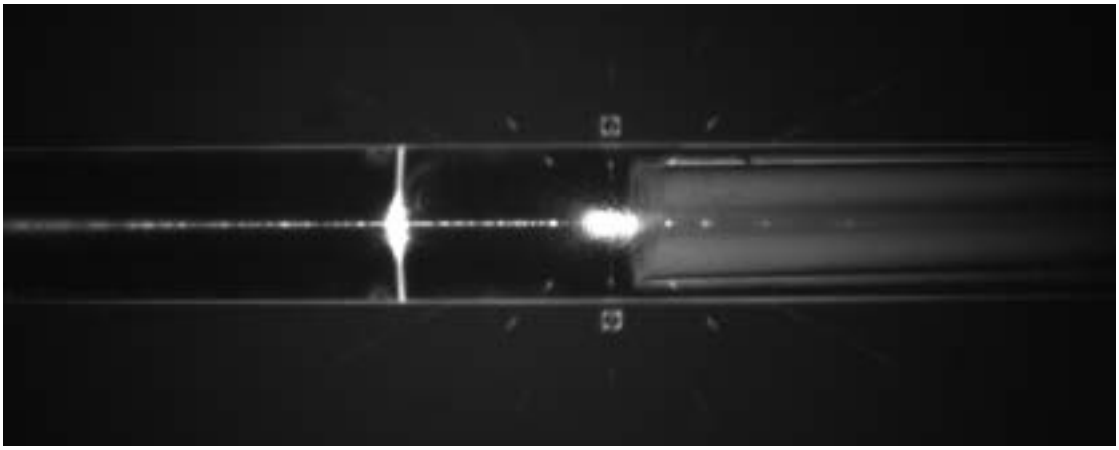

Figure 4.8: Microscope of the waveguide as light is being coupled in with an optical fiber. Light propagating in the waveguide is scattered onto the camera, and we see that the first tether array and the coupling tether scatters more light.

50:50 fiber beam-splitter, where one port is sent to the device and the other is used to monitor the power of the injected light. The light is delivered to and siphoned from the chip with an anti-reflection (AR) coated 780-HP fiber[9], stripped to the cladding on the last 10 mm.

Fiber to Chip Coupling

The chip is mounted on a custom chip holder, where the chip is secured by a trapezoidal piece of metal that is fixed by a screw. The chip holder is a ridge that allows access from two sides and is mounted on a 3-axis stage. The fibers are held on tapered V-groove fiber holders mounted on 5-axis stages[10] A camera with a microscope objective and a variable zoom lens tube is mounted above the setup fig. 4.7.

The procedure for coupling light into the waveguide using the fiber is as follows: The fibers are tilted towards the chip and positioned above the V-groove. With the tip of the fiber at a safe distance from the waveguide coupler, the fiber is lowered into the V-groove until the tip of the fiber is flush with the bottom of the groove. The light source is turned on, and the injection fiber is moved toward the waveguide coupler while monitoring the camera. By looking at the first section of the waveguide, it is possible to see when the fiber is in physical contact with the waveguide coupler by looking for a distortion of the light in the waveguide. The fiber is backed off until the distortion disappears. When light is coupled into the waveguide, the outcoupling fiber

[9]The AR coating is the broadband RARe Motheye coating provided by amstechnologies
[10]A PY003/M mounted on a NanoMax 3-axis stage, both from Thorlabs.

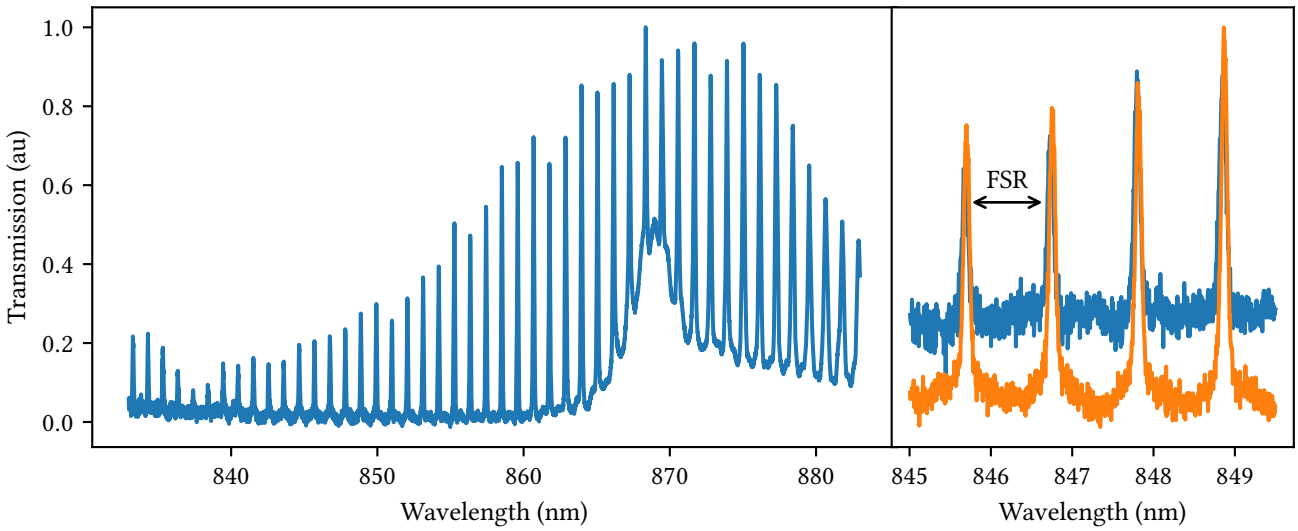

Figure 4.9: SLED spectrum. Left is the broadband spectrum of a device with a Fabry-Perot cavity. The right figure is zoomed in, and the effect of aligning the polarization to the TE mode is shown; transmission between resonances is suppressed.

can be aligned as described above. An image of a waveguide with light coupled in is shown in fig. 4.8.

We look at the light scattered in the microscope objective to align the polarization. The TE mode is polarised parallel to the plane of the waveguide. For impurities much smaller than the wavelength, the scattered light follows a dipole emission pattern where no light is radiated in the direction of the dipole, and thus, for the TE polarization, maximal radiation is expected in a direction perpendicular to the plane of the chip. To align the polarization with the TE mode, we maximize the camera signal, and to align with the TM polarization, we minimize it.

This procedure should be done using a monochromatic light source, as the camera's sensitivity is also wavelength-dependent. For devices with spectral features, such as the DBR mirrors in the cavities described in section 2.3, we utilize that the mirrors are designed to be highly reflective in the TE polarization but not in the TM polarization and thus by minimizing the transmission between resonances of the cavities, the polarization is aligned to the TE mode. The finite bandwidth of the optical elements means that this can only be done in a narrow wavelength range, and it should thus be optimized for the wavelength of interest for a given measurement.

4.2.1 Cavity Finesse Measurements

We do a two-step measurement to measure the linewidth of the cavities described in section 2.3. First, the broadband spectrum is measured with the SLED and OSA to determine the location of the cavity's resonances as shown in fig. 4.9. The resonant wavelengths are determined from Lorentzian fits to the OSA spectrum. The laser is then tuned to these wavelengths and a scan of 100 GHz around the resonance is done with the internal etalon scan of the laser. The transmission signal on the APD is recorded with the input power measured on the other port of the input BS and the wavelength measured on the wavemeter.

The OSA and wavemeter are not perfectly calibrated, and thus, it is necessary to determine the offset between them. To determine this offset, we tune the laser to one of the resonant wavelengths determined by the OSA measurement and then manually tune the laser while monitoring the cavity on the camera. When the cavity is in resonance, the light build-up is easily seen, and the offset is recorded and used as an offset for all of the OSA measurements.

For the shorter cavities, the linewidth of the resonances can be determined directly from the OSA data. Still, for the longer cavities, the linewidth is smaller than the resolution of the OSA. Some effort was made to determine the linewidth from the OSA data by deconvolving the measured resonances with the instrument function of the OSA, but this was not feasible for linewidths comparable to the OSA resolution of 0.07 nm.

When inspecting the resonances, it became clear that they were not all simple Lorentzians, and to fit the data, we used an asymmetric Fano resonance.

$$F(\lambda) = \frac{A}{1+q^2} \cdot \frac{(\epsilon+q)^2}{1+\epsilon^2} + B, \tag{4.2.1}$$

where $\epsilon = \frac{\lambda-\lambda_0}{\delta\lambda/2}$, with $\delta\lambda$ being the full-width-half-maximum (FWHM) of the peak, and λ_0 being the central wavelength of the peak. A is the amplitude of the peak, B is a constant background, and q is the asymmetry parameter. For $q = 0$, this becomes a Lorentzian.

The Fano resonance accounts for the asymmetry of the resonances, which is likely caused by coupling to a continuous channel or a broad cavity. The DBR mirrors are a cavity, and one hypothesis would be that the intra-cavity modes couples to etalon modes of the DBR mirrors, arising from the finite length of the DBR mirrors.

The $\Delta\lambda_{\mathrm{FSR}}$ for a given resonance is determined as the average distance to the two neighboring resonances, and the Finesse is then calculated as

$$\mathcal{F} = \Delta\lambda_{\mathrm{FSR}}/\delta\lambda \tag{4.2.2}$$

For several of the measured devices, we observed mode-dependent losses where the Finesse of the resonances oscillate from mode to mode as seen in fig. 4.10.

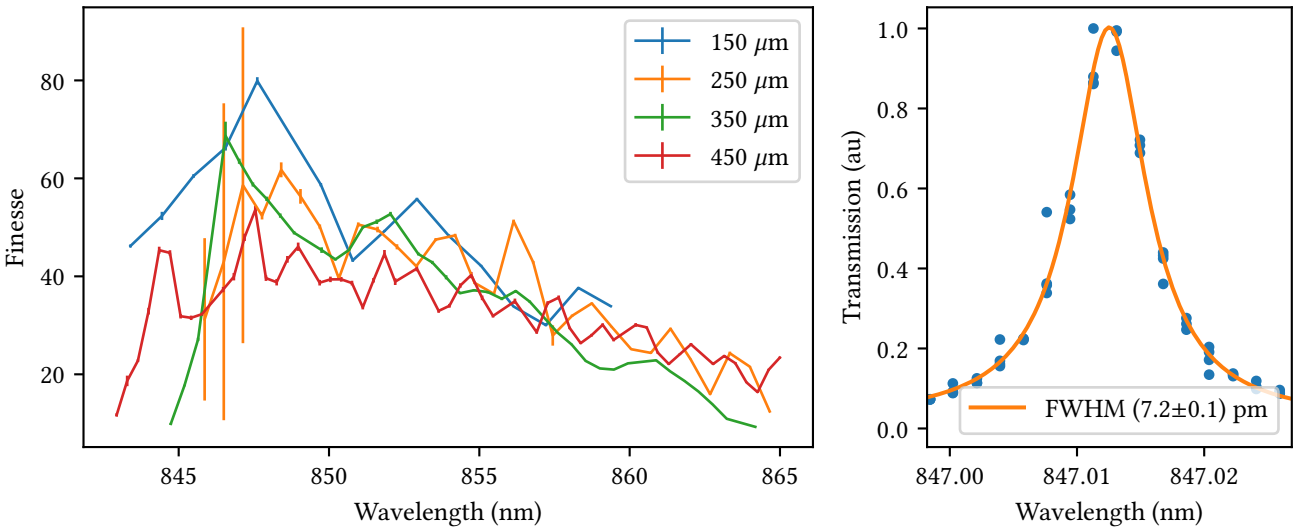

Figure 4.10: Left: The Finesse of the measured devices as a function of wavelength. The Finesse is calculated from the resonances' measured line widths and the neighboring modes' spectral spacing. **Right:** The linewidth is determined from a fit to the transmission spectrum of the cavity.

That the Finesse is wavelength dependent is expected, as the reflectivity of the DBR mirrors also has a strong wavelength dependence, but a substantial difference in Finesse between two neighboring modes is not expected inside the Bragg window of the DBR. The rapid variations in Finesse may be caused by local scatterers on the waveguide interior, which are then sampled differently by the standing waves of different cavity modes. To investigate this further, we image the waveguide on resonance with a camera as shown in fig. 4.11. The images show that the intensity of the scattered light at a given point in the cavity is periodic in wavelength, with the periodicity depending on the position in the cavity. On resonance, the light in the cavity is a standing wave with $m = 2Ln_{\text{eff}}/\lambda_0$ anti-nodes, where L is the length of the cavity, n_{eff} is the effective index of the cavity mode, and λ_0 is the wavelength of the resonance. Modes with an anti-node at the point of a scatterer will be more sensitive to the scatterer than modes with a node at the scatterer, which could explain the observed mode-dependent losses. We see that the modulation of the scattered light intensity is most rapid around $L/4$ and $3L/4$, and not at the center of the cavity. From an intuitive picture of a standing wave between two mirrors, we would expect the modulation to be the fastest at the center of the cavity, where the standing wave has alternating nodes and anti-nodes for consecutive mode numbers. The observed modulation would be consistent with this model if we only saw every other mode such that there are no modes with an anti-node at the center of the cavity. Still, comparing the measured FSR to the expected FSR for

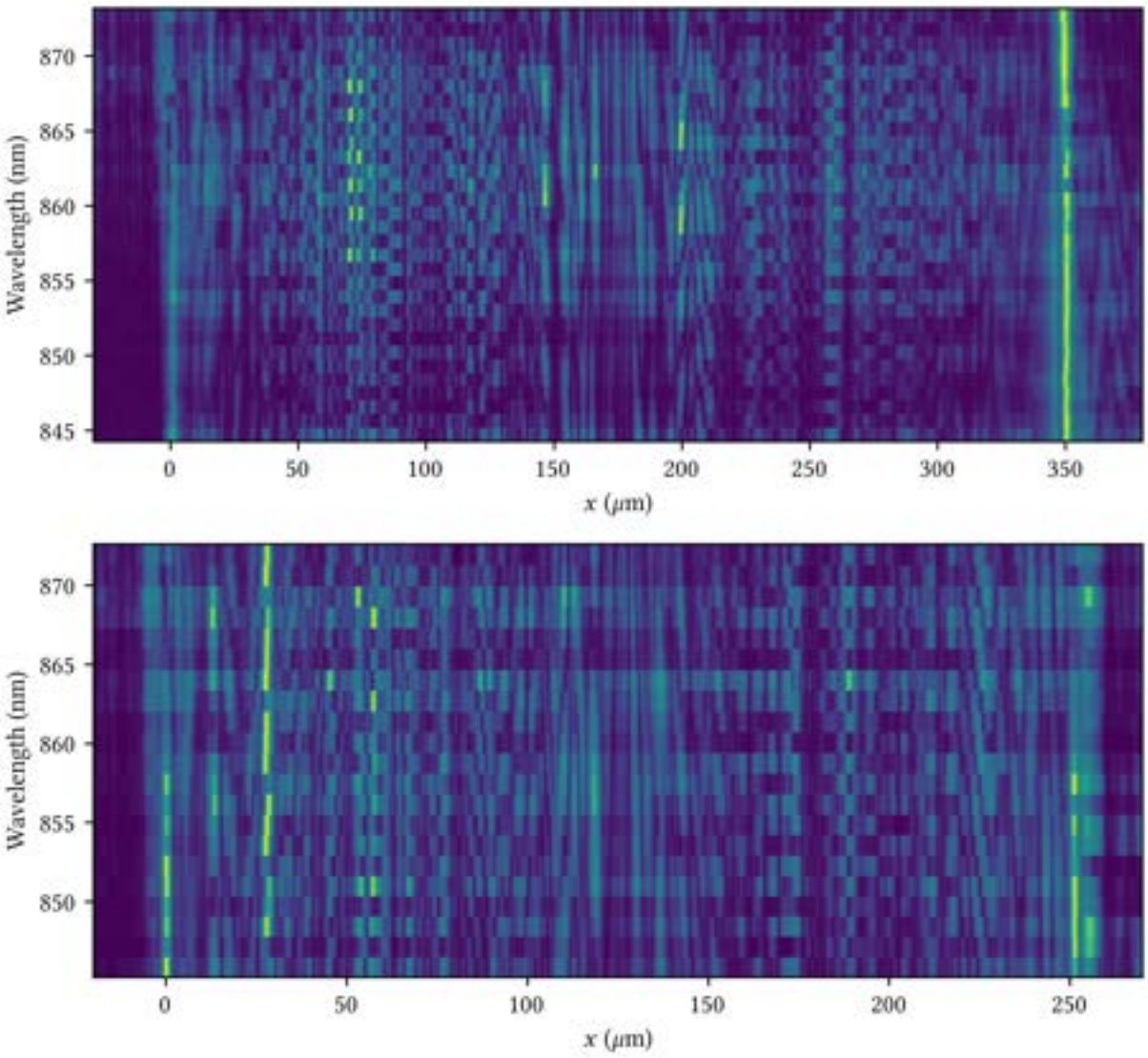

Figure 4.11: Images of the TE resonances of the waveguide cavity. Each horizontal line is obtained from an image of the cavity on resonance. By taking the maximum pixel value along a line perpendicular to the waveguide we get a line representation of the light scattered off the waveguide. Yellow corresponds to a high intensity of scattered light. The top figure is for a resonator of length L =350 µm, and the bottom is of a resontor of length L =250 µm. We observe a position-dependent modulation of the scattered light intensity as a function of wavelength and note that the modulation seems to happen most rapidly around $L/4$ and $3L/4$.

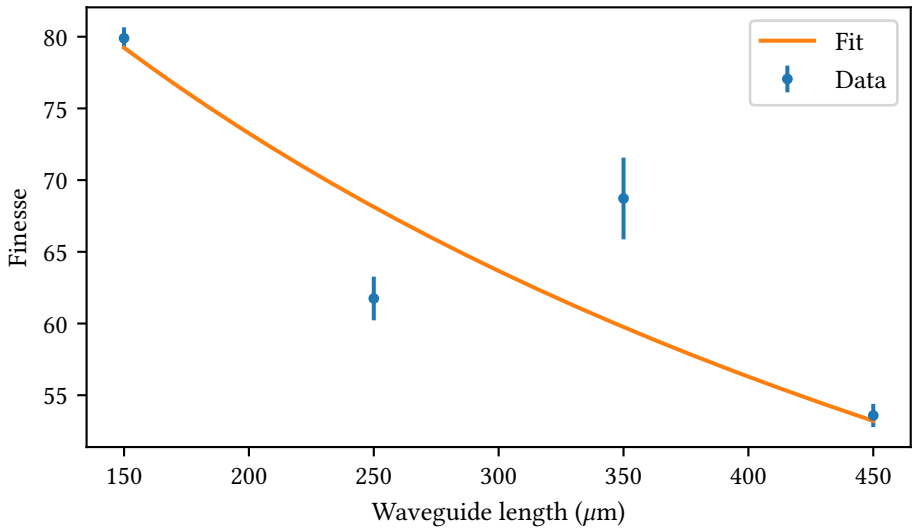

Figure 4.12: The measured relationship between cavity Finesse and cavity length. From a fit to eq. (2.3.3) we find a propagation loss $\alpha_{\mathrm{dB}} = (2.8 \pm 0.5)\,\mathrm{dB\,cm^{-1}}$ and mirror reflectivity $R = (97.0 \pm 0.3)\,\%$. We observe that the uncertainties on the observed finesses suggest that the model function does not fit the data.

a given cavity length, we see that the measured FSR is consistent with the expected FSR. The imaging system cannot resolve the standing wave pattern, and the observed slow modulation at the center of the cavity could be a form of aliasing caused by the limited resolution of the imaging.

Regardless, the position-dependent scattering loss could help explain the mode-dependent losses observed in the Finesse measurements.

When modeling the loss from the waveguide, the most accurate result is obtained by comparing the Finesse from resonances at the same wavelength where the reflectivity of the DBR is nominally identical. Still, given the mode-dependent losses, this is not possible. We resort to comparing the highest measured Finesse for each cavity length, irrespective of the wavelength of the resonance. The fit to the Finesse as a function of cavity length is shown in fig. 4.12, where propagation loss $\alpha_{\mathrm{dB}} = (2.8 \pm 0.5)\,\mathrm{dB\,cm^{-1}}$ and mirror reflectivity $R = (97.0 \pm 0.3)\,\%$ are found. Fitting the model to this data hardly seems reasonable, given the amount of data and the quality of the fit. Still, it is done here to illustrate the procedure for future reference.

The devices measured here were fabricated towards the end of the project, and due to time constraints, only a very small number of devices were available for measurements. The results here are not as conclusive as we would have liked, and further measurements are needed to confirm the results. What is presented here does suggest that the technique is feasible, and we have a good idea of how to proceed with further

measurements, namely to change to a corrugated mirror design that allows for much higher cavity Finesse, making the sensitivity to propagation losses higher.

This measurement technique and the results presented here can be seen as a point of comparison for future changes to the fabrication process.

4.3 Scanning Near-Field Optical Microscopy

At the heart of the LAQS experiment, we want to trap single atoms in the evanescent field of a photonic crystal, and as such, the field at the surface of the crystal is of great interest. Some information about the distribution of the field can be extracted from optical imaging. Still, the minimal resolution d is limited by diffraction to $d = \frac{\lambda}{2\mathrm{NA}}$ where NA is the numerical aperture of the microscope objective used to image. For visible light of 500 nm, the resolution is limited to around 300 nm, which is not sufficient to resolve the features of the photonic crystals. A solution to overcome this limit is to use a Scanning Near-Field Optical Microscope (SNOM). The working principle of a SNOM is to have a sharp tip that is brought close enough to the surface of the sample that it interacts with the evanescent field of a guided mode in the structure. Scanning the tip across the surface while collecting the light that has either been scattered by or transmitted into/from the probe makes it possible to create a topological image with a resolution beyond the diffraction limit. The fundamental principle of a SNOM was proposed already in 1928 by Synge [71], with the first experimental demonstration of what they refer to as an "optical stethoscope" happening in the 1980s [72]. Here, we will provide only a very basic overview of the operation of a SNOM, but we recommend [14] as a good reference for the theory of SNOM.

There are, generally speaking, two types of SNOM: aperture SNOM (a-SNOM) and scattering SNOM (s-SNOM). In the former, the light is injected or measured through a sub-wavelength size aperture at the apex of a tapered fiber. The aperture is created by coating the tip of the fiber with a metal and milling a sub-wavelength size hole at the end using focused ion beam (FIB) milling [73]. With this type of measurement, the resolution is limited by the size of the aperture, which is limited by the amount of power that can be transmitted through the aperture without damaging the probe. The size of the aperture is thus a trade-off between resolution and signal-to-noise ratio, with typical aperture sizes around 100 nm to 150 nm. This type of SNOM has three types of operation shown in fig. 4.13. In illumination mode, the sample is illuminated by light coming from the tip, and a detector collects the light transmitted through the sample. In reflection mode, the light is injected and collected by the tip, and in collection mode, the sample is illuminated by an external source, and the tip collects the light. In s-SNOM, a sharply tipped probe, either metal coated or dielectric, scatters light from a laser beam that is focused onto the sample and into the structure. The sharpness of the tip limits the resolution and can be much higher than that of the a-SNOM, with

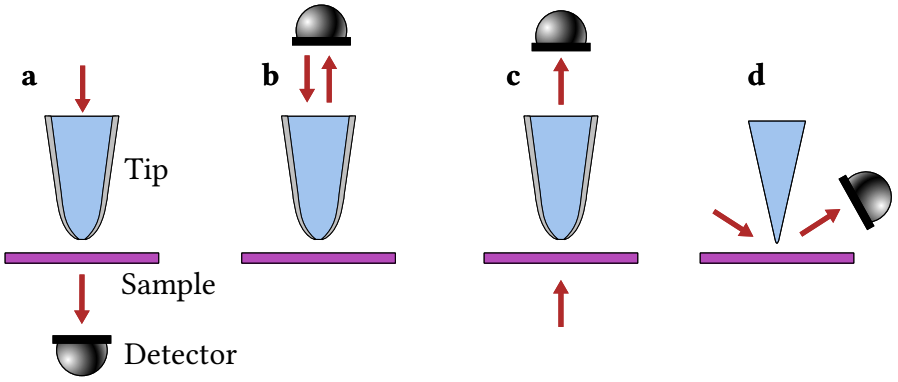

Figure 4.13: Four modes of operating SNOM. **a** Illumination mode. The probe is used to illuminate the sample, and a detector in transmission collects the light. **b** Reflection Mode. The probe is used to illuminate and collect light from the sample. **c** Collection mode. An external source illuminates the sample, and the SNOM collects light. **d** Scattering mode. The probe scatters light from an external source into the sample, and a microscope objective collects the scattered light. The apertureless probe can be tapered to a finer point.

resolutions of down top 5 nm to 10 nm [74]. To measure the light scattered from the tip above the background of light scattered from the surface of the sample, interferometric heterodyne detection is often used, where the light scattered from the tip is mixed with a reference beam of light and subsequently demodulated at the mechanical frequency of the tip [75].

Both types of SNOM have been demonstrated as powerful tools for characterizing PhC devices. For example, the extraction of dispersive features from a periodic waveguide [76] using a s-SNOM, the full vectorial mapping of the electric field of a PhCWg [77] using a-SNOM, and more recently it has been used to demonstrate Anderson Localization in disordered photonic devices [78]. It has been proposed that using two s-SNOM measurements with different-sized probes makes it possible to measure the LDOS directly [79]. With an a-SNOM, it is possible to probe the polarization dependence of the coupling to various in-plane photonic modes [80], which could enable the mapping of the coupling to the in-plane modes of the PhC of a dipole emitter as simulated in section 2.4.3.

We decided to purchase a SNOM system from Mad City Labs, which consisted of a piezo-actuated 3-axis nanoposition stage, a motorized 3-axis μposition stage for the probe, and a 2D manual μposition stage as well as electronics for closed loop operation and the electronics for doing surface force feedback. By default, this system is set up for a-SNOM but can, in principle, be modified to do s-SNOM. It is a modular system in that most of the components can be swapped out for other components, the system can be expanded with more stages and detectors if necessary, and the stages can be used for other purposes. Mad City Labs also provides a more complete solution, but

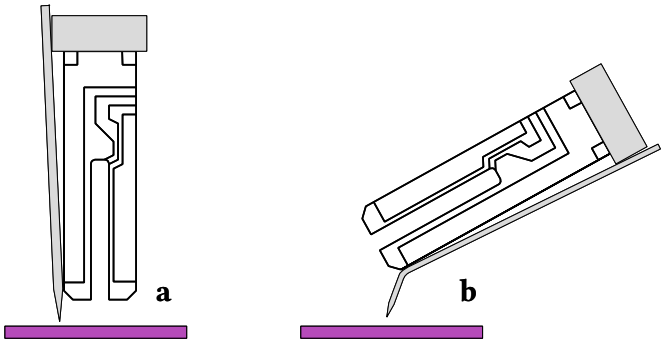

Figure 4.14: Types of SNOM tips. **a** Straight tip using shear-force feedback. **b** Angled tip using normal-force feedback.

we opted for a 'lightweight' system where we would be supplying our light source and detectors.

The system accommodates a variety of probes, but for the time being, we have been using tuning-fork probes. We will discuss the probe in more detail in the following section.

The system was assembled, and some initial tests were done. Still, due to a combination of time constraints and lack of availability of a tunable light source, the system was not used for measurements in this project. The progress made with the system is documented here in the hopes that this will be useful for future work. Some modifications may be necessary before the system can be used for the intended purpose, and these are discussed in one of the following sections. Discussions with the group of Martijn Wubs, where there is extensive knowledge about s-SNOM, revealed that the acquisition and analysis of SNOM data is a non-trivial task, which also steered the project away from using the SNOM system for the time being. With the acquisition of a tunable light source and a few modifications, some initial measurements could and should be made and may reveal interesting information about the devices fabricated in this project.

4.3.1 Sample-Probe Distance Control and Probe Assembly

The probe is a 780HP SM fiber with one end tapered and coated with Al and a nominal aperture- diameter of 100 nm[11], glued to a quartz tuning fork[12]. The distance to the sample is maintained using shear-force or normal-force feedback, see fig. 4.14. The amplitude of motion for the probe can be described as a harmonic oscillator with a resonance frequency $\omega_o(d)$ and damping $\gamma(d)$ where the dependence on the tip-sample distance d originates from viscous surface-forces[81]. For a harmonic driving force of

[11]K-Tek Nano, E50-780HP-AL-100.
[12]Purchased from Mad City Labs

magnitude F and angular frequency ω, the motion of the probe can be written as

$$x(t,d) = \frac{\frac{F}{m}}{\omega_0(d)^2 - \omega^2 - i\gamma(d)\omega} e^{-i\omega t}, \tag{4.3.1}$$

which is a Lorentzian lineshape with m being the effective mass of the mode of operation. As the probe moves towards the surface, this causes a frequency shift and amplitude change in the probe, which can be measured in the piezoelectric signal from the tuning fork. A piezo-actuated z translation stage actuates the position of the probe, and by using either the amplitude or frequency shift as an error signal, the probe's position can be held constant with a PI controller. For typical tuning fork parameters, it can be shown that detecting the change frequency is far more sensitive than detecting a change in amplitude [14, chapter 7]. The driving force depends on the mode of operation, but it will drive the tuning fork close to resonance, either with a synthesized signal or an amplified signal from the tuning fork itself.

The mechanical Q of the probe, which for the bare tuning fork is typically $10^3 - 10^4$, must remain above a certain level for the frequency shift to be measurable, and we found that the process of gluing the fiber to the tuning fork affected this Q substantially. The probe assembly procedure is as follows.

1. The quartz tuning fork is soldered to the PCB, adjusting the angle of the tuning fork to be perpendicular to the PCB for straight fibers or at a slight angle for angled fibers.

2. The probe board is placed in the setup shown in fig. 4.15, and the fiber is placed in the V-groove next to the probe holder

3. The pitch, yaw, and linear positioners (shown in pale blue) align the fiber so that the fiber touches the barrel of the tuning fork and a point close to the tip of one prong. The tip of the fiber should only protrude slightly from the tip of the tuning fork.

4. Two drops of UV-curable glue are placed at the two contact points with a microlance syringe, and the fiber is lowered onto the tuning fork using the z translation stage (shown in orange).

5. The glue is cured with a UV lamp (purple) for about 5 minutes.

The third step proved to be crucial for creating a usable probe. If the fiber is not aligned properly, the glue will cause the tuning fork to bend, and the Q of the probe is immeasurably low. The Q can be measured with the software provided by the manufacturer, and for proper gluing, the Q was found to drop from around 1900 to around 1500.

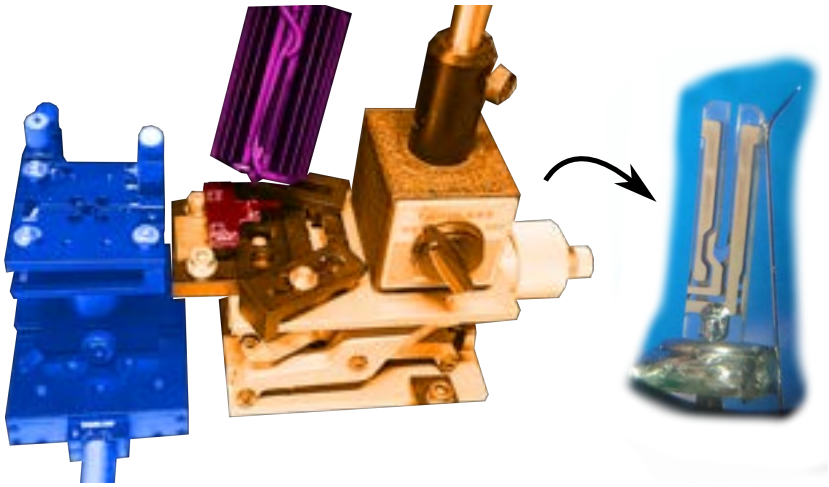

Figure 4.15: The probe assembly rig on the left and a successfully glued fiber probe. The blue stage positions the fiber to align correctly with the tuning fork. The orange stage moves the fiber into contact with the tuning fork. The UV lamp, shown in purple, is used to cure the two drops of UV glue placed at the contact points. On the right is a successfully glued probe.

4.3.2 Strehl Ratio Measurement and Aperture Probe PSF

A 'simple' measurement using an aperture probe could be to image a photonic crystal structure with an optical microscope while a SNOM tip is placed close to the surface. The light from the tip will interact with the evanescent field of the structure, and the light collected by the tip can be imaged on a camera. The optical microscope could not resolve features smaller than the diffraction limit. Still, the anisotropic emission pattern predicted when emitting in a flat-band region of the dispersion curve should produce an emission pattern spanning several unit cells fig. 2.14. With a diffraction-limited imaging setup, this may be resolvable, and the emission pattern could be used to determine the band edge frequency for a given crystal. It would be a nice measurement in itself.

We did not reach a point where this measurement could be performed, but progress on the necessary step of assessing the imaging system's quality was performed, and it is presented here.

To assess the quality of our imaging system, we used the SNOM tip as a point source to measure our system's PSF. In the context of an image, the point spread function describes the response of an imaging system to a point source analogously to the electronic case eq. (3.4.3), and any image obtained with a given system can be calculated as the convolution of the imaged object $O(x_i, y_j)$ with the PSF of the system

$$I(x_i, y_j) = \int\int O(u, v)\mathrm{PSF}(x_i - u, y_j - v)\mathrm{d}u\mathrm{d}v, \tag{4.3.2}$$

where $\mathrm{PSF}(x_i - u, y_j - v)$ is the image of a point source $\delta(x_i - u, y_j - v)$. While a

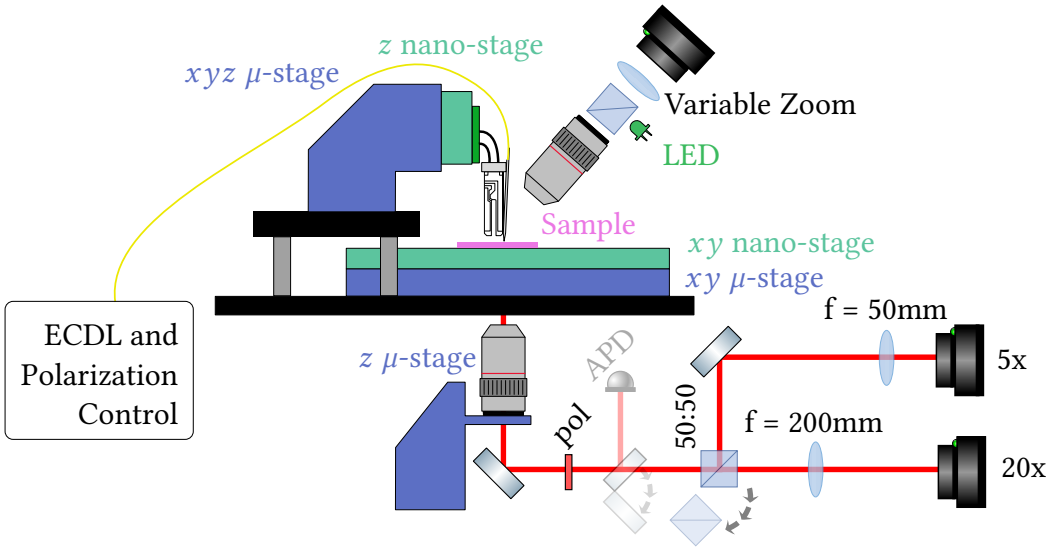

Figure 4.16: Schematic of the SNOM setup. In this configuration, it runs in illumination mode. The light from the SNOM tip is collected by the objective and imaged on the camera. Another camera with 5x magnification can be used to navigate the sample by placing a beamsplitter in the path. Another camera is mounted above the sample to work with opaque samples. The APD would be placed in the beam path for SNOM measurements.

physical point source does not exist, our SNOM tips' aperture is much smaller than the imaging system's resolution and should allow us to measure the PSF. Knowing the PSF, images obtained in this imaging system can be deconvolved to remove or reduce artifacts caused by aberration in the imaging system. In the case of Poissonian noise, the iterative Richardson-Lucy algorithm can be used, [82][83] and in the case of Gaussian additive noise, a Wiener filter can be used [84].

A figure of merit typically used to assess the quality of an imaging system is the Strehl ratio, which is defined as the ratio of the peak value of the PSF to that of an ideal, aberration-free imaging system. For such an imaging system, the only limit is diffraction, and the PSF is an Airy disk [85]

$$\mathrm{PSF}_{\mathrm{Airy}}(x, y) = \left(\frac{2J_1(kr)}{kr} \right)^2, \tag{4.3.3}$$

where J_1 is the Bessel function of the first kind and $k = 2\pi/\lambda$. A system is said to be diffraction-limited when the Strehl ratio,

$$S = \frac{\mathrm{PSF}(0,0)}{\mathrm{PSF}_{\mathrm{Airy}}(0,0)}, \tag{4.3.4}$$

is ≥ 0.8.[86]

The imaging system here consists of a Mitutoyo M Plan APO NIR B 20X objective and a 200 mm infinity-corrected tube lens from Thorlabs with a FLIR Blackfly camera. An overview of the SNOM setup is shown in fig. 4.16, with the imaging system considered here being the one underneath the sample. The PSF was measured by scanning the SNOM tip across the field of view of the camera, as well as through the focal plane of the microscope while imaging the SNOM tip at each position. The light source used for the SNOM tip was a home-built ECDL laser with a wavelength of 854 nm. We found that the PSF of the imaging system was asymmetric, which could be caused by the aperture of the SNOM probe not being parallel to the focal plane. The cause of this asymmetry could be either the aperture of the emitter not being parallel to the focal plane or an asymmetry of the probe aperture.

The SNOM probe used in this measurement is imaged with SEM and shown in fig. 4.17. There appears to be some damage to the probe used here, and a piece of the metal coating is protruding on one side of the tip.

Regardless of the cause of the asymmetry, we can get an approximate value for the Strehl ratio by calculating the Strehl ratio along different 1D cuts rotated around the center of the measured PSF. This approach measured the maximal Strehl ratio to be around 0.72, close to the diffraction limit. An image of the radiating SNOM probe used here is shown in fig. 4.18. A rigorous measurement of the Strehl ratio would require careful optimization and is beyond this project's scope. Still, the measurement presented here does suggest that the imaging system is close to diffraction limited. An alternative way to view this measurement is to see it as a way to verify the quality of a SNOM probe without having to use an SEM. If we can verify that our imaging system is indeed (at least close to) diffraction limited, any excess spread in the PSF will be caused by a faulty probe aperture. This would require a measurement of the PSF, either by an undamaged aperture probe or by using a calibrated pin-hole. Whether the asymmetry seen in fig. 4.18 is caused by the probe aperture or the imaging system is as of yet undetermined.

4.3.3 Future Work

This system has not been utilized yet, and with the recent arrival of a Ti:Saph in the lab, there are plenty of interesting things to try out. The polarization state at different wavelengths at the output of the SNOM tip should be measured for straight fibers and bent fibers, as these have been observed to behave differently [87]. The measurement described in the previous sector should, in principle, be straightforward but should be compared against numerical simulations. Some initial work on FDTD simulations of the SNOM fiber and the photonic crystal has been done, but further work is needed.

To combine the SNOM with our 1D waveguide structure, a modification to the configuration of translation stages is necessary. The probe remains stationary in the xy plane, and the sample is scanned using the nano-xy positioner. Moving the sample

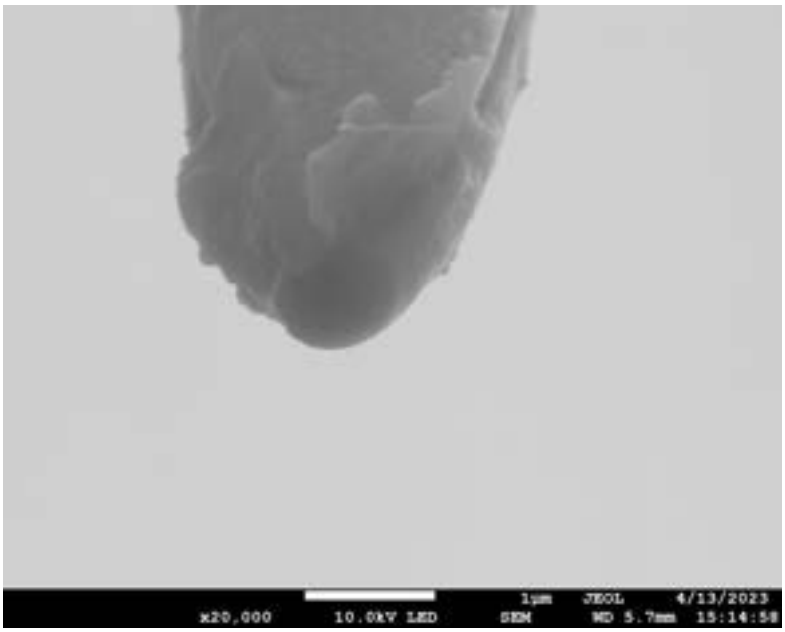

Figure 4.17: SEM image of a SNOM tip. Some damage appears to have been done, which could explain the asymmetric emission pattern.

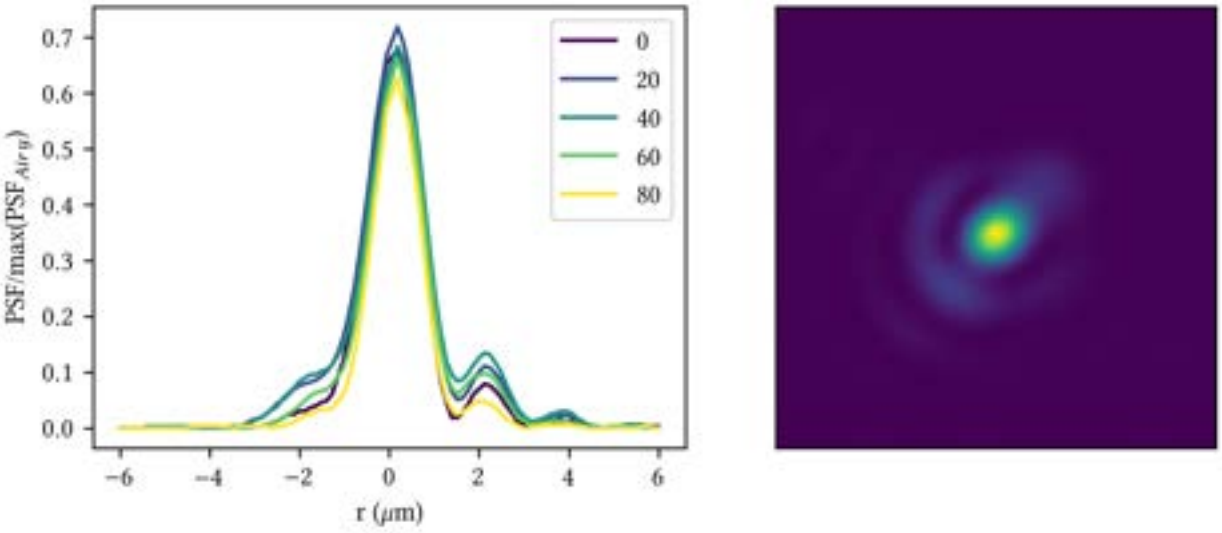

Figure 4.18: Right: Image of the SNOM tip, where we see an asymmetric fringe pattern. Left: Line cuts through the center for different angles, the asymmetry of the PSF gives a different Strehl ratio at different angles.

is problematic, as the scanning motion will affect the coupling into the chip. One option is to glue the fiber to the V-groove before scanning, which would make the measurement destructive. The other, arguably better, option is to swap the position of the sample and the probe, such that the probe is scanned in the xy plane and the sample is stationary. Keeping the sample stationary requires a new sample holder and an adapter for mounting the probe and the z nano-positioner on the xy nano-stage and a sample holder mounted on the xyz μ-positioner. A third option would be to use piezo-actuated stages for the coupling fibers or objectives to move the fiber with the sample as it is scanning. By sending the (properly attenuated) signal for the piezo stages controlling the xy movement of the sample to the xy stage controlling the light source's position, the coupling changes can be minimized.

4.4 Thermo-Mechanical Measurements

The mechanical motion of our devices is of interest for several reasons. As stoichiometric Si_3N_4 is a high-stress material, high-frequency mechanical modes are expected, which should be accounted for when designing the devices. One potential problematic situation is where mechanical modes of the structure have frequencies comparable to the motional frequencies of the atoms in the traps. In this case, the mechanical motion could act as a source of parametric heating and decrease the coherence time of the trapped atoms[53]. The mechanical modes of the devices are also of interest to optomechanical coupling, which could open up new avenues for hybrid systems. This type of interaction has already been studied in the case of the 1D alligator waveguides [88].

Moreover, the thermal expansion may allow for thermal tuning of optical properties, such as the band gap edge frequency, by heating the substrate to thermally expand the photonic structure. This thermal tuning has been demonstrated for the 1D AWG system [27]. Here, they tune the band gap of a 1D PhC by heating the substrate, but the mechanism of the thermo-optomechanical tuning here is possibly driven by stress-induced separation of the two nano-beams of the structure as the substrate expands [88]. In a 2D PhC slab, the mechanism of coupling between

In our 2D system, the larger number of trapped atoms requires higher optical powers, which in turn necessitates a more thorough understanding of the thermo-mechanical properties of the system. The degree of heating caused by the optical tweezers, which are focused on the PhC, was particularly interesting. While the absorption in the Si_3N_4 film is low, the presence of a PhC can cause light to scatter into the underlying substrate, and understanding how this affects the mechanical properties is important. These measurements were carried out in the spring of 2022 with the help of undergraduate student Simon Lind. The waveguides were yet to be designed and fabricated, and direct measurement of the optomechanical coupling was not avail-

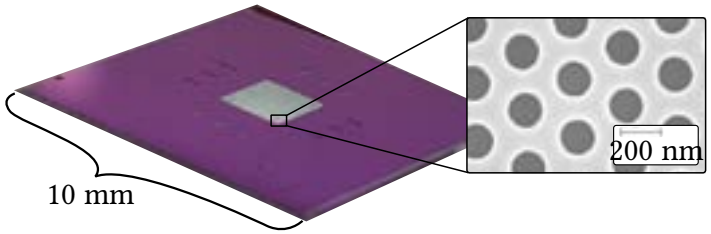

Figure 4.19: The device used for the thermo-mechanical measurements. A 10x10 mm square Si with a 2x2 mm square hole in the center. A 200 nm Si_3N_4 membrane is suspended over the hole. Sections of photonic crystals are defined at the edge of the Si_3N_4 membrane.

able. To measure the effects of thermal expansion, we instead measured the resonance frequency of a mechanical mode of the suspended membrane.

The device considered here is shown in fig. 4.19. It is one of the earlier devices we fabricated, where several photonic crystals are placed towards the edges of a 200 nm Si_3N_4 membrane. While heating the PhC with a laser, we measure the changes to the resonance frequency of the fundamental mechanical mode to estimate the absorption of the trapping tweezers. Similarly, suspended Si_3N_4 structures beams have been used as ultra-sensitive temperature sensors [89], and recently to measure the optical absorption of Si_3N_4 . We start here by reviewing the theory of a thermally driven mechanical oscillator following the same steps as in [90], and then describe the experimental setup used to measure the mechanical modes of the membrane before presenting the preliminary results of the optical stress-testing.

4.4.1 Thermally Driven Mechanical Oscillators

Our devices are suspended membranes, and what we are concerned with is the displacement of these membranes from their equilibrium position $\mathbf{u}(\mathbf{r}, t)$, which is the solution to the problem of linear elasticity for a given set of boundary conditions. By assuming separability of the solution, considering only the displacement along z, we expand the displacement field in a set of basis functions

$$u(x, y, t) = \mathbf{u}(\mathbf{r}, t)_z = \sum_n A_n \mathbf{u}_n(x, y) z_n(t) \hat{z}, \tag{4.4.1}$$

we can reduce the problem to that of a 1D harmonic oscillator. To simplify notation, we omit the reference to the mode number n, remembering that the motion of the membrane is a superposition of these modes.

The equation of motion for the amplitude z is that of a damped driven harmonic oscillator with damping rate Γ_m, resonant frequency ω_m, and effective mass m_{eff} and is given by

$$\frac{\partial^2}{\partial t^2}z(t) - \Gamma_m \frac{\partial}{\partial t}z(t) + \omega_m^2 z(t) = \frac{1}{m_{\text{eff}}}F. \tag{4.4.2}$$

We consider this in the Fourier domain, where the membrane displacement can be seen as the transduction of the driving force.

$$z(\omega) = \chi(\omega)_m F(\omega), \tag{4.4.3}$$

with

$$\chi(\omega)_m^{-1} = m_{\text{eff}}(\omega_m^2 - \omega^2 - i\Gamma_m\omega), \tag{4.4.4}$$

being the mechanical susceptibility.

Anticipating that we will be measuring the mechanical motion as a time signal, it is useful to consider the power spectral density (PSD)

$$S_{zz}(\omega) \equiv \lim_{T\to\infty} \frac{1}{T}|z_T(\omega)|^2, \tag{4.4.5}$$

which is defined in terms of the finite-time Fourier Transform of the time signal

$$z_T(\omega) = \int_{-T/2}^{T/2} z(t)e^{-i\omega t}d\omega, \tag{4.4.6}$$

in the limit where the time T goes to infinity. In other words, $z_T(\omega)$ is the Fourier transform of $z(t)$, filtered by a centered rectangular window of length T, corresponding to a finite measurement of $z(t)$.

The driving force that we consider here is a stochastic thermal force $F_{th}(t)$ that is the result of the random motion of the atoms in the membrane, in which case the PSD of the mechanical motion can be shown to be [91]

$$S_{zz}(\omega) = |\chi(\omega)_m|^2 S_{F_{th}F_{th}}(\omega) \approx \frac{\Gamma_m k_B T}{\omega_m^2 m_{\text{eff}}} \frac{1}{(\omega_m - \omega)^2 + (\Gamma_m/2)^2}. \tag{4.4.7}$$

We see that each mechanical mode will give rise to a Lorentzian lineshape in the PSD of the mechanical motion, with a full width at half maximum of Γ_m.

4.4.2 Mode Overlap with Probe Beam

The mechanical motion of the membrane is measured as the phase shift of a laser beam reflected off the membrane, and to measure the displacement efficiently, we must consider the spatial dependence of the modes of the displacement field. The spatial dependency is accounted for via the overlap integral of the mode shape and the electric field of the laser beam

$$\eta_n(x, y) = \int_A \mathbf{u}_n(x, y)\Phi(x - x', y - y')\mathrm{d}x'\mathrm{d}y', \tag{4.4.8}$$

Parameter	Symbol	Value	Source
Side length	L	2 mm	Own measurement
Thickness	d	(205.8 ± 0.1) nm	Own measurement
Refractive index	n	(2.0008 ± 0.0001)	Own measurement
Tensile stress	$\mathcal{T}$	1.1 GPa	Own measurement
Young's modulus	E	350 GPa	[92]
Poisson's ratio	ν	0.25	[93]
Thermal expansion Si_3N_4	$\alpha_{Si_3N_4}$	$2.35 \times 10^{-6}\,^{\circ}C^{-1}$	[94]
Thermal expansion Si	α_{Si}	$2.6 \times 10^{-6}\,^{\circ}C^{-1}$	[94]
Mass density	ρ	$3.1\,g\,cm^{-3}$	[39]
Fundamental mode frequency	ω_{11}	$2\pi\times$ 207 kHz	Calculated

Table 4.1: Parameters of the membrane used in the mechanical measurements.

Where $\Phi(x, y)$ is the normalized field profile of the laser in the plane of the membrane, A is the area of the membrane, and $\mathbf{u}_n(x', y')$ is the n^{th} mode in the expansioneq. (4.4.1). For a given position of the laser beam, this has to be evaluated for each membrane mode. The device measured here is a square membrane with the parameters shown in table 4.1

For a thin membrane, the displacement modes can be shown to be approximately [91]

$$u_{nm}(x, y, t) = z_{nm}(t)\sqrt{\frac{2}{L}}\sin\left(\frac{n\pi x}{L}\right)\sin\left(\frac{m\pi y}{L}\right), z_{nm}(t) = z_0\cos(\omega_{nm}t), \tag{4.4.9}$$

where mode frequencies are given by

$$\omega_{nm} = \frac{\pi}{L}\sqrt{\frac{2\mathcal{T}}{\rho}}\sqrt{\frac{n^2+m^2}{2}}. \tag{4.4.10}$$

For a Gaussian beam with a waist at the membrane surface $w(z_m)$, the overlap integral can be calculated analytically to beam

$$\eta_{nm}(x, y) = \exp\left[-\frac{w^2(z_m)}{8}\left(\frac{n^2\pi^2}{L_x^2}+\frac{m^2\pi^2}{L_y^2}\right)\right]\sin\left(\frac{n\pi x}{L_x}\right)\sin\left(\frac{m\pi y}{L_y}\right), \tag{4.4.11}$$

and we see that to measure ω_{11} with the highest sensitivity, the beam should be centered on the membrane. While this may be fairly obvious for simple geometry, these tools become important when considering more complex geometries in the future. For non-trivial geometries, the normal modes can be calculated numerically using FEM

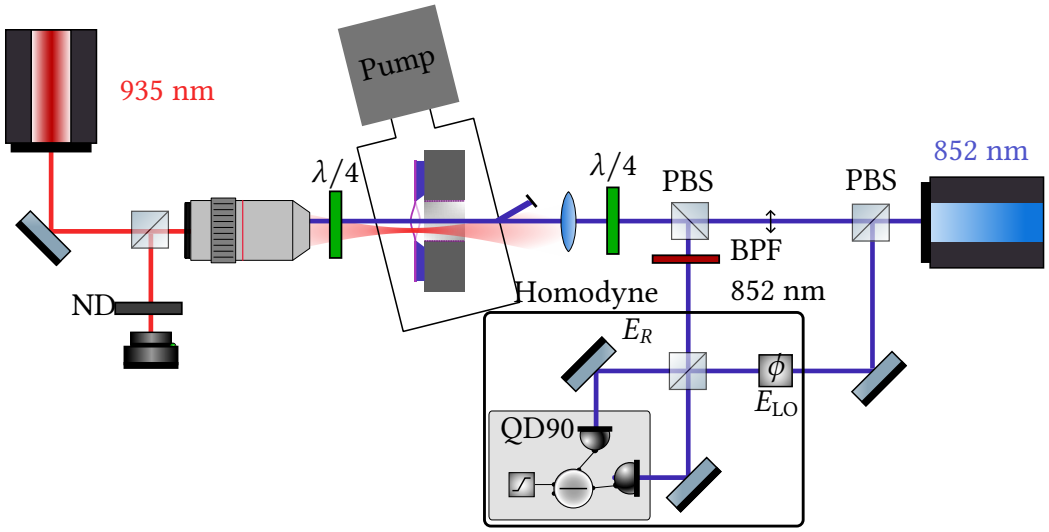

Figure 4.20: Schematic of the optical setup for thermomechanical measurements. The membrane is heated with a 935 nm laser focused down to 1.3 µm spot and the fundamental mode frequency is measured by a homodyne detection scheme. The vacuum chamber is angled to direct the reflection from the glass cell away from the detection path.

software such as COMSOL. In this case, the overlap integral can be calculated numerically by integrating the product of the mode shape and the laser beam's electric field profile over the membrane's area, and to measure a specific mode, the beam can be positioned to maximize η_{nm}. Alternatively, suppose the quantity of interest is only the PSD read out by a specific laser beam, not the mechanical modes themselves. In that case, the simulation can be turned around using the direct approach[95]. Here a driving-force of amplitude F_0 with the same spatial profile as the laser beam is used to drive the membrane at varying frequencies. The PSD of the mechanical motion can be calculated as

$$S_{zz}(\omega) = \frac{2k_B T}{\omega^2} \frac{W_{\text{diss}}}{F_0^2}, \tag{4.4.12}$$

W_{diss} is the total power dissipated from the structure's surface. For more details on implementing this in COMSOL, see [90].

4.4.3 Experimental Setup

To measure the motion of the membrane, we used a homodyne detection setup by measuring the phase of a beam of light reflected by the membrane. A schematic of the optical setup is shown in fig. 4.20. It is possible to measure the membrane motion from the amplitude of the reflected light by reflecting it at an angle and passing it

through a pinhole, but this turned out to be impractical due to our devices' low thin film reflectivity. The reflectivity of a dielectric film at normal incidence is [96]

$$R = \left| \frac{r_{12} + r_{23} e^{2ikd}}{1 + r_{12} r_{23} e^{2ikd}} \right|^2, \tag{4.4.13}$$

where

$$r_{ij} = \frac{n_i - n_j}{n_i + n_j}, \tag{4.4.14}$$

is the Fresnel reflectivity coefficient at an interface between two materials of refractive index n_i and n_j, $k = \frac{2\pi}{\lambda}$ and d is the thickness of the membrane.

The laser available at the time was an 852 nm Extended Cavity Diode Laser (ECDL) tunable by only a few nanometers, and the devices that we wanted to measure had a thickness of (205.8 ± 0.1) nm and refractive index of $n = (2.0008 \pm 0.0001)$ at 852 nm, measured with Ellipsometry. With these values, it gives a reflectivity of $R \approx 0.6\%$ from the surface of the membrane, i.e., a very weak signal, for which homodyne detection seemed the appropriate choice.

Homodyne Detection

The setup for homodyne detection is shown in fig. 4.21. The laser is split into two beams on a PBS, sending one arm to the membrane. The reflected beam is combined with the other arm on another PBS, and with a combination of another waveplate and PBS, the overlapped beam can be balanced on a photodetector. An optical band pass filter (BPF) removes the light from the heating laser. The balanced detector used here is a home-built model with two outputs, one for the difference signal and one with the same signal with a high pass filter (HPF). The unfiltered difference signal is sent to a Red Pitaya where PyrPL [97] is used to lock the phase between the reflected beam and the LO. The phase is controlled by a piezo mounted on a mirror in the reference arm. The signal from the ± 1 V signal from the Red Pitaya is amplified to ± 15 V in a home-built amplifier, which is sufficient to drive the piezo a full wavelength. The HP-filtered signal is low-pass filtered and sent to the input of a PicoScope 4262, where a periodogram of the signal is calculated. For more details on how to optimize the detected signal, see [90].

The field reflected from the membrane can be written as

$$E_R(t) = E_0 \alpha(t) e^{-i\omega t} \alpha(t) = \alpha_0 + \delta X(t) + i \delta Y(t), \tag{4.4.15}$$

where $\delta X(t)$ ($\delta Y(t)$) are the in (out of) phase fluctuations of the reflected field, which for small fluctuations $\alpha \gg \delta X, \delta Y$, corresponds to the amplitude (phase) fluctuations of the reflected field, and are referred to as the quadratures of the noise. The local oscillator field is

$$E_{\mathrm{LO}} = E_{0,\mathrm{LO}} e^{i(\omega t + \phi_{\mathrm{LO}})}, \tag{4.4.16}$$

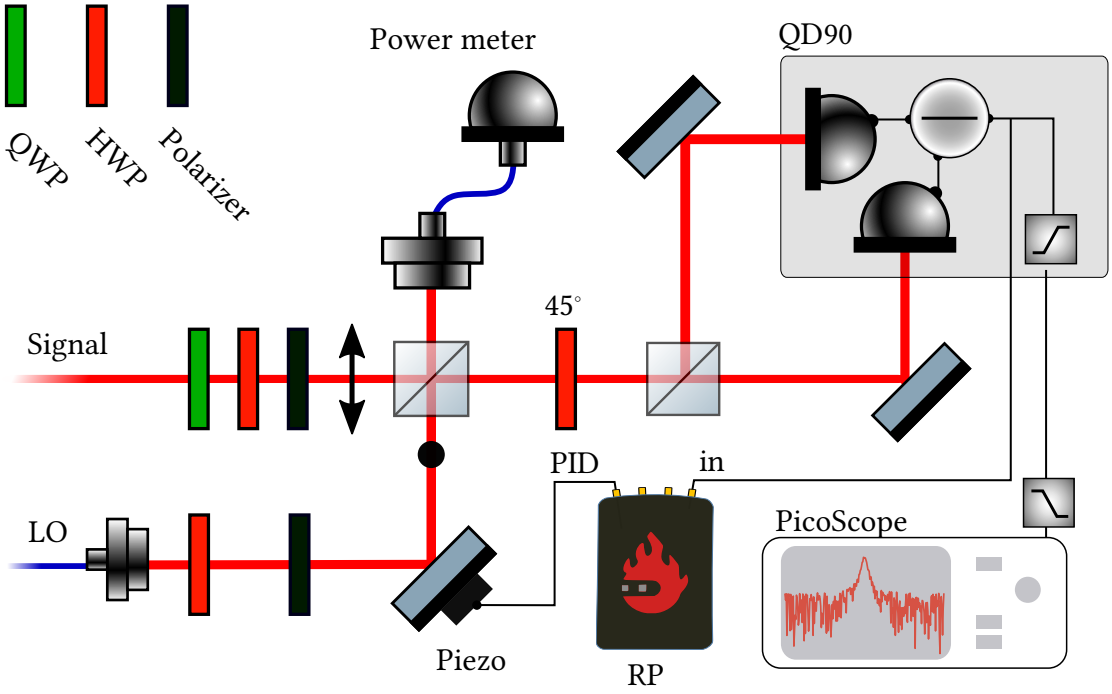

Figure 4.21: Implementation of Homodyne detection. The signal and LO are overlapped spatially on the first PBS, which is verified by coupling into the same fiber mode via the unused PBS port. The second PBS, in combination with a $\lambda/4$ plate is used to balance the signal on the two photodiodes. The DC difference signal is used to lock the phase of the LO, and the AC contains the PSD of the chosen quadrature. Adapted from [90]

and by balancing the power on the two detectors in fig. 4.21, the difference signal is given as

$$\frac{V}{G_D} = \left|\frac{i}{\sqrt{2}}E_R + \frac{1}{\sqrt{2}}E_{\mathrm{LO}}\right|^2 - \left|\frac{-i}{\sqrt{2}}E_{\mathrm{LO}} + \frac{1}{\sqrt{2}}E_R\right|^2 \tag{4.4.17}$$

$$= i\left(E_{\mathrm{LO}}E_R^* - E_{\mathrm{LO}}^*E_R\right) \tag{4.4.18}$$

$$= iE_{0,\mathrm{LO}}E_0\left(\alpha(t)e^{-i\phi_{\mathrm{LO}}} - \alpha^*(t)e^{i\phi_{\mathrm{LO}}}\right). \tag{4.4.19}$$

Here, $G_D(\omega)$ is the gain of the detector, which in general is frequency dependent but, in our case, can safely be considered a constant as ω_{11} is well within the bandwidth of our electronics. When the LO phase is locked to $\phi_{\mathrm{LO}} = 0$, $V(t) \propto \delta Y(t)$, and we can measure the phase of the light reflected from the membrane. The phase of the reflected light is proportional to the out-of-plane motion of the membrane, and the PSD of the measured voltage is related to the displacement PSD of the membrane

$$S_{VV} \propto S_{zz}. \tag{4.4.20}$$

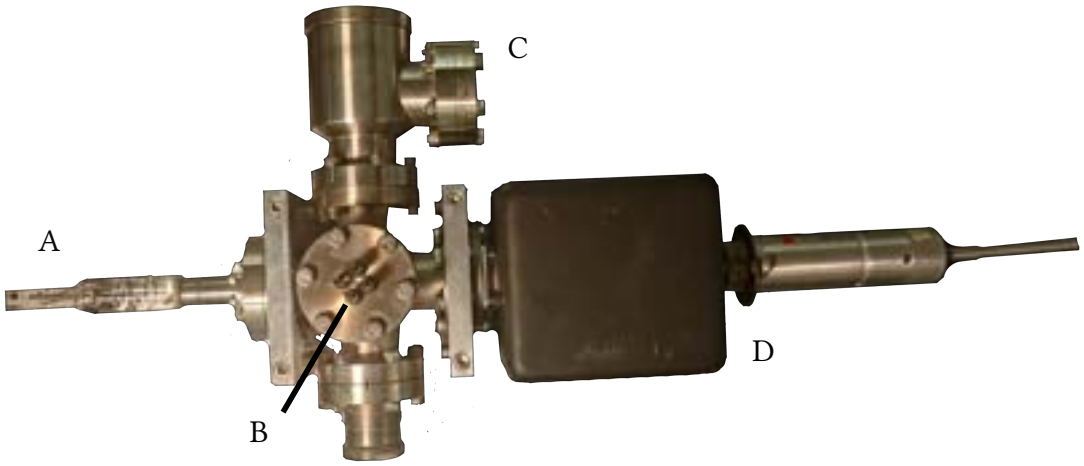

Figure 4.22: The vacuum chamber used for the mechanical measurements, seen top down. (**A**) The science chamber is a rectangular glass cell with optical access from all sides. (**B**) the central chamber has a Cs dispenser. (**C**) Valve and connector for the vacuum pump. (**D**) Ion pump.

Vacuum Chamber

The membrane was mounted in a vacuum chamber to avoid the effects of air damping, in part to avoid the effects of air convection, and in part to enable us to test the effects of Cs sticking to the surface in the future. The vacuum chamber is shown in fig. 4.22. The chamber is a glass science cell connected to a Cs dispenser in the center and a valve and connector for the vacuum pump. The chamber is pumped in three stages: a roughing pump, a turbo pump, and an ion pump. The pressure cannot be measured directly but can be extrapolated from the ion pump current. The pressure is typically in the range of 1×10^{-5} mbar to 1×10^{-6} mbar.

Because the reflectivity of the membrane was so low, the sample had to be rotated with respect to the glass windows of the vacuum chamber to deflect the reflections from the glass. The chip was mounted to a small piece of metal with a hole through the center, fig. 4.23, and fortunately, we chose to use a magnetic metal for the sample holder, allowing us to turn the sample relative to the glass sides of the chamber without breaking vacuum.

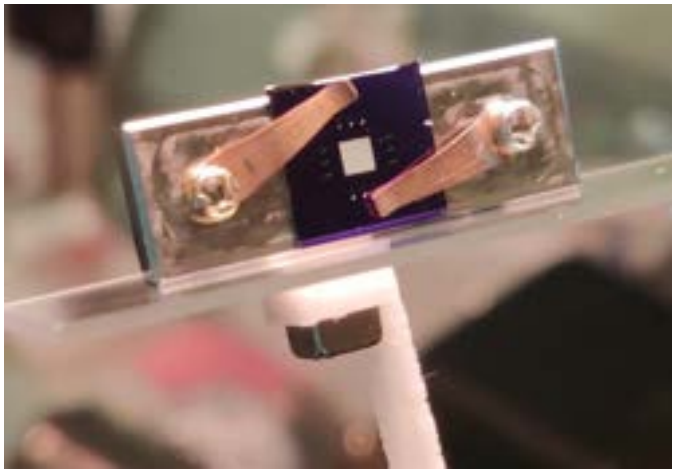

Figure 4.23: The sample holder used to mount the chip in the vacuum chamber. The chip is mounted on the metal piece and held with two leaf springs. The metal piece is held in place by a magnet placed on the bottom of the chamber. The chip holder is placed on a glass slide to verify that the magnet can maneuver the sample holder. The magnet is held in a 3D-printed holder to avoid damage to the glass.

Heating Laser

To heat the membrane, we used a 935 nm laser[13]. The heating laser is focused to a beam diameter comparable to that of the trapping laser to mimic the situation in the atomic experiment, $w_0 \approx 1\,\mu m$. The laser beam is expanded to a $1/e^2$ radius of 2.4 mm, which fills the back-aperture of the 20x microscope objective [14] and focuses to a spot size of 1.3 µm. To inspect the positioning of the heating laser on the membrane, a camera is placed in the beam path using a beam splitter, using ND filters to attenuate the reflected heating beam.

The microscope objective introduced another complication regarding the homodyne detection setup. Because of the low reflectivity of the membrane, the reflection from the microscope objective also had to be suppressed so as not to drown out the signal from the membrane. By placing a $\lambda/4$ waveplate in the beam path, the reflection of the 852 nm light from the objective in the detection path was decreased sufficiently.

4.4.4 Data Collection and Analysis

With the homodyne detection set up locked to maximize the detection of the phase quadrature, the time signal is recorded on the PicoScope. The probe beam is positioned at the center of the membrane, where the amplitude of the fundamental mechanical

[13]Toptica TAPro
[14]Mitotoyo M Plan Apo NIR 20X

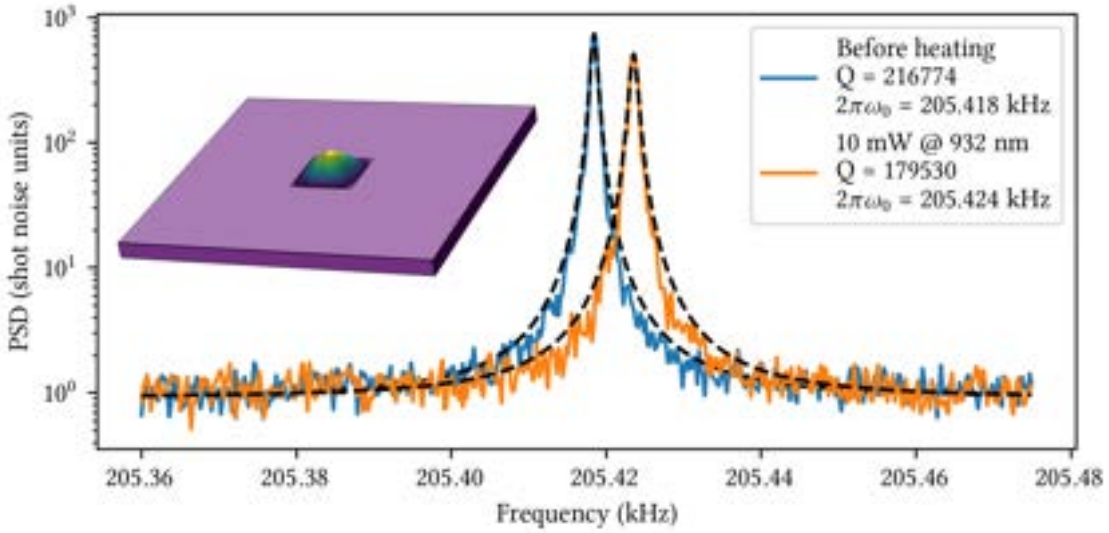

Figure 4.24: PSD of the fundamental mechanical mode of the membrane. The simulated displacement profile of the mode is shown in the inset, where only the released Si_3N_4 window is moving, with the amplitude of the displacement being exaggerated. Hitting the membrane with a laser at 935 nm causes the central frequency to increase. The broadening of the mechanical mode is at least in part attributed to a slow drift during the measurement.

mode is the largest. The PSD is calculated from the Discrete Fourier Transform of the time signal s_n

$$\mathrm{DFT}[s](m) = \sum_{n=1}^{N} s_n e^{-2\pi i m n/N}, \tag{4.4.21}$$

where N is the number of samples in the time signal, and m is the frequency index running from 0 to $N-1$. The data is sampled at a sampling rate of F_s, which for the PicoScope 4262 is 10 MHz. The width of the frequency bins called the resolution bandwidth (RBW), is then given as F_s/N, and it is thus limited by the number of samples in the time signal. The PSD is approximated by the Periodogram, which is defined as

$$P_s(m) = \frac{1}{NF_s}|\mathrm{DFT}[s](m)|^2, \tag{4.4.22}$$

which converges to the PSD of s_n as $T = N/F_s$ approaches infinity.

With the heating laser on the released section of the membrane, an increase in resonant frequency was observed Figure 4.24. The difference in thermal expansion of Si and Si_3N_4 can explain the positive frequency shift for an increase in temperature. If the Si frame expands more than the Si_3N_4 membrane, the stress increases, and so does the resonance frequency of the mechanical modes according to eq. (4.4.10).

For a solid slab of Si with a Si_3N_4 membrane on top, the change in tensile stress in the Si_3N_4 layer induced by the differential thermal expansion from a temperature change of ΔT is

$$\Delta\mathcal{T}(\Delta T) = \frac{E}{1-\nu}\left(\alpha_{\mathrm{Si}} - \alpha_{\mathrm{Si_3N_4}}\right)\Delta T, \tag{4.4.23}$$

where E and ν are Young's modulus and Poisson's ratio for Si_3N_4 respectively, and $\alpha_{\mathrm{Si}}(\alpha_{\mathrm{Si_3N_4}})$ is the coefficient of thermal expansion for Si(Si_3N_4). Together with eq. (4.4.10), we can estimate the change in temperature from a change in the frequency of the fundamental mechanical mode. To first order in ΔT

$$\frac{d\omega_{11}}{dT} \approx \frac{\pi E(\alpha_{\mathrm{Si}} - \alpha_{\mathrm{Si_3N_4}})}{2L(1-\nu)}\sqrt{\frac{2}{\mathcal{T}\rho}}\Delta T \approx 2\pi \times 11\,\mathrm{Hz}\,^{\circ}\mathrm{C}^{-1}. \tag{4.4.24}$$

This is an approximate value, as it depends on $\alpha_{\mathrm{Si_3N_4}}$, which can vary depending on the process parameters of the deposition. We note that if the temperature of the system could be measured or controlled via a different mechanism, this would enable us to measure $\alpha_{\mathrm{Si_3N_4}}$, as α_{Si} is provided by the manufacturer.

4.4.5 Tracking the Mechanical Mode

Ultimately, we want to determine whether the change in resonance frequency caused by the heating laser was reversible. We thought it would be interesting to see how the frequency changes over time during heating and cooling. We determined the resonance frequency in the stationary case by fitting a Lorentzian function to the spectrum. This approach proved problematic when tracking changes to the resonance frequency in real time. As Γ_m is on the order of Hz we require sub-Hz RBW to track the change in ω_m accurately ω_m. The RBW is the inverse of the acquisition time, and thus, to obtain a frequency resolution of below 1 Hz, the spectrum has to be recorded for $T > 1$ s. On the other hand, one needs to average over multiple traces to increase the signal-to-noise ratio (SNR) to a point where the mechanical peak can be detected above the background, a technique often referred to as the Welch method [98], where a time signal is chopped into shorter signals that are then averaged. There is a fundamental trade-off between spectral resolution and SNR; to increase the spectral resolution, one should work with long-time traces, but to increase the SNR, we want to average over as many traces as possible. For a stationary process, this is solved by simply taking many sufficiently long time traces, but when measuring a chirped signal, the averaging is no longer valid. Here, we are satisfied in measuring changes in the resonance frequency on a timescale of seconds, and we find that an acquisition time of $T = 200$ ms gives sufficient SNR to discern the mechanical peak. When tracking the peak frequency, we found that using the centroid frequency f_c was the most robust way to track the frequency. It is defined as

$$f_c = \frac{\sum f_i \cdot A_i}{\sum A_i}, \tag{4.4.25}$$

where A_i is the amplitude of the signal at f_i, where the sum runs over n points around the maximum of the spectrum in a region around the previously measured frequency.

4.4.6 Heating Transients

When the membrane is heated with the laser, we observe a transient shift in ω_{11} happening at two distinct timescales. Initially the slow timescale was suspected of being signs of permanent damage to the chip, but after waiting for a longer time ω_{11} returns close to the initial value.

The heating transients can be explained by a simple lumped element heating model, where the rate of change of thermal energy of an object of mass m and heat capacity c is

$$mc\frac{dT}{dt} = Q - hA(T(t) - T_{\text{env}}), \tag{4.4.26}$$

where Q is a constant source of thermal energy, T is the temperature of the object, T_{env} is the temperature of the environment that the object is coupled to through a contact area A with a heat transfer coefficient h. By defining a characteristic time $\tau = mc/hA$ and an effective heating temperature ΔT_{heat} it can be written as

$$\frac{dT}{dt} = \frac{\Delta T_{\text{heat}} + T_{\text{env}} - T(t)}{\tau}. \tag{4.4.27}$$

For this specific system, T is the temperature of the membrane at thermal equilibrium with the metal block, as the transient time of the chip is much faster than what we can measure here. Here, the environment is the glass cell of the vacuum chamber T_{gc}, which is thermally coupled to the sample and the laboratory temperature T_{lab}. This gives a set of two coupled differential equations.

$$\frac{dT}{dt} = \frac{\Delta T_{\text{heat}} + T_{\text{gc}}(t) - T(t)}{\tau} \tag{4.4.28}$$

$$\frac{dT_{\text{gc}}}{dt} = \frac{\gamma}{\tau_{\text{gc}}}\left(T(t) - T_{\text{gc}}(t)\right) - \frac{T_{\text{gc}}(t) - T_{\text{lab}}}{\tau_{\text{gc}}}, \tag{4.4.29}$$

where $\gamma = \frac{hA}{h_{\text{gc}}A_{\text{gc}}}$ is the ratio of the heat transfer coefficients between the chip/sample holder to the glass cell, and that of the glass cell to the lab.

In fig. 4.25, we see the tracked frequency shift for 24 consecutive heating and cooling cycles with moderate (10 mW) optical power. By fitting exponentials to the slow and fast time scale separately and using these as parameters in a numerical solution to eq. (4.4.28), we see excellent qualitative agreement.

This means that to determine whether a change in ω_{11} is permanent, it is necessary to wait for the entire system to reach thermal equilibrium.

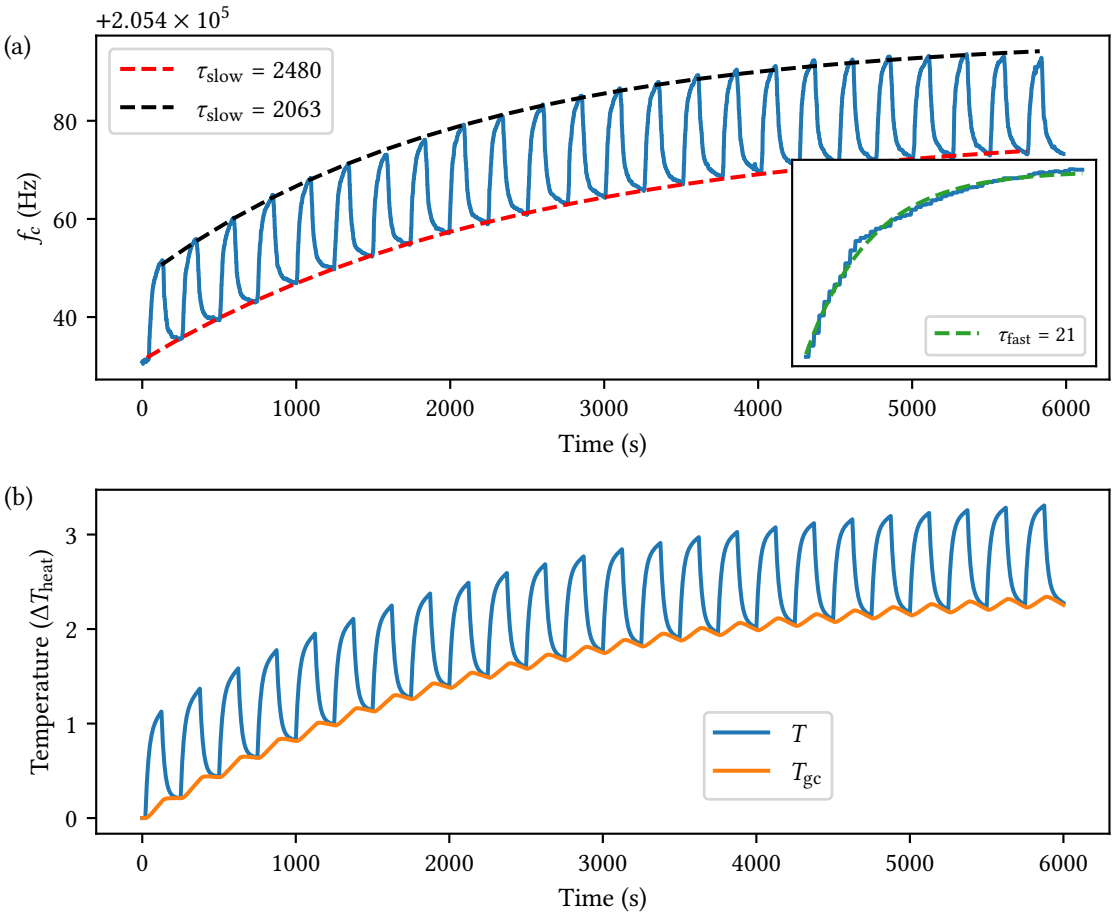

Figure 4.25: (a) Changes in mechanical frequency for 24 cycles of heating cooling. Time constants for the transient are fitted at the end and start of the heating cycle. The inset shows a fit to one of the short transient times. (b) Heat dissipation model with $\tau_{fast} = 21$s, $\tau_{slow} = 2271$s and $\alpha = 5$

At the time, the highest optical power available was 150 mW, and using this we observed a steady-state frequency shift of 210 Hz, corresponding to a temperature change of $\Delta T \approx 20\,^{\circ}$C. This rather modest temperature shift was fully reversible.

With the same optical power, we observed that when the laser is focused on a region containing a PhC, the change in frequency is appreciably larger. This is most likely caused by increased scattering by the PhC into the Si substrate.

The conclusion to this is that at least for the full 2D membrane, 150 mW of optical power focused onto a Si_3N_4 membrane with a PhC is not enough to permanently alter the fundamental mode frequency ω_{11} appreciably. This is promising, but as the final design will have both a different mechanical mode structure and different thermal

dissipation channels, these results are preliminary.

The capability of measuring and tracking the mechanical mode frequencies of our devices is a powerful tool to have, especially when combined with optical access to the in-plane modes. It allows us to measure optomechanical and thermo-optomechanical coupling in our design and will help us determine thermal tuning rates of the band gap frequency. With the recently acquired Ti:Saph laser, optical powers of several W are now available, and it may be possible to determine the limits of these structures using this setup.

Chapter 5

Summary and Outlook

This thesis has documented the establishment of a comprehensive framework for the design, fabrication, and characterization of suspended Si_3N_4 photonic crystal devices for integration with cold atom systems.

The design of suspended Si_3N_4 PhC membranes and waveguides using both analytical models and numerical simulation tools has been demonstrated. We designed tether structures that minimize scattering and allow for thermal dissipation to the substrate, and couplers for efficient coupling to either a fiber or a free space mode. We simulated the dispersion for the 2D PhC, and used FDTD simulations to calculate key FOMs, and estimate fabrication tolerances for our target design parameters.

A fabrication process for suspended Si_3N_4 photonic crystal devices has been established, utilizing a combination of dry and wet etching, metal deposition, and lithography techniques. This process has been successfully integrated with the design files from the framework, enabling the fabrication of photonic waveguides and two-dimensional photonic crystal slabs. Additionally, using a chromium hard mask for etching has enabled the achievement of high sidewall verticality in structures with large aspect ratios.

Several characterization tools have been implemented to evaluate the optical properties of the fabricated devices. Transmission spectra have been successfully measured for fabricated waveguides, and SEM has been employed to assess the quality of the fabricated structures. A near-field optical microscope has also been established, though its application to photonic crystal devices remains ongoing. A detailed analysis was conducted to assess the accuracy and limitations of the SEM-based evaluations.

The work presented in this thesis provides a solid foundation for future advancements in integrating cold atoms with photonic crystal devices. The design framework can be further extended to include more complex device configurations, which would allow for exploring additional applications and device functionalities.

Optimization of the fabrication process will be essential for improving device performance, particularly in reducing defects and enhancing the quality of sidewall and

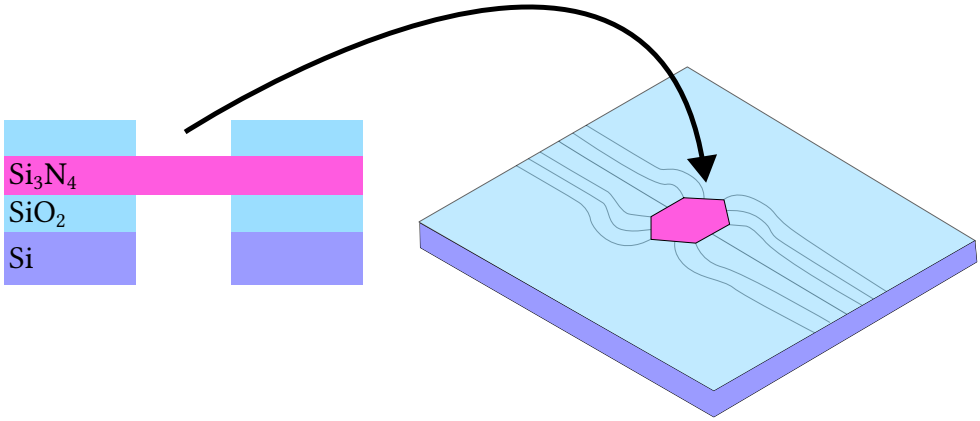

Figure 5.1: Conceptual drawing of potential alternative fabrication platform. A hexagonal PhC (indicated by a hexagonal opening) Si_3N_4 device is clad in SiO_2 everywhere except at the location of the PhC, and the waveguides are now fully embedded in SiO_2. The waveguides provide bidirectional optical access to the high symmetry directions in the PhC.

feature definition. Continued refinement of etching protocols and lithography techniques will likely result in higher device yields and better control over critical dimensions.

The characterization tools established in this thesis offer significant potential for future studies. The near-field optical microscope, once fully operational, will provide critical insights into the near-field properties of photonic crystals. Further, the existing optical and SEM-based characterizations can be expanded to probe more intricate device behaviors, such as modal properties and loss mechanisms.

An idea that emerged towards the end of the project was that of switching to a different fabrication platform, as illustrated in fig. 5.1. Here, the Si_3N_4 layer is clad in a layer of SiO_2 that is only opened at the center of the device where the PhC structure is located. There are a few benefits of doing so. Waveguide design is simpler as we no longer have to tether the devices or worry about thermal dissipation, and routing should be simpler as the effects of anisotropic etching discussed in section 3.6 no longer apply. Scattering losses from the waveguides are reduced because of the lower index contrast, and the release of the membrane should be more robust, as it is no longer necessary to have thin waveguides suspended over a large window.

Bibliography

[1] Q. f. Life. *Quantum for Life*. en. Publisher: University of Copenhagen. July 2021. URL: https://quantumforlife.ku.dk/ (visited on 09/26/2024).

[2] B. Keimer et al. "From quantum matter to high-temperature superconductivity in copper oxides". en. In: *Nature* 518.7538 (Feb. 2015). Publisher: Nature Publishing Group, pp. 179–186. ISSN: 1476-4687. DOI: 10.1038/nature14165. URL: https://www.nature.com/articles/nature14165 (visited on 09/04/2024).

[3] D. N. Basov, R. D. Averitt, and D. Hsieh. "Towards properties on demand in quantum materials". en. In: *Nature Materials* 16.11 (Nov. 2017). Publisher: Nature Publishing Group, pp. 1077–1088. ISSN: 1476-4660. DOI: 10.1038/nmat5017. URL: https://www.nature.com/articles/nmat5017 (visited on 09/04/2024).

[4] B. Fauseweh. "Quantum many-body simulations on digital quantum computers: State-of-the-art and future challenges". en. In: *Nature Communications* 15.1 (Mar. 2024). Publisher: Nature Publishing Group, p. 2123. ISSN: 2041-1723. DOI: 10.1038/s41467-024-46402-9. URL: https://www.nature.com/articles/s41467-024-46402-9 (visited on 09/04/2024).

[5] J. Bermejo-Vega et al. "Architectures for Quantum Simulation Showing a Quantum Speedup". en. In: *Physical Review X* 8.2 (Apr. 2018), p. 021010. ISSN: 2160-3308. DOI: 10.1103/PhysRevX.8.021010. URL: https://link.aps.org/doi/10.1103/PhysRevX.8.021010 (visited on 09/04/2024).

[6] R. Trivedi, A. Franco Rubio, and J. I. Cirac. "Quantum advantage and stability to errors in analogue quantum simulators". en. In: *Nature Communications* 15.1 (Aug. 2024). Publisher: Nature Publishing Group, p. 6507. ISSN: 2041-1723. DOI: 10.1038/s41467-024-50750-x. URL: https://www.nature.com/articles/s41467-024-50750-x (visited on 09/24/2024).

[7] P. De Vries, D. V. Van Coevorden, and A. Lagendijk. "Point scatterers for classical waves". en. In: *Reviews of Modern Physics* 70.2 (Apr. 1998), pp. 447–466. ISSN: 0034-6861, 1539-0756. DOI: 10.1103/RevModPhys.70.447. URL: https://link.aps.org/doi/10.1103/RevModPhys.70.447 (visited on 09/04/2024).

[8] M. K. Tey et al. “Strong interaction between light and a single trapped atom without the need for a cavity”. en. In: *Nature Physics* 4.12 (Dec. 2008). Publisher: Nature Publishing Group, pp. 924–927. ISSN: 1745-2481. DOI: 10.1038/nphys1096. URL: https://www.nature.com/articles/nphys1096 (visited on 09/24/2024).

[9] A. Reiserer and G. Rempe. “Cavity-based quantum networks with single atoms and optical photons”. en. In: *Reviews of Modern Physics* 87.4 (Dec. 2015), pp. 1379–1418. ISSN: 0034-6861, 1539-0756. DOI: 10.1103/RevModPhys.87.1379. URL: https://link.aps.org/doi/10.1103/RevModPhys.87.1379 (visited on 09/08/2024).

[10] R. Miller et al. “Trapped atoms in cavity QED: coupling quantized light and matter”. en. In: *Journal of Physics B: Atomic, Molecular and Optical Physics* 38.9 (Apr. 2005), S551. ISSN: 0953-4075. DOI: 10.1088/0953-4075/38/9/007. URL: https://dx.doi.org/10.1088/0953-4075/38/9/007 (visited on 09/08/2024).

[11] E. M. Purcell. “Spontaneous Emission Probabilities at Radio Frequencies”. In: *Physical Review* 69 (1946), p. 681. DOI: 10.1103/PhysRev.69.674.2. URL: http://link.aps.org/doi/10.1103/PhysRev.69.674.2.

[12] M. Albrechtsen et al. “Nanometer-scale photon confinement in topology-optimized dielectric cavities”. en. In: *Nature Communications* 13.1 (Oct. 2022). Publisher: Nature Publishing Group, p. 6281. ISSN: 2041-1723. DOI: 10.1038/s41467-022-33874-w. URL: https://www.nature.com/articles/s41467-022-33874-w (visited on 09/09/2024).

[13] J. D. Joannopoulos et al. *Photonic Crystals: Molding the Flow of Light - Second Edition*. REV - Revised, 2. Princeton University Press, 2008. ISBN: 978-0-691-12456-8. DOI: 10.2307/j.ctvcm4gz9. URL: https://www.jstor.org/stable/j.ctvcm4gz9 (visited on 09/09/2024).

[14] L. Novotny and B. Hecht. *Principles of Nano-Optics*. Cambridge: Cambridge University Press, 2006. DOI: 10.1017/CBO9780511813535. URL: https://www.cambridge.org/core/books/principles-of-nanooptics/EAA3E0D04179A7252088E27483C4ACC1 (visited on 08/21/2024).

[15] P. Lodahl, S. Mahmoodian, and S. Stobbe. “Interfacing single photons and single quantum dots with photonic nanostructures”. In: *Reviews of Modern Physics* 87.2 (May 2015). Number of pages: 54 Publisher: American Physical Society, pp. 347–400. DOI: 10.1103/RevModPhys.87.347. URL: https://link.aps.org/doi/10.1103/RevModPhys.87.347.

[16] A. Sipahigil et al. “An integrated diamond nanophotonics platform for quantum-optical networks”. In: *Science* 354.6314 (2016). tex.eprint: https://www.science.org/doi/pdf/10.1126/science.aah6875, pp. 847–850. DOI: 10.1126/science.aah6875. URL: https://www.science.org/doi/abs/10.1126/science.aah6875.

[17] M. Arcari et al. “Near-unity coupling efficiency of a quantum emitter to a photonic-crystal waveguide”. en. In: *Physical Review Letters* 113.9 (Aug. 2014). arXiv:1402.2081 [physics, physics:quant-ph], p. 093603. ISSN: 0031-9007, 1079-7114. DOI: 10.1103/PhysRevLett.113.093603. URL: http://arxiv.org/abs/1402.2081 (visited on 09/14/2024).

[18] L. Scarpelli et al. “99% beta factor and directional coupling of quantum dots to fast light in photonic crystal waveguides determined by spectral imaging”. In: *Physical Review B* 100.3 (July 2019). Publisher: American Physical Society, p. 035311. DOI: 10.1103/PhysRevB.100.035311. URL: https://link.aps.org/doi/10.1103/PhysRevB.100.035311 (visited on 09/14/2024).

[19] A. Asenjo-Garcia et al. “Atom-light interactions in quasi-one-dimensional nanostructures: A Green’s-function perspective”. en. In: *Physical Review A* 95.3 (Mar. 2017), p. 033818. ISSN: 2469-9926, 2469-9934. DOI: 10.1103/PhysRevA.95.033818. URL: https://link.aps.org/doi/10.1103/PhysRevA.95.033818 (visited on 09/24/2024).

[20] T. Gruner and D.-G. Welsch. “Quantum-optical input-output relations for dispersive and lossy multilayer dielectric plates”. In: *Physical Review A* 54.2 (Aug. 1996). Publisher: American Physical Society, pp. 1661–1677. DOI: 10.1103/PhysRevA.54.1661. URL: https://link.aps.org/doi/10.1103/PhysRevA.54.1661 (visited on 09/30/2024).

[21] M. Wubs, L. G. Suttorp, and A. Lagendijk. “Multiple-scattering approach to interatomic interactions and superradiance in inhomogeneous dielectrics”. In: *Physical Review A* 70.5 (Nov. 2004). Publisher: American Physical Society, p. 053823. DOI: 10.1103/PhysRevA.70.053823. URL: https://link.aps.org/doi/10.1103/PhysRevA.70.053823 (visited on 09/30/2024).

[22] D. E. Chang et al. “Colloquium: Quantum matter built from nanoscopic lattices of atoms and photons”. In: *Reviews of Modern Physics* 90.3 (Aug. 2018), p. 031002. DOI: 10.1103/RevModPhys.90.031002. URL: https://link.aps.org/doi/10.1103/RevModPhys.90.031002 (visited on 03/07/2024).

[23] J. S. Douglas et al. “Quantum many-body models with cold atoms coupled to photonic crystals”. en. In: *Nature Photonics* 9.5 (May 2015). Publisher: Nature Publishing Group, pp. 326–331. ISSN: 1749-4893. DOI: 10.1038/nphoton.2015.57. URL: https://www.nature.com/articles/nphoton.2015.57 (visited on 09/09/2024).

[24] A. Goban et al. “Superradiance for Atoms Trapped along a Photonic Crystal Waveguide”. en. In: *Physical Review Letters* 115.6 (Aug. 2015), p. 063601. ISSN: 0031-9007, 1079-7114. DOI: 10.1103/PhysRevLett.115.063601. URL: https://link.aps.org/doi/10.1103/PhysRevLett.115.063601 (visited on 05/01/2024).

[25] J. D. Thompson et al. “Coupling a Single Trapped Atom to a Nanoscale Optical Cavity”. In: *Science* 340.6137 (June 2013). Publisher: American Association for the Advancement of Science, pp. 1202–1205. DOI: 10.1126/science.1237125. URL: https://www.science.org/doi/10.1126/science.1237125 (visited on 09/09/2024).

[26] A. Goban et al. “Atom–light interactions in photonic crystals”. en. In: *Nature Communications* 5.1 (May 2014). Publisher: Nature Publishing Group, p. 3808. ISSN: 2041-1723. DOI: 10.1038/ncomms4808. URL: https://www.nature.com/articles/ncomms4808 (visited on 09/08/2024).

[27] J. D. Hood et al. “Atom-atom interactions around the band edge of a photonic crystal waveguide”. en. In: *Proceedings of the National Academy of Sciences* 113.38 (Sept. 2016), pp. 10507–10512. ISSN: 0027-8424, 1091-6490. DOI: 10.1073/pnas.1603788113. URL: http://arxiv.org/abs/1603.02771 (visited on 05/01/2024).

[28] S. P. Yu et al. “Two-dimensional photonic crystals for engineering atom–light interactions”. In: *Proceedings of the National Academy of Sciences of the United States of America* 116.26 (2019), pp. 12743–12751. ISSN: 10916490. DOI: 10.1073/pnas.1822110116. URL: www.pnas.org/cgi/doi/10.1073/pnas.1822110116.

[29] M. E. Kim et al. “Trapping single atoms on a nanophotonic circuit with configurable tweezer lattices”. In: *Nature Communications* 10.1 (2019). ISSN: 20411723. DOI: 10.1038/s41467-019-09635-7. URL: http://dx.doi.org/10.1038/s41467-019-09635-7.

[30] H. L. Sørensen et al. “Coherent Backscattering of Light Off One-Dimensional Atomic Strings”. In: *Physical Review Letters* 117.13 (Sept. 2016). Publisher: American Physical Society, p. 133604. DOI: 10.1103/PhysRevLett.117.133604. URL: https://link.aps.org/doi/10.1103/PhysRevLett.117.133604 (visited on 09/07/2024).

[31] X. Zhou et al. “Subwavelength precision optical guiding for trapped atoms coupled to a nanophotonic resonator”. In: (2021). URL: http://arxiv.org/abs/2111.01119.

[32] J.-B. Béguin et al. “Advanced apparatus for the integration of nanophotonics and cold atoms”. In: *Optica* 7.1 (2020), p. 1. ISSN: 23342536. DOI: 10.1364/optica.7.000001.

[33] S.-P. Yu. “Nano-Photonic Platform for Atom-Light Interaction”. en. phd. California Institute of Technology, 2017. DOI: 10.7907/Z9668B7F. URL: https://resolver.caltech.edu/CaltechTHESIS:06022017-134307910 (visited on 04/04/2024).

[34] J. Witzens, M. Lončar, and A. Scherer. “Self-collimation in planar photonic crystals”. In: *Selected Topics in Quantum Electronics, IEEE Journal ofSelected Topics in Quantum Electronics, IEEE Journal of* 8 (2002). ISBN: 1077-260X, pp. 1246–1257.

[35] J. A. Muniz Silva. "Nanoscopic Atomic Lattices with Light-Mediated Interactions". en. phd. California Institute of Technology, 2017. DOI: 10.7907/Z9W66HTK. URL: https://resolver.caltech.edu/CaltechTHESIS:05152017-144541997 (visited on 09/10/2024).

[36] S. G. Johnson and J. D. Joannopoulos. "Block-iterative frequency-domain methods for Maxwell's equations in a planewave basis". EN. In: *Optics Express* 8.3 (Jan. 2001). Publisher: Optica Publishing Group, pp. 173–190. ISSN: 1094-4087. DOI: 10.1364/OE.8.000173. URL: https://opg.optica.org/oe/abstract.cfm?uri=oe-8-3-173 (visited on 09/11/2024).

[37] J. D. Cohen, S. M. Meenehan, and O. Painter. "Optical coupling to nanoscale optomechanical cavities for near quantum-limited motion transduction". en. In: *Optics Express* 21.9 (May 2013), p. 11227. ISSN: 1094-4087. DOI: 10.1364/OE.21.011227. URL: https://opg.optica.org/oe/abstract.cfm?uri=oe-21-9-11227 (visited on 09/03/2024).

[38] A. C. McClung. "Photonic Crystal Waveguides for Integration into an Atomic Physics Experiment". en. phd. California Institute of Technology, 2017. DOI: 10.7907/Z9154F3G. URL: https://resolver.caltech.edu/CaltechTHESIS:06082017-134311664 (visited on 04/04/2024).

[39] H. O. Pierson. *Handbook of chemical vapor deposition*. eng. 2nd ed. Materials science and process technology series. Norwich, NY: Noyes Publications, 1999. ISBN: 978-0-8155-1432-9.

[40] X. Luan et al. "The Integration of Photonic Crystal Waveguides with Atom Arrays in Optical Tweezers". en. In: *Advanced Quantum Technologies* 3.11 (2020). _eprint: https://onlinelibrary.wiley.com/doi/pdf/10.1002/qute.202000008, p. 2000008. ISSN: 2511-9044. DOI: 10.1002/qute.202000008. URL: https://onlinelibrary.wiley.com/doi/abs/10.1002/qute.202000008 (visited on 09/07/2024).

[41] C. A. Rosiek. "Topological Insulators and Topology Optimization in Nanophotonics". en. In: ().

[42] M. Gehl et al. "Characterization of suspended membrane waveguides towards a photonic atom trap integrated platform". en. In: *Optics Express* 29.9 (Apr. 2021), p. 13129. ISSN: 1094-4087. DOI: 10.1364/OE.418986. URL: https://opg.optica.org/abstract.cfm?URI=oe-29-9-13129 (visited on 07/31/2024).

[43] D. Feng et al. *Self-referencing photothermal common-path interferometry to measure absorption of Si3N4 membranes for laser-light sails*. Apr. 2024. DOI: 10.48550/arXiv.2404.04449. URL: http://arxiv.org/abs/2404.04449 (visited on 08/01/2024).

[44] F. P. Payne and J. P. R. Lacey. "A theoretical analysis of scattering loss from planar optical waveguides". en. In: *Optical and Quantum Electronics* 26.10 (Oct. 1994), pp. 977–986. ISSN: 1572-817X. DOI: 10.1007/BF00708339. URL: https://doi.org/10.1007/BF00708339 (visited on 08/09/2024).

[45] C. J. R. Sheppard. "Approximate calculation of the reflection coefficient from a stratified medium". en. In: *Pure and Applied Optics: Journal of the European Optical Society Part A* 4.5 (Sept. 1995), p. 665. ISSN: 0963-9659. DOI: 10.1088/0963-9659/4/5/018. URL: https://dx.doi.org/10.1088/0963-9659/4/5/018 (visited on 07/31/2024).

[46] Y.-W. Hu et al. "Characterization of Low Loss Waveguides Using Bragg Gratings". In: *IEEE Journal of Selected Topics in Quantum Electronics* 24.4 (July 2018), pp. 1–8. ISSN: 1558-4542. DOI: 10.1109/JSTQE.2018.2827663. URL: https://ieeexplore.ieee.org/document/8338360/?arnumber=8338360 (visited on 07/31/2024).

[47] D. R. Paschotta. *finesse*. en. URL: https://www.rp-photonics.com/finesse.html (visited on 07/31/2024).

[48] C. Kittel. *Introduction to solid state physics*. 8th ed. tex.added-at: 2011-04-14T10:28:42.000+0200 tex.asin: 047141526X tex.description: Amazon.com: Introduction to Solid State Physics (9780471415268): Charles Kittel: Books tex.dewey: 530.41 tex.ean: 9780471415268 tex.interhash: 7c425e2261b6584cc1df9c2da6d13331 tex.intrahash: d4e036d9937063fecea5b99c8498cdaf tex.timestamp: 2011-04-14T10:28:42.000+0200. Wiley, 2004. ISBN: 978-0-471-41526-8. URL: http://www.amazon.com/Introduction-Solid-Physics-Charles-Kittel/dp/047141526X/ref=dp_ob_title_bk.

[49] B. Martinez de Aguirre Jokisch. "Dispersion engineering of atom-nanophotonic crystal waveguide interfaces". PhD thesis. University of Copenhagen, 2022.

[50] E. P. Navarro-Barón, H. Vinck-Posada, and A. González-Tudela. "Directional spontaneous emission in photonic crystal slabs". en. In: *Nanophotonics* 13.11 (May 2024). Publisher: De Gruyter, pp. 1963–1973. ISSN: 2192-8614. DOI: 10.1515/nanoph-2023-0843. URL: https://www.degruyter.com/document/doi/10.1515/nanoph-2023-0843/html (visited on 09/13/2024).

[51] G. S. Agarwal. *PHYSICAL HEVIEW A VOLUME 12, NUMBKH 4 OCTOBER 1975 Quantum electrodynamics in the presence of dielectrics and conductors. IV. General theory for spontaneous enussion in finite geometries*.

[52] A. González-Tudela et al. "Subwavelength vacuum lattices and atom-atom interactions in two-dimensional photonic crystals". In: (2015). DOI: 10.1038/NPHOTON.2015.54. URL: www.nature.com/naturephotonics.

[53] R. Grimm, M. Weidemüller, and Y. B. Ovchinnikov. *Optical dipole traps for neutral atoms*. arXiv:physics/9902072. Feb. 1999. DOI: 10.48550/arXiv.physics/9902072. URL: http://arxiv.org/abs/physics/9902072 (visited on 09/04/2024).

[54] S. Y. Buhmann et al. "Casimir-Polder forces: A nonperturbative approach". en. In: *Physical Review A* 70.5 (Nov. 2004), p. 052117. ISSN: 1050-2947, 1094-1622. DOI: 10.1103/PhysRevA.70.052117. URL: https://link.aps.org/doi/10.1103/PhysRevA.70.052117 (visited on 09/15/2024).

[55] B. Martinez de Aguirre Jokisch et al. "Omnidirectional gradient force optical trapping in dielectric nanocavities by inverse design". In: *ACS Photonics* 0.0 (). tex.eprint: https://doi.org/10.1021/acsphotonics.4c01060, null. DOI: 10.1021/acsphotonics.4c01060. URL: https://doi.org/10.1021/acsphotonics.4c01060.

[56] P. Muñoz et al. "Silicon Nitride Photonic Integration Platforms for Visible, Near-Infrared and Mid-Infrared Applications". en. In: *Sensors* 17.9 (Sept. 2017). Number: 9 Publisher: Multidisciplinary Digital Publishing Institute, p. 2088. ISSN: 1424-8220. DOI: 10.3390/s17092088. URL: https://www.mdpi.com/1424-8220/17/9/2088 (visited on 09/23/2024).

[57] R. Baets et al. "Silicon photonics: Silicon nitride versus silicon-on-insulator". In: *2016 optical fiber communications conference and exhibition (OFC)*. 2016, pp. 1–3.

[58] K. H. Nam, I. H. Park, and S. H. Ko. "Patterning by controlled cracking". en. In: *Nature* 485.7397 (May 2012). Publisher: Nature Publishing Group, pp. 221–224. ISSN: 1476-4687. DOI: 10.1038/nature11002. URL: https://www.nature.com/articles/nature11002 (visited on 09/29/2024).

[59] M. Vangbo and Y. Bäcklund. "Precise mask alignment to the crystallographic orientation of silicon wafers using wet anisotropic etching". en. In: *Journal of Micromechanics and Microengineering* 6.2 (June 1996), p. 279. ISSN: 0960-1317. DOI: 10.1088/0960-1317/6/2/011. URL: https://dx.doi.org/10.1088/0960-1317/6/2/011 (visited on 06/10/2024).

[60] J. Bolten et al. "At low costs: Study on optical propagation losses of silicon waveguides fabricated by electron beam lithography". In: *Microelectronic Engineering*. Nano Lithography 2013 123 (July 2014), pp. 1–3. ISSN: 0167-9317. DOI: 10.1016/j.mee.2014.03.009. URL: https://www.sciencedirect.com/science/article/pii/S0167931714000823 (visited on 06/12/2024).

[61] K. Bordo and H.-G. Rubahn. "Effect of Deposition Rate on Structure and Surface Morphology of Thin Evaporated Al Films on Dielectrics and Semiconductors". en. In: *Materials Science* 18.4 (Dec. 2012). Number: 4, pp. 313–317. ISSN: 2029-7289. DOI: 10.5755/j01.ms.18.4.3088. URL: https://matsc.ktu.lt/index.php/MatSc/article/view/3088 (visited on 08/30/2024).

[62] A. P. Milenin et al. “The SOI planar photonic crystal fabrication: patterning of Cr using Cl2/O2 plasma etching”. In: *Microelectronic Engineering* 77.2 (Feb. 2005), pp. 139–143. ISSN: 0167-9317. DOI: 10.1016/j.mee.2004.10.001. URL: https://www.sciencedirect.com/science/article/pii/S0167931704004836 (visited on 08/30/2024).

[63] E. Langman. “The Design and Fabrication of Snap-Release Integrated Optomechanical Circuits”. en. PhD thesis. UC Santa Barbara, 2018. URL: https://escholarship.org/uc/item/68m6j4z5 (visited on 08/29/2024).

[64] A. Simonsen. *Smooth nitride etching with Cr hardmask*. en. URL: https://labadviser.nanolab.dtu.dk/images/7/7a/Report_summer2022_Anders_Simonsen_bghe_edits.pdf.

[65] *Etching (microfabrication)*. en. Page Version ID: 1226059711. May 2024. URL: https://en.wikipedia.org/w/index.php?title=Etching_(microfabrication)&oldid=1226059711#Anisotropic_wet_etching_(Orientation_dependent_etching) (visited on 09/20/2024).

[66] G. Vazquez, E. Alvarez, and J. M. Navaza. “Surface Tension of Alcohol Water + Water from 20 to 50 .degree.C”. In: *Journal of Chemical & Engineering Data* 40.3 (May 1995). Publisher: American Chemical Society, pp. 611–614. ISSN: 0021-9568. DOI: 10.1021/je00019a016. URL: https://doi.org/10.1021/je00019a016 (visited on 09/21/2024).

[67] N. Otsu. “A Threshold Selection Method from Gray-Level Histograms”. In: *IEEE Transactions on Systems, Man, and Cybernetics* 9.1 (Jan. 1979). Conference Name: IEEE Transactions on Systems, Man, and Cybernetics, pp. 62–66. ISSN: 2168-2909. DOI: 10.1109/TSMC.1979.4310076. URL: https://ieeexplore.ieee.org/document/4310076 (visited on 08/12/2024).

[68] S. Suzuki and K. be. “Topological structural analysis of digitized binary images by border following”. In: *Computer Vision, Graphics, and Image Processing* 30.1 (Apr. 1985), pp. 32–46. ISSN: 0734-189X. DOI: 10.1016/0734-189X(85)90016-7. URL: https://www.sciencedirect.com/science/article/pii/0734189X85900167 (visited on 08/12/2024).

[69] Itseez. *Open Source Computer Vision Library*. 2015. URL: https://github.com/itseez/opencv.

[70] F. Pedregosa et al. “Scikit-learn: Machine learning in Python”. In: *Journal of Machine Learning Research* 12 (2011), pp. 2825–2830.

[71] E. H. Synge. “XXXVIII. A suggested method for extending microscopic resolution into the ultra-microscopic region”. EN. In: *The London, Edinburgh, and Dublin Philosophical Magazine and Journal of Science* (Aug. 1928). Publisher: Taylor & Francis Group. DOI: 10.1080/14786440808564615. URL: https://www.tandfonline.com/doi/abs/10.1080/14786440808564615 (visited on 08/21/2024).

[72] D. W. Pohl, W. Denk, and M. Lanz. "Optical stethoscopy: Image recording with resolution λ/20". In: *Applied Physics Letters* 44.7 (Apr. 1984), pp. 651–653. ISSN: 0003-6951. DOI: 10.1063/1.94865. URL: https://doi.org/10.1063/1.94865 (visited on 08/21/2024).

[73] J. A. Veerman et al. "Single molecule mapping of the optical field distribution of probes for near-field microscopy". en. In: *Journal of Microscopy* 194.2-3 (1999). _eprint: https://onlinelibrary.wiley.com/doi/pdf/10.1046/j.1365-2818.1999.00520.x, pp. 477–482. ISSN: 1365-2818. DOI: 10.1046/j.1365-2818.1999.00520.x. URL: https://onlinelibrary.wiley.com/doi/abs/10.1046/j.1365-2818.1999.00520.x (visited on 08/22/2024).

[74] D. Vobornik and S. Vobornik. "SCANNING NEAR-FIELD OPTICAL MICROSCOPY". In: *Bosnian Journal of Basic Medical Sciences* 8.1 (Feb. 2008), pp. 63–71. ISSN: 1512-8601. URL: https://www.ncbi.nlm.nih.gov/pmc/articles/PMC5724879/ (visited on 08/21/2024).

[75] A. Bek. "Apertureless SNOM : a new tool for nano-optics". en. PhD thesis. EPFL, 2004. DOI: 10.5075/epfl-thesis-3073. URL: https://infoscience.epfl.ch/handle/20.500.14299/212380 (visited on 08/21/2024).

[76] A. A. Sukhorukov et al. "Dispersion extraction with near-field measurements in periodic waveguides". EN. In: *Optics Express* 17.5 (Mar. 2009). Publisher: Optica Publishing Group, pp. 3716–3721. ISSN: 1094-4087. DOI: 10.1364/OE.17.003716. URL: https://opg.optica.org/oe/abstract.cfm?uri=oe-17-5-3716 (visited on 08/21/2024).

[77] K. G. Lee et al. "Vector field microscopic imaging of light". en. In: *Nature Photonics* 1.1 (Jan. 2007). Publisher: Nature Publishing Group, pp. 53–56. ISSN: 1749-4893. DOI: 10.1038/nphoton.2006.37. URL: https://www.nature.com/articles/nphoton.2006.37 (visited on 08/21/2024).

[78] N. Granchi. "Scanning Near-Field Optical Microscopy: Recent Advances in Disordered and Correlated Disordered Photonics". en. In: *Photonics* 11.8 (Aug. 2024). Number: 8 Publisher: Multidisciplinary Digital Publishing Institute, p. 734. ISSN: 2304-6732. DOI: 10.3390/photonics11080734. URL: https://www.mdpi.com/2304-6732/11/8/734 (visited on 08/21/2024).

[79] R. Prasad and R. Vincent. "Resolving phase information of the optical local density of state with scattering near-field probes". In: *Physical Review B* 94.16 (Oct. 2016). Publisher: American Physical Society, p. 165440. DOI: 10.1103/PhysRevB.94.165440. URL: https://link.aps.org/doi/10.1103/PhysRevB.94.165440 (visited on 08/20/2024).

[80] B. le Feber, N. Rotenberg, and L. Kuipers. "Nanophotonic control of circular dipole emission". en. In: *Nature Communications* 6.1 (Apr. 2015). Publisher: Nature Publishing Group, p. 6695. ISSN: 2041-1723. DOI: 10.1038/ncomms7695. URL: https://www.nature.com/articles/ncomms7695 (visited on 09/13/2024).

[81] P. Bazylewski, S. Ezugwu, and G. Fanchini. "A review of three-dimensional scanning near-field optical microscopy (3D-SNOM) and its applications in nanoscale light management". In: *Applied Sciences* 7.10 (2017). Number: 973. ISSN: 2076-3417. DOI: 10.3390/app7100973. URL: https://www.mdpi.com/2076-3417/7/10/973.

[82] L. B. Lucy. "An iterative technique for the rectification of observed distributions". In: *The Astronomical Journal* 79 (June 1974). Publisher: IOP ADS Bibcode: 1974AJ.....79..745L, p. 745. ISSN: 0004-6256. DOI: 10.1086/111605. URL: https://ui.adsabs.harvard.edu/abs/1974AJ.....79..745L (visited on 08/24/2024).

[83] W. H. Richardson. "Bayesian-based iterative method of image restoration". In: *Journal of The Optical Society of America* 62.1 (Jan. 1972). Publisher: Optica Publishing Group, pp. 55–59. DOI: 10.1364/JOSA.62.000055. URL: https://opg.optica.org/abstract.cfm?URI=josa-62-1-55.

[84] J. S. Lim. *Two-dimensional signal and image processing*. Publication Title: Englewood Cliffs ADS Bibcode: 1990ph...book.....L. Jan. 1990. URL: https://ui.adsabs.harvard.edu/abs/1990ph...book.....L (visited on 08/24/2024).

[85] *Encyclopedia of Modern Optics*. en. ISBN: 9780123693952. URL: http://www.sciencedirect.com:5070/referencework/9780123693952/encyclopedia-of-modern-optics (visited on 08/23/2024).

[86] C.-Y. Fan, C.-P. Lin, and G.-D. J. Su. "Ultrawide-angle and high-efficiency metalens in hexagonal arrangement". en. In: *Scientific Reports* 10.1 (Sept. 2020). Publisher: Nature Publishing Group, p. 15677. ISSN: 2045-2322. DOI: 10.1038/s41598-020-72668-2. URL: https://www.nature.com/articles/s41598-020-72668-2 (visited on 09/28/2024).

[87] A. E. Klein. "Scanning near-field optical microscopy: from single-tip to dual-tip operation". en. In: (May 2015). URL: https://www.db-thueringen.de/receive/dbt_mods_00026018 (visited on 08/26/2024).

[88] J.-B. Béguin et al. "Coupling of light and mechanics in a photonic crystal waveguide". In: *Proceedings of the National Academy of Sciences* 117.47 (Nov. 2020). Publisher: Proceedings of the National Academy of Sciences, pp. 29422–29430. DOI: 10.1073/pnas.2014851117. URL: https://www.pnas.org/doi/full/10.1073/pnas.2014851117 (visited on 09/12/2024).

[89] T. Larsen et al. "Ultrasensitive string-based temperature sensors". In: *Applied Physics Letters* 98.12 (Mar. 2011), p. 121901. ISSN: 0003-6951. DOI: 10.1063/1.3567012. URL: https://doi.org/10.1063/1.3567012 (visited on 09/27/2024).

[90] J. Mathiassen. "Characterising and Modelling Thermal Substrate Noise for a Membrane in the Middle Optomechanical Cavity". MA thesis. University of Copenhagen, 2019.

[91] W. H. Nielsen. "Qantum Cavity Optomechanics with Phononic Bandgap Shielded Silicon Nitride Membranes". en. Publisher: University of Copenhagen. PhD thesis. 2016. URL: https://nbi.ku.dk/english/theses/phd-theses/william-h-p-nielsen/ (visited on 09/16/2024).

[92] A. Kaushik, H. Kahn, and A. Heuer. "Wafer-level mechanical characterization of silicon nitride MEMS". In: *Journal of Microelectromechanical Systems* 14.2 (Apr. 2005). Conference Name: Journal of Microelectromechanical Systems, pp. 359–367. ISSN: 1941-0158. DOI: 10.1109/JMEMS.2004.839315. URL: https://ieeexplore.ieee.org/document/1416912 (visited on 09/26/2024).

[93] R. L. Edwards, G. Coles, and W. N. Sharpe. "Comparison of tensile and bulge tests for thin-film silicon nitride". en. In: *Experimental Mechanics* 44.1 (Feb. 2004), pp. 49–54. ISSN: 1741-2765. DOI: 10.1007/BF02427976. URL: https://doi.org/10.1007/BF02427976 (visited on 09/26/2024).

[94] Z. Li et al. "Process Development of Low-Loss LPCVD Silicon Nitride Waveguides on 8-Inch Wafer". en. In: *Applied Sciences* 13.6 (Jan. 2023). Number: 6 Publisher: Multidisciplinary Digital Publishing Institute, p. 3660. ISSN: 2076-3417. DOI: 10.3390/app13063660. URL: https://www.mdpi.com/2076-3417/13/6/3660 (visited on 09/26/2024).

[95] Y. Levin. "Internal thermal noise in the LIGO test masses: A direct approach". In: *Physical Review D: Particles and Fields* 57.2 (Jan. 1998). Number of pages: 0 Publisher: American Physical Society, pp. 659–663. DOI: 10.1103/PhysRevD.57.659. URL: https://link.aps.org/doi/10.1103/PhysRevD.57.659.

[96] M. Born and E. Wolf. *Principles of Optics: Electromagnetic Theory of Propagation, Interference and Diffraction of Light*. 7th ed. Cambridge: Cambridge University Press, 1999. DOI: 10.1017/CBO9781139644181. URL: https://www.cambridge.org/core/books/principles-of-optics/D12868B8AE26B83D6D3C2193E94FFC32 (visited on 05/01/2024).

[97] lneuhaus. *lneuhaus/pyrpl*. Apr. 2024. URL: https://github.com/lneuhaus/pyrpl (visited on 05/02/2024).

[98] P. Welch. "The use of fast Fourier transform for the estimation of power spectra: A method based on time averaging over short, modified periodograms". In: *IEEE Transactions on Audio and Electroacoustics* 15.2 (June 1967), pp. 70–73. ISSN: 1558-2582. DOI: 10.1109/TAU.1967.1161901. URL: https://ieeexplore.ieee.org/document/1161901 (visited on 05/29/2024).

[99] L. H. Gabrielli. *gdstk*. 2020. URL: https://github.com/heitzmann/gdstk.

Appendix A - Parameters for the waveguide design

Table 1: Parameters for the waveguide design. All lengths are in μm.

Parameter	Value	Description
l_waveguide	1500	Length of waveguide
distance_to_coupler_tether	2	Distance from waveguide coupler to tether
w_waveguide	0.5	Width of waveguide
w_coupler	0.128	Width of coupler at the end
w_coupler_tether	0.100	Width of tether at the end of the coupler
l_taper_coupler	200	Length of coupling taper
l_groove	10000	Length of the groove
w_groove	150.00	Width of groove
l_coupler_first_array	100	Length between the end of the coupling taper and the angled tether array
a_tether_array	700	Pitch between tether arrays (ignored if n_tether_array is specified)
n_tether_array	2	Number of tether arrays
n_tether	15	Number of tethers per array
l_taper_tether	14	Length of tapering section around tethers
l_blank_tether	2	Length between taper and first tether
w_tether	0.110	Width of tethers
a_tether	0.238	Pitch of tethers
a_tether_at_rail	0.40	Pitch of tethers at rail
l_hole_tether	1	Length of tether holes
r_etch_hole	0.7	Radius of holes in tether plate
a_etch_hole	3.0	Pitch between tether plate holes
w_tether_section	1.5	Width of waveguide at tether section

Continued on next page

Parameter	Value	Description
angle_coupler	0	Angle of coupling tether (degrees)
angle_tensile	3.56	Angle of tilted array (degrees)
d_fine_exposure	100	Length after the waveguide for fine exposure
cell_name	default	Name of cell
layer_fine	0	Layer for fine exposure
layer_bulk	12	Layer for bulk exposure
positive_design_layer	42	Layer for positive tone design
layer_backside	24	Layer for backside exposure
layer_labels	60	Layer for labels
sleeve	10	Distance around fine area for exposure
overlap_bulk_fine	2	Overlap between fine and bulk exposure
w_rail	5	Width of supporting rails
pitch_rail_holes	3	Pitch of holes in siderails
r_rail_hole	0.5	Radius of holes in rail
recess_rail	330	Distance from window edge to first hole in rail
l_window	1000	Length of window on front
h_window	5000	Height of window on front
pitch_waveguide	320	Distance between waveguides
n_waveguide	1	Number of waveguides on chip
w_chip	10000	Chip width
h_chip	11000	Height of chip
substrate_thickness	500	Substrate thickness
r_fillet	1	Radius of fillets
r_fillet_tether	None	Fillet on tethers (calculated if None)
d_tip_coupler_tether	2	Distance from coupler tip to anchoring tether
tile_edge_width	2.0	Size of edge around exposed tiles
n_tiles	6	Number of tiles per groove width
origin	(0, 0)	Origin of the middle of the bottom waveguide
tolerance	1e-5	Tolerance for boolean operations
cleave_groove_width	200	Width of cleave groove
cleave_groove_extra_height	5000	Height of cleave groove
cleave_distance_from_waveguide	20	Distance from waveguide to cleave groove center
cleave_groove_frontside_width	100	Width of cleave groove on front side
layer_front_cleave	61	Layer for front cleave
tile_front_cleave	False	Add tiles to front cleave
front_groove_full	False	Add full front groove

Continued on next page

Parameter	Value	Description
cleave_at_chip_width	False	Cleave at chip width
window	False	Add window to chip
bragg_mirror_bool	False	Add Bragg mirror
bragg_period	0.31	Period of Bragg mirror
bragg_radius	0.11	Radius of Bragg mirror holes
bragg_N_taper	10	Number of tapers in Bragg mirror
bragg_N_holes	100	Number of holes in Bragg mirror
bragg_remove_N_holes	0	Number of holes to remove from Bragg mirror
bragg_r_min	0.08	Minimum radius of Bragg mirror holes
cavity_length	0	Length of cavity
magic_factor	0.0	Offset of the entire structure

Appendix B - Life of a File

For generating patterns, the gdstk library [99] which is C++ library with a python wrapper. This includes the various tools for constructing geometry. Other libraries exist for generating gds files with python, many of which are easier to use due to their less stringent adherence to the cell structure of the gds format. This does however come at the cost of making them slower for large designs, and more critically, they do not offer the same level of control over the generated gds file, which in turn can affect the compilation on the EBL machine.

The parameters for the geometry are stored in a dataclass object stored in the same file as the functions used for generating the design. The library partslib is imported, and a local copy of the configuration dataclass is created and modified to the desired parameters, and then used as the input for a function that generates the gds file. The default values are shown in table 1, which produces a simple waveguide with no spectrally selective features.

For simulating optical properties, the gds file is imported into Lumerical FDTD using a python wrapper that was written for this project. This wrapper has utility functions for quickly implementing 1D transmission simulations. It imports the gds file, detects the physical extent of the structure and creates the simulation to match it. Port objects are used to inject and measure light in the desired guided mode of the structure, and the boundary conditions are adjusted appropriately for the chosen symmetry.

Similar functionality is available for COMSOL for doing mechanical stress relaxation simulations, although the scripting interface is based om MATLAB, as this has officially supported integration with COMSOL. The gds file is imported into COMSOL, and the geometry is used to create a mesh and boundary conditions for the simulation.

To prepare a .gds file for e-beam lithography, there are a number of steps that depends on the system. A flow chart of the process is shown in fig. 1. A .gds file is created from the parameter config dataclass. Various simulations are then used to inform the design parameters. When the desired parameters have been found, the nominal design undergoes PEC, which requires a computer with a license for the Beamer software. The licensing of the Beamer software is such that it can only export to certain systems, and thus, using the Beamer PC at DTU, we can only export to the file format for the DTU

e-beam writer and vice versa. To define e-beam parameters such as dose, shot-pitch, chip-placement, alignment and so on is done via schedule-deck- (.sdf) and job-deck-files (.jdf). These are then compiled locally on the computer controlling the e-beam system. The Elionix 125 uses the GUI based WECAS software, making it slightly more user friendly.

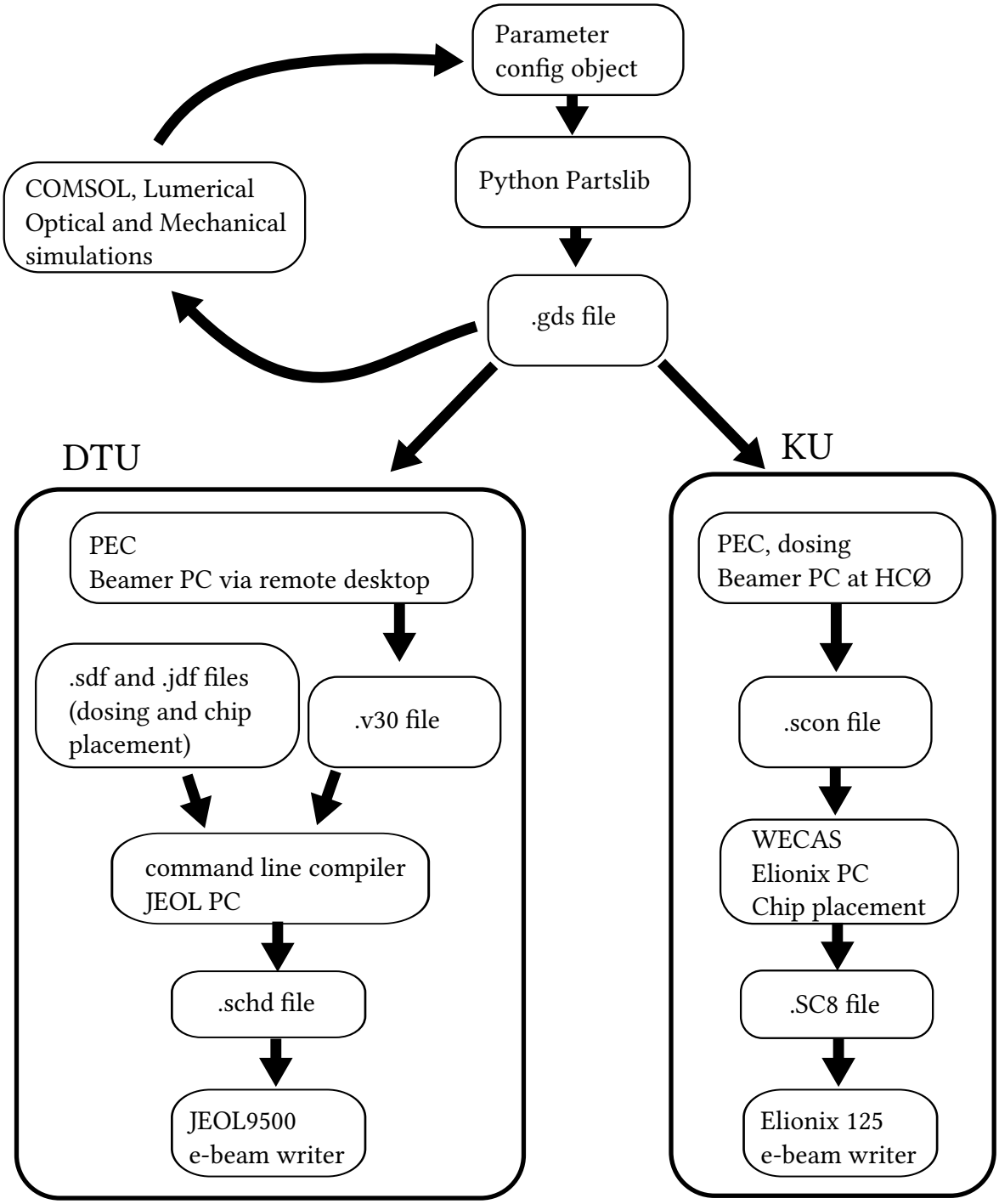

Figure 1: Flow chart showing the steps of compilation and file processing necessary to go from design parameters to lithography on an e-beam writer.

Appendix C - Summary of publication

Phononically shielded photonic-crystal mirror membranes for cavity quantum optomechanics

Georg Enzian[1,*], Zihua Wang[1], Anders Simonsen[1], Jonas Mathiassen[1], Toke Vibel[1], Yeghishe Tsaturyan[1,2], Alexander Tagantsev[3], Albert Schliesser[1], Eugene S. Polzik[1]

[1]*Niels Bohr Institute, University of Copenhagen, Blegdamsvej 17, 2100 Copenhagen, Denmark*
[2]*Present address: Pritzker School of Molecular Engineering, University of Chicago, Chicago, IL 60637, USA*
[3]*Swiss Federal Institute of Technology (EPFL), School of Engineering, Institute of Materials Science, CH-1015 Lausanne, Switzerland*

[*]Corresponding author: georg.enzian@nbi.ku.dk

Summary

This paper presents the development of a highly reflective, sub-wavelength-thick membrane resonator designed for cavity quantum optomechanics applications. The 88.5 nm-thick stoichiometric silicon nitride membrane combines two-dimensional photonic and phononic crystal patterns. A vital feature of the membrane is its high mechanical quality factor (Q) of 2.9×10^7 at room temperature, achieved through soft clamping and dissipation dilution techniques. The membrane demonstrates reflectivities as high as 99.89%, making it a highly efficient mirror in a Fabry-Perot-type optical cavity. The cavity exhibits non-Gaussian optical beam shapes in transmission, which align with theoretical predictions, and the membrane enables optomechanical sideband cooling to millikelvin temperatures starting from room temperature. Additionally, optomechanically induced optical bistability is observed at higher intracavity powers.

This work showcases the potential of the membrane for achieving high cooperativities with minimal light input, paving the way for advancements in optomechanical sensing, squeezing applications, and quantum ground-state cooling from room temperature.

Contribution

My contributions to the work presented in this paper are as follows: I constructed the optical setup and wrote the control software for the experiment. I performed mechanical measurements of the membrane Q-factor and resonance frequencies. I participated in discussions regarding simulations and performed SEM imaging and subsequent image analysis with the tools described in section 4.1